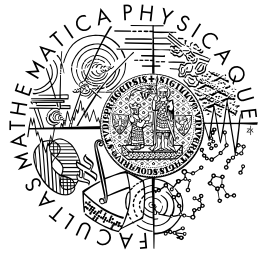

FACULTY
OF MATHEMATICS
AND PHYSICS
Charles University

DOCTORAL THESIS

Jakub Pokorný

The role of rheology and water in the deformation of subducting slabs

Department of Geophysics

Supervisor of the doctoral thesis: doc. RNDr. Hana Čížková, Ph.D.
Study programme: Physics
Study branch: Physics of the Earth and Planets

Prague 2024

I declare that I carried out this doctoral thesis independently, and only with the cited sources, literature and other professional sources. It has not been used to obtain another or the same degree.

I understand that my work relates to the rights and obligations under the Act No. 121/2000 Sb., the Copyright Act, as amended, in particular the fact that the Charles University has the right to conclude a license agreement on the use of this work as a school work pursuant to Section 60 subsection 1 of the Copyright Act.

In ..... date ....

Author's signature

To Zuz and Zita

I would like to express my deepest gratitude to my supervisor, Hanka Čížková, for her unwavering patience, especially with my writing, and for her invaluable guidance. Her insightful scientific and personal discussions have not only shaped my research but also profoundly contributed to my growth as a scientist.
I am grateful to Arie van den Berg for his support throughout my Ph.D. journey. His assistance, particularly with the programming and technical aspects of my project, and text editing, was invaluable. I also appreciate his generosity in hosting me during my stays at Utrecht University and also for personal discussions over a glass of beer in Kafé België.
A special thanks belongs to Erik van der Wiel for taking care of me in Utrecht and for the paper we wrote together. I enjoyed this project very much and i think we did a great job.
I also want to thank my other coauthors Craig Bina, Douwe van Hinsbergen, and Wim Spakman for the opportunity to make a scientific progress together. It was a pleasure working with you. I would like to extend my thanks to Hikaru Iwamori for providing me with his phase diagrams of peridotite systems, that are used in this thesis. I am greatful to Vašek Špillar for his expert comments on the geological parts of this thesis.
Last but not least I would like to thank to people (and Polárka) at the Department of Geophysics. To my fellow students - Franta, Honza, Kačka, Vojta, Martin, Burak, Lubica, Libor and Míša for being good friends and source of support. I also want to express my gratitude to all the other colleagues at the department for the stimulating discussions and the refreshing coffee breaks that kept the energy flowing.
Finally, I owe my deepest thanks to my family for being the best support I could have ever hoped for.
This research was supported by - Czech Science Foundation under grants number 18-20818S and 23-06345S , Charles University Grant Agency under grant number 36121, grant SVV 260709, and The Ministry of Education, Youth and Sports of the Czech Republic through the program INTER-EXCELLENCE II (grant LUAUS23233).

Title: The role of rheology and water in the deformation of subducting slabs

Author: Jakub Pokorný

Department: Department of Geophysics

Supervisor: doc. RNDr. Hana Čížková, Ph.D., Department of Geophysics

Abstract: The process of subduction, a key driver of plate tectonics, has been intensively studied over the past few decades. Understanding the complex mechanisms that control subduction dynamics is essential for comprehending slab fate in the transition zone, stress distribution associated with deep seismicity, water transportation, but also changes in plate motions driven by variations in slab sinking speed. Previous studies have shown that the combined effects of the rheology of crust and mantle and phase transitions control the deformation of the subducting lithosphere in the deeper parts of the Earth's mantle. In this thesis, we use numerical modeling of subduction to further elaborate on the material properties that influence subduction.

It has been previously shown that magnitude of constant crustal viscosity plays an important role in the slab behavior. Here we build on these findings and concentrate on the impact of nonlinear crustal rheology. We find that there is a feedback between slab velocity and nonlinear crustal viscosity that enhances transient nature of slab behavior and eventually facilitates slab penetration to the lower mantle after a temporary period of stagnation in the transition zone (TZ). Further, we evaluate the effects of water present in the oceanic crust. We show that besides the direct weakening of initially wet crust, subduction is further accelerated through weak hydrated mantle wedge. On the other hand, low density of wet crustal material might reduce plate velocity considerably especially in early stages of subduction.

In the application part, we explain the unusual stress orientations associated with deep earthquakes in the Tonga region. We show that the direct buoyancy effects from the phase transition at 660 km depth are overprinted by forces related to slab bending. Change in stress orientation occurs as the slab, temporarily deflected by the 660 km phase transition, penetrates the lower mantle, tightening the fold in the flat-lying part. This behavior is seen in cold slabs with the viscosity interface shifted from 660 km to 1000 km depth. Finally, we link slab deformation in TZ with surface plate motions. We find that buckling in the TZ causes rapid plate velocity oscillations of the Indian plate, as recently indicated by plate reconstructions. We show that the amplitude and period of these oscillations are controlled by the average subduction velocity and space available in the TZ.

Keywords: subduction dynamics, crustal and mantle rheology, transition zone, stress orientation, slab buckling, slab dehydration

Název: Vliv reologie a obsahu vody na deformaci subdukující desky

Autor: Jakub Pokorný

Katedra: Katedra geofyziky

Vedoucí práce: doc. RNDr. Hana Čížková, Ph.D., Katedra geofyziky

Abstrakt: Procesu subdukce, významnému hnacímu faktoru deskové tektoniky, byla v posledních dekádách věnována značná pozornost. Porozumění komplexním mechanismům, kontrolujících dynamiku subdukce, je zásadní pro pochopení chování desek v přechodové oblasti, rozložení napětí spojeného s hlubokou seismicitou, transportu vody, ale také variací v deskových pohybech, které jsou řízeny změnami subdukční rychlosti. Předchozí studie ukázaly, že deformace subdukující litosféry v hlubších partiích zemského pláště závisí na reologii kůry a pláště a fázových přechodech. V této práci využíváme numerické modelování subdukce k detailnějšímu pochopení vlivu materiálových vlastností na subdukci.
Dříve bylo ukázáno, že velikost konstantní viskozity kůry hraje v chování subdukce důležitou roli. Zde se zaměřujeme na vliv nelineární reologie kůry. Ukazujeme, že existuje zpětná vazba mezi rychlostí desky a nelineární viskozitou kůry. Variace viskozity kůry v čase vedou k dočasné stagnaci desky v přechodové oblasti (PO) a následnému proniknutí do spodního pláště. Zabýváme se také vlivem vody v kůře. Ukazujeme, že kromě snížení viskozity kůry voda také urychluje subdukci hydratací plášťového klínu. Na druhou stranu, nižší hustota hydratované kůry, může výrazně snižovat rychlost subdukce, zvláště v počátečním stádiu jejího vývoje.
V aplikační části práce vysvětlujeme nebvyklou orientaci napětí spojenou s hlubokými zemětřeseními v oblasti Tonga. Ukazujeme, že přímý vliv vztlakových sil spojených s fázovým přechodem v 660 km je menší než síly související se skládáním desky. Ke změnám v orientaci napětí dochází, když deska dočasně pozdržená fázovým přechodem v 660 km, proniká do spodního pláště a ohýbá se. Nakonec dáváme do kontextu deformaci desek v PO s jejich pohybem na povrchu. Zjistili jsme, že výrazné změny v rychlostech Indické desky, které byly indikovány deskovými rekonstrukcemi, jsou způsobeny kvaziperiodickým ohýbáním desky v PO. Ukazujeme, že amplituda a perioda těchto oscilací je řízena průměrnou subdukční rychlostí a prostorem, který je v PO k dipozici.

Klíčová slova: subdukční dynamika, reologie kůry a pláště, přechodová oblast, orientace napětí, skládání desky, dehydratace desky

Contents

Introduction

Planet Earth has two main sources of heat: primordial heat, which was acquired during its formation approximately 4.5 billion years ago, and the heat generated by the decay of radioactive isotopes of uranium, thorium, and potassium. The cooling of the Earth releases a significant amount of energy that drives convection in the mantle, manifested by plate tectonics at the surface. The oceanic lithosphere emerges at the mid-ocean ridges and plunges back into the mantle in the subduction zones. The primary driving force of plate tectonics is the slab pull of the subducting plate in subduction zones and, to a lesser extent, ridge push. On the contrary, slabs are slowed down by the viscous coupling at the contact of the plates and potentially by the drag of the mantle [e.g. Forsyth and Uyeda, 1975, Lithgow-Bertelloni and Richards, 1998]. The rates of the lithospheric plates at the surface reach up to 20-25 cm/a [Zahirovic et al., 2015, Hu et al., 2022], in contrast with significantly slower descent of the slabs through the lower mantle, typically at rates < 1.5 cm/a [e.g. van der Meer et al., 2010, 2018]. This slowdown of the slab on its way to deeper parts of the Earth's interior is accommodated by slab thickening. This phenomenon manifests diversely, with some slabs penetrating into the lower mantle and buckling almost vertically, while others are rolling back (i.e., the trench is retreating) and buckling subhorizontally in the mantle transition zone between 410 and 660 km [e.g. Ribe et al., 2007, Sigloch and Mihalynuk, 2013, Goes et al., 2017, Pokorný et al., 2021]. This diverse behavior has been documented by seismic tomography [e.g. Bijwaard et al., 1998, van der Meer et al., 2018]. The last 50 years of observations, and both numerical and analog modeling, have provided some understanding of the controlling factors of the subduction dynamics and slab deformation. These are mainly the rheology of both crustal and mantle material and the strength of mantle phase transitions [e.g. Christensen, 1996, Bina et al., 2001, van Hunen et al., 2001, Čížková et al., 2002, Billen and Hirth, 2007, Torii and Yoshioka, 2007, Běhounková and Čížková, 2008, Chertova et al., 2012, Agrusta et al., 2014, Holt et al., 2015, Rudolph et al., 2015, Arredondo and Billen, 2017, Faccenda and Zilio, 2017, Goes et al., 2017, Behr and Becker, 2018, Behr et al., 2022]. This doctoral thesis endeavors to enhance our understanding of the subduction process and its associated phenomena through numerical modeling. We further elaborate on the effects of rheology, phase transitions and water transport and evaluate their effects both in a parametric study and in applications to natural subduction zones.

The uppermost layer of the subducting plate, the crust, decouples the subducting and overriding plate, lowers the friction at the contact of the plates, and thus enables subduction. It has been shown that the mechanical properties of this decoupling layer play a crucial role in the subduction dynamics [e.g. Běhounková and Čížková, 2008, Chertova et al., 2012, Agrusta et al., 2014, Sandiford and Moresi, 2019]. Numerical models with simplified crustal rheology, e.g., by Androvičová et al. [2013], Behr et al. [2022] showed that the magnitude of constant crustal viscosity has direct implications for the subduction velocity. The study of Behr and Becker [2018] further revealed that sedimentary rocks lying on top of the subducting plate may reduce the viscosity of the lubricating layer by $\sim$ 1-2

orders of magnitude relative to the astenosphere. Work done by, e.g., Čížková and Bina [2013] or Goes et al. [2017] pointed out that magnitude of constant crustal viscosity influences trench rollback and the slab deformation in the mantle transition zone, and determines how and when the slab penetrates the lower mantle. It follows that detailed knowledge about the decoupling layer between subducting and overriding plate is crucial for understanding the subduction dynamics. To that end, in the first part of **chapter 3** we further elaborate on the combined effects of **constant crustal viscosity** and the **thickness** of the crust on the subduction dynamics. However, it is well known that in nature, crustal material deforms non-linearly [Shelton and Tullis, 1981, Ranalli, 1995]. In second part of **chapter 3** we thus study in detail how the **nonlinear crustal rheology**, combining the effects of dislocation creep and Byerlee type pseudoplatic deformation, influences subduction. We are interested mainly in the feedback between the slab velocity and the nonlinear strainrate dependent rheology of the crustal material and its influence on the deformation of the slab in the transition zone.

The deformation of the slab in the deeper parts of the Earth's mantle is mainly caused by the viscosity increase at the boundary between the transition zone and lower mantle and by the opposing buoyancy forces of the exothermic and endothermic mantle phase transitions at 410 and 660 km. Petrological buoyancy associated with phase transitions is responsible for slab buckling [Běhounková and Čížková, 2008], the viscosity increase at the base of the transition zone itself is sufficient to slow down slabs at these depths and make them thicken and stagnate [Goes et al., 2017]. This viscosity increase that marks the boundary between the transition zone and lower mantle is conventionally linked to the bridgmanite-forming endothermic phase transition at a depth of 660 km. Slabs usually stagnate above this boundary (e.g., Honsu, Aleutians or Ryuku slabs), but some seem to stagnate deeper at depths $\sim$ 1000 km as in case of, e.g., Java or Tonga slabs [Goes et al., 2017, Obayashi et al., 2013, Fukao and Obayashi, 2013]. Such deep stagnation might be associated with rheological boundary shifted towards the 1000 km depth [Rudolph et al., 2015]. This further illustrates the complexity of the process of subduction and points down to the fact, that different slab topologies, pictured by seismic tomography in the mantle, reflect a superposition of many factors. It is therefore essential to seek observational evidence that may further constrain the numerical models. Variations in slab deformation patterns result in distinct strain rate and stress fields within and in the vicinity of the slabs. An independent information about stress orientations in subducted slabs may thus be retrieved from source mechanisms of earthquakes that occurs within the subducted slabs. This information can be used to constrain subduction models, or on the contrary subduction models can be used to explain the nature of observed seismicity [Zahradník et al., 2017]. Here we will apply our subduction model and try to explain stress pattern associated with deep earthquakes in Tonga region. Deep earthquakes at depths around 660 km, are usually associated with down-dip compression due to the resistance from the endothermic phase transition. However, in the Tonga subduction region, where the Pacific plate subducts under the Australian plate, very deep earthquakes ($\geq$ 680 km) exhibit vertical tension contrary to expectations [Fukao and Obayashi, 2013, Fukao et al., 2014]. In **chapter 4** we study how the **rheology of the (lower) mantle, the**

strength of phase transitions as well as the possible **rheological boundary shift towards 1000 km** influence the stress field that is reflected in these unexpected focal mechanisms of deep earthquakes.

Seismic tomographic images as well as earthquake focal mechanisms document current state of subducting system - one snapshot in time. Numerical models on the other hand provide a complex picture of subduction process including the history of subducting plate velocity and trench motion, In nature, changes in tectonic plate motions are recorded in seafloor (marine) magnetic anomalies. These might be used in plate kinematic reconstructions, that allow us to look back in time on how the positions of the tectonic plates, their velocities and, to a certain extent, slab deformation evolved. Such reconstructions, usually sampled every 3-10 Ma, provide information about gradual changes in plate motions with occasional abrupt changes between the individual sample times [e.g. Torsvik et al., 2008, Müller et al., 2022]. The gradual changes can be, for example, explained by the changes in slab pull [e.g. Goes et al., 2011] or changes in lubrication at the contact of the plates [Behr and Becker, 2018]. The abrupt changes may be driven by, e.g., slab detachment [Bercovici et al., 2015], resistance to subduction of large oceanic plateaus [Knesel et al., 2008], or the arrival of mantle plume-head at the base of the plates [van Hinsbergen et al., 2021]. Recent work of DeMets and Merkouriev [2021] on high resolution ($\sim 0.5 - 1$ Ma) plate kinematic reconstruction of India-Africa spreading revealed rapid ($2-3$ Ma) plate velocity oscillations. In **chapter 5** we test if these velocity oscillations might be connected with **slab deformation through buckling** in the mantle transition zone and whether we might see a direct footprint of slab deformation in the tectonic plates motion.

As already mentioned above, slab deformation as well as the subduction rate critically depend on the mechanical properties of the crust. So far we have however not discussed an important factor that is essential in controlling crustal properties, and this is water. Wet rocks are less viscous and more buoyant [e.g. Nakao et al., 2016, 2018] than dry rocks and series of dehydration reactions that occurs with increasing pressure and temperature thus affects the decoupling of the subducting and overriding plate [e.g. Arcay et al., 2005]. Dehydration of crustal and mantle subducting material hydrates and weakens the mantle wedge [Karato and Jung, 1998] and promotes mantle wedge flow. The mantle wedge flow may potentially heat up the overriding plate, leading to its thermal erosion [Peacock and Wang, 1999, Eberle et al., 2002, Arcay et al., 2005]. Water carried further down to the upper mantle and transition zone is essential in explaining the mechanism of intermediate-depth and possibly also deep earthquakes [e.g. Zhan, 2020]. Therefore, studying the transport of water in subduction is vital for broadening our understanding of this process. In **chapter 6** we follow up on studying the influence of crustal rheology on subduction dynamics from chapter 3 and we will conclude this thesis by discussing how the presence of **water** in the crust and mantle wedge affects the subduction dynamics and slab deformation in the transition zone.

1. Mechanical properties of the oceanic lithosphere and the role of water

1.1 A very brief geology of the oceanic lithosphere

The origin of the oceanic crust (except the sedimentary layer) unfolds at mid-ocean ridges, where spinel lherzolite partially melts at depths of about 40 km and melt ascends towards the surface.

Oceanic crust is relatively thin - 7 km on average with density $\sim 3\ g/cm^3$. It is thinnest at mid-ocean ridges and gradually thickens as the material undergoes cooling. Seismic observations, deep-sea drill cores, and analysis of ophiolite complexes (a sequence of oceanic crustal rocks uplifted to the surface) have elucidated the structure of the oceanic crust. Conventionally, the rock series on the ocean crustal floor is categorized into three layers [White and Klein, 2014, Karson, 2002]: a sedimentary layer, a complex of pillow lavas and sheeted dike complex, and a layer of cumulate gabbro.

The composition of the sedimentary layer exhibits considerable variability influenced by multiple factors, including the regional climate, ocean depth, and proximity to the continent. The thickness of this layer is not uniform, reaching its minimum in abyssal zones (between mid-ocean ridges and margins) and attaining maximum thickness near continents (at subduction zones or passive margins), where fluvial sediments may significantly contribute. In more distant regions from continents, deep-sea clays, radiolarites, and carbonates become prevalent. Under the carbonate compensation depth, carbonate abundance decreases with depth as the rate of calcite dissolution increases [e.g. Zhang et al., 2022]. The fluvial system can transport substantial amounts of clastic sedimentary material to areas adjacent to continents and, consequently, to subduction zones. Sediments are believed to play an important role in weakening and lubricating the contact between the subducting and overriding plate [e.g. Behr and Becker, 2018]. However, factors such as arid climate or material entrapment in the back-arc area can severely limit the supply of this type of material [Seibold and Berger, 1984].

Pillow basalt lavas arise from the swift cooling of basaltic magma upon encountering sea water. The rapid cooling, allowing less time for crystallization, results in a fine-grained, glass-like structure. As depth increases, the basalt crystals grow in size, overlying a series of sheeted dikes complex composed of diabase.

According to Carbotte and Scheirer [2004], the thickness of this layer ranges from 1 to 3 km.

The last and thickest layer, situated within the oceanic crust, comprises cumulate gabbros. These banded rocks result from gravitational segregation during crystallization. The thickness of this layer varies from 3.5 to 5.5 km [White and Klein, 2014]. The primary minerals forming this thoelitic basaltic rock type are plagioclase (labradorite, bytownite, anorthite) and pyroxenes.

The lithospheric mantle is predominantly composed of a coarse-grained ultramafic peridotite. Typically, we can find two types of peridotite in the lithospheric mantle: lherzolite and harzburgite. Lherzolite is formed by olivine, orthopyroxenes and clinopyroxenes. Harzburgite, a partly depleted rock, forms after lithospheric mantle undergoes partial melting and is composed mainly of olivine and orthopyroxene. Rarely a third type of peridotite, dunite, can occur as lenses in the peridotite sequence. Dunite is even more depleted than harzburgite and consists mainly of olivine.

1.2 Rheology of the oceanic crust

Crust, the uppermost layer of the lithospheric plate is the lubricating contact layer between the subducting and overriding plate. Its mechanical properties thus determine to a large extent how the subduction behaves. Rheology of the crustal material is one of the main factors that significantly influence how fast the subduction is and how the slab deforms in the deeper parts of the mantle.

As the confining (lithostatic) pressure and temperature increase with depth, the response of the material to stress changes. In shallow parts of the crust, i.e. under low confining pressure and at low temperatures, crustal material deforms elastically (at small stresses and strains) or by fracturing (brittle deformation). Under high confining pressure and temperature, the crustal material deforms without fracturing, the deformation is ductile. The transition between brittle and ductile deformation is a function of pressure, temperature, and strain rate, thus this transition is not sharp.

When talking about brittle failure in connection with Earth's crust, we usually have cataclasis in mind. Cataclastic deformation involves the mechanical breakdown of rocks, primarily through fracturing and grinding [e.g. Sibson, 1977, Burov and Schubert, 2007, Karato, 2008]. In numerical models of subduction we usually approximate this brittle deformation with a Byerlee type deformation [Byerlee, 1978], that describes a stress conditions under which rocks slip along pre-existing cracs and faults (see eq. 2.14). Byerlee [1978] showed that the brittle stregth, i.e. the stress conditions under which rocks slip along faults in the brittle regime, is a function of lithostatic pressure, but is independent on the rock type and that is a huge advantage of this empirical law. Here we use parameters based on quarzite experiments [Liao et al., 2017].

The ductile deformation of crust is in numerical models of subduction usually

approximated by disclocation creep (see eq. 2.13) [e.g. van Hunen et al., 2000, Burov and Schubert, 2007, Pokorný et al., 2021]. As has been described in Section 1.1, oceanic crust consists of mafic rocks, namely basalt and gabbro. They differ in grain size, but have the same composition. The mechanical properties of these rocks are not as well reported as, for example, for olivine. In this thesis we use dislocation creep parameters for crust that are based on quarzite experimetns [Ranalli, 1995] and on the experiments on diabase (compositionally equivalent to volcanic basalt and plutonic gabbros) [Shelton and Tullis, 1981].

1.3 The role of water in the subduction process

Water is a ubiquitous and essential substance on Earth, playing a fundamental role in shaping the planet's physical, chemical, and biological processes. From a perspective of geology, water is crucial for a wide range of processes, such as weathering and erosion [e.g. Drever, 2005], the origin of karst phenomena [e.g. Bögli, 2012], geothermal activity [e.g. Barbier, 2002], formation and movement of glaciers [e.g. Eyles, 2006] and last but not least volcanism [e.g. Pawley and Holloway, 1993]. From a perspective of mantle circulation, water is vital for plate tectonics and the processes connected to it [e.g. van der Lee et al., 2008]. Water present in the crust and the top parts of the lithospheric mantle lowers the viscosity of the rocks and thus lubricates the contact between the subducting and overriding plates [e.g. Arcay et al., 2005, Nakao et al., 2018]. Dehydration of the subducting rocks is responsible for island arc volcanism through flux melting. Moreover, water is one of the possible mechanisms of deep earthquakes nucleation via dehydration embrittlement [e.g. Zhan, 2020].

Approximately 71 % of the Earth's surface is covered by oceans. Its mass $M_{oceans} \approx 1.4 \times 10^{21}$ kg makes ≈ 0.023 wt% of the Earth's total mass. Various other reservoirs of water such as ice, underground aquifers, lakes, rivers, soil, sediments, crust, and the atmosphere, contain approximately half the volume of water found in the world's oceans. The water content of the mantle can be assessed through high-pressure rock experiments, geochemical analysis of rocks, or methods such as electrical conductivity probing. Due to the inability to directly measure the water content of the mantle and core, a wide range of water content estimates were proposed. For mantle, the estimates are from 1 to 12 ocean mass [Inoue et al., 1995, Kohlstedt et al., 1996, Inoue et al., 1998, Litasov et al., 2003, Hirschmann, 2006, Pearson et al., 2014, Nakagawa and Iwamori, 2019]. The estimates of the hydrogen content in the core, make this Earth layer an enormous potential water reservoir with the water content ranging from 0.2 to 80 hydrogen equivalents of ocean masses [Genda, 2016, Peslier et al., 2017, Wu et al., 2018, Li et al., 2020c]. Recently, it has been suggested that the core contains hydrogen equivalent of 5 oceans [Wu et al., 2018, Li et al., 2020c]. These huge differences in estimates only illustrate how difficult it is to indirectly determine mantle and core water content and that these are strongly dependent on the geological and geochemical assumptions and methods that are used. However, even if we combine the higher estimates of water contained in the reservoirs listed above, the overall Earth's water budget should not exceed ~ 2 wt% of the Earth's mass [Mottl et al., 2007, Genda, 2016].

The origin of water on Earth is still a matter of debate. It is believed that oceans exist on Earth from the early stages of its evolution. This is based, among other things, on the existence of the ancient pillow lavas from Greenland 3.7 - 3.8 Ga old [Maruyama and Komiya, 2011]. Pillow lavas are formed when hot material (basaltic magma) rapidly cools down upon contact with water. One of the possible suggested theories of Earth's water origin is that part of the water originates from Earth's accretion from a protoplanetary disk and thus water was on our planet from the very beginning [Genda, 2016, Wu et al., 2018]. The second leading theory, the late-venner hypothesis, suggests that water found its way to our planet carried on asteroids and comets after the Earth had nearly fully formed [Genda, 2016, Peslier et al., 2017].

1.3.1 The form of water in the interior of the Earth

The majority of the Earth's water is not present as H_2O, but as hydroxyl (OH^-) or hydrogen (H) dissolved in minerals [Peslier et al., 2017]. Minerals that have water structurally bound in the crystal lattice are referred to as nominally hydrous minerals (e.g. serpentine, chlorite, talc). Alternatively, water might not be structurally bound within the crystal lattice of the mineral (hydrogen is missing in the chemical formula), but it is only structurally incorporated as (OH^-) or H_2O (very rare), through e.g. hydrogen bond or including hydrogen in structural defects. These minerals are referred to as nominally anhydrous minerals (e.g. wadsleyite, ringwoodite) [Keppler and Bolfan-Casanova, 2006]. In the literature, these are usually called wet minerals. Less frequently, liquid water may also be present in the pores of a sedimentary layer. This water is considered not to be mineralogically bound but free.

1.3.2 Hydration of the oceanic lithosphere

Let us now have a look at how water is supplied into the crustal and mantle material of the subducting plate.

The sedimentary layer of the oceanic lithospheric plate hydrates its minerals (e.g. chlorite, muscovite, phlogopite, and talc) through diagenesis and/or hydrothermal alteration. Diagenesis is a process of physical, chemical, and biological changes, e.g. through interaction with pore fluids and compaction of sediments after deposition and during their transition to sedimentary rocks. This process occurs at relatively low temperatures and pressures [e.g. Mackenzie, 2005]. Hydrothermal alteration is a metasomatic process involving the interaction of a preexisting solid phase with a hot mineral-rich fluid. It is difficult to estimate the water saturation of a sedimentary layer because its composition and thickness vary from one subduction zone to another. According to Plank and Langmuir [1998] the sedimentary layer of average composition (global subducting sediment - GLOSS) contains 7.29 wt% of water. In numerical models of subduction, the sedimentary layer,typically only a few hundred meters thick, is often excluded due to limited resolving power of a large-scale global models. However, because the layer is relatively thin and most of the water from sediments is out at relatively low pressures

$\sim$ 3 GPa [Chemia et al., 2015], it is acceptable that it is generally not considered in these models.

The layer underlying the oceanic sediments, the oceanic crust, is hydrated through hydrothermal alteration of basalt on its way from the mid-ocean ridges to trenches [e.g. Peacock, 1990, Hernández-Uribe et al., 2020]. As the oceanic floor cools and spreads, thermal stresses result in the formation of cracks in the upper parts of the oceanic crust. Water that finds its way through these cracks reacts with hot material and forms hydrothermally altered minerals (e.g. chlorite, lawsonite, amphibole, chloritoid, and epidote) [Schmidt and Poli, 1998, Faccenda, 2014]. For example, chlorite contains $\approx$ 13 wt% of water and is usually present in altered basaltic rocks by 5-30 wt%. Lawsonite bounds 11.2 wt% of water and forms 7-15 wt% of altered basalt. Amphibole is the most abundant hydrous mineral in altered basaltic rocks (20-60 wt%), but is capable of accommodating only 1-3 wt% [Cesare et al., 2003, Faccenda, 2014]. Schmidt and Poli [1998] conclude that saturated altered basaltic crustal material bounds, on average, 5-6 wt% of water. As the extent of hydrothermal alteration is a function of depth, the gabbroic part of the crust is usually considered to contain 0-2 wt% of water [Jarrard, 2003, Faccenda, 2014]. The extent of alteration has been confirmed based on P wave velocity experiments [e.g. Carlson and Jay Miller, 2004]. The level of water saturation strongly depends on the PT conditions of the slab, mineral assemblages, and the level of deformation (formation of cracks). The estimates of slab water saturation are usually based on the analysis of the rock samples obtained by drilling of the oceanic floor, geochemical analyses of ophiolite complexes [Alt et al., 1986, Staudigel et al., 1989, Bousquet et al., 1997] and/or determined based on the thermodynamic calculations of phase equilibrium [Schmidt and Poli, 1998, Iwamori, 2004, Connolly, 2005, Iwamori, 2007, Chemia et al., 2015].

Beneath the crust lies a mantle lithosphere made predominantly of peridotite. As the slab flexes at the trench, pre-existing cracks are promoted, and new ones may emerge throughout the crust down to the lithospheric layer, as discussed by e.g Peacock and Wang [1999] and Page and Hattori [2019]. When water reaches the lithospheric mantle, peridotite undergoes serpentinization. Serpentinization is a process of hydrothermal alteration transforming Fe-Mg silicates (e.g. olivine, pyroxenes) into serpentine polymorphs - lizardite (the most prevalent), antigorite, and chrysotile. Amphibole, talc, chlorite, and brucite may also be present in hydrated peridotites [Schmidt and Poli, 1998]. Serpentine contains up to 12.3 wt% of water. The water content in peridotites depends on the level of serpentinization, the presence of other minerals bounding water, and PT conditions. Peridotitic rocks are able to accommodate up to 15 wt% of water at P $\geq$ 12 GPa and T $\leq$ 1100 K (see fig. 2.3) [Iwamori, 2004, 2007]. The degree of hydration of the partially serpentinized mantle differs in literature. For example Chemia et al. [2015] use the value of 6.8 wt% with a linear decrease with depth [Ranero et al., 2003, Chemia et al., 2015]. On the contrary, Schmidt and Poli [1998] assumes only up to 1 wt% of water with linear decrease for young slabs and constant saturation of 1 wt% for the old one. In this thesis we will use the saturation diagram of Iwamori [2004, 2007] described in detail in chapter 2.5.

1.3.3 Dehydratation of the subducting slab

Dehydration is a metamorphic reaction leading to the release of water from the minerals. It is a complicated, quasi-continuous process of mineral destabilization. As the oceanic lithosphere descends into the Earth's interior, it crosses the PT stability fields of minerals, and consequently, water is released.

First, the porous (free) water is extruded from the pores due to the compaction and porosity reduction of the sedimentary material beneath the accretionary wedge and the forearc region [e.g Jarrard, 2003]. At similar conditions ($\sim 60 - 150\,°C$) , the bound water in clay minerals, opal and zeolites is also released [e.g. Saffer and Tobin, 2011] Dehydration at these conditions may lead to the formation of mud volcanoes in the fore-arc region [Hensen et al., 2004].

Dehydration of the crust takes place via progressive metamorphism from altered basalt through greenschist facies, blueschist facies to eclogite facies assemblage. Water released from the crust percolates upward and hydrates the mantle wedge material, forming serpentine minerals and chlorite [Arcay et al., 2005, Hirschmann, 2006]. This newly formed hydrated layer is dragged down by the ongoing subduction. At temperatures approximately 600 - 800°C, metamorphic breakdown of serpentine and then chlorite takes place [Iwamori, 2007, Spandler and Pirard, 2013]. Water released from serpentinized mantle wedge hydrates further the overlying material and may trigger arc volcanism [Arcay et al., 2005]. Because dehydration reactions are controlled by temperature and pressure, the depth of these reactions depends strongly on the thermal state of the slab in the given subduction region [Kirby et al., 1991]. In general, colder and faster slabs can deliver water to greater depths [Ohtani et al., 2004, van Keken et al., 2011]. This is also dependent on the composition of subducting slab [Rüpke et al., 2004, van Keken et al., 2011]. However, laboratory experiments suggest that the limit for the total dehydration of the crustal material is 300 km depth [Litasov and Ohtani, 2007, Faccenda, 2014].

Finally, water released by serpentine and chlorite breakdown from the serpentinized lithospheric slab percolates upwards through the slab and reacts with the crustal material, where lawsonite and phengite are potentially formed. These two minerals are stable up to approximately 300 km depth [Ono, 1998, Spandler and Pirard, 2013]. Downgoing serpentinized lithosphere remains partly hydrated as long as the geotherm remains under the choke point.

The choke point occurs at $\sim$ 6 GPa [$\approx$180 km] and 600°C and represents the transition from the upper-pressure limit of the stability range of serpentine minerals to low-pressure limit for the stability range of Phase A [Schmidt and Poli, 1998, Hirschmann, 2006]. Water that is dragged by the old and fast slabs down to the transition zone can be stored in the dense hydrous magnesium silicate (DHMS) phases (phase A, phase E, phase D, and superhydrous phase B) and in the high-pressure olivine nominally anhydrous polymorphs wadsleyite and ringwoodite. These olivine polymorphs have a huge H_2O storage capacity up to 3 wt% and 2 wt%, respectivelly [Kohlstedt et al., 1996, Inoue et al., 1995, Litasov et al., 2003]. This is the reason why transition zone and mantle in general are consid-

ered to be an important water reservoir, possibly containing up to several ocean masses [e.g. Inoue et al., 1995, Kohlstedt et al., 1996, Inoue et al., 1998, Litasov et al., 2003]. The solubility of H_2O in wadsleyite and ringwoodite decreases with rising temperature and reaches 0 wt% at the boundary between the transition zone and the lower mantle. Here also most of the DHMS phases decompose and only phase D transports water further into the lower mantle [Hirschmann, 2006]. In very cold slabs, it is also a superhydrous phase B transporting water beneath the transition zone-lower mantle boundary. The stability field of phases D and superhydrous phase B is estimated to reach approximately 44 GPa (∼1250 km), where it decomposes into the anhydrous phases and fluids [Shieh et al., 1998, Litasov and Ohtani, 2007]. Because of the very limited water storage capacity of the nominally anhydrous minerals of the lower mantle, this should result in melting [Hirschmann, 2006]. In case the produced melts were positively buoyant, they would move upwards through the 660 km phase boundary and solidify in the transition zone [Bercovici and Karato, 2003]. In the opposite scenario, the negatively buoyant melts are stored in the D'' layer. If this is the case, a big portion of water is sequestered above core-mantle boundary [Hirschmann, 2006]. These scenarios are however a subject of debate.

The water storage capacity of the lower mantle (composed mainly of Mg - perovskite, ferropericlase, and Ca - perovskite) is unclear and controversial. Suggested water storage capacities can differ by two orders of magnitude [e.g. Murakami et al., 2002, Litasov et al., 2003, Bolfan-Casanova et al., 2003]. Some of the estimates argue that the water storage capacity of the lower mantle is comparable to three oceans[e.g. Litasov et al., 2003]. Most of the studies agree that there is a layered structure in the water storage capacity of the mantle. The upper and lower mantle have relatively low water storage capacities, in contrast to the transition zone with high water storage capacity [Ohtani et al., 2004].

1.3.4 How water influences subduction dynamics

Water bound in the crustal and lithospheric mantle material influences the viscosity and density of the slab and hence has an impact on its velocity and deformation. In some cases it could even affect slab ability to penetrate to the lower mantle [Nakao et al., 2016]. Moreover, water released from the slab hydrates the mantle wedge and lowers its viscosity [Karato and Jung, 1998].

Lower viscosity promotes mantle wedge flow, which is an important mechanism playing a role in the evolution of the thermal state of the subducting and overriding plate [Van Keken et al., 2002]. The mantle wedge flow may heat up the overriding plate, which can be subsequently thermally eroded [Peacock and Wang, 1999, Eberle et al., 2002, Arcay et al., 2005]. By the interplay of the rollback followed by the overriding plate thinning and the presence of water in the mantle wedge, back-arc opening together with decompression melting may occur resulting in back-arc volcanism [Nakao et al., 2016]. Similar behavior may emerge due to the hydration of overriding plate by percolating water [Gerya and Meilick, 2010] or by Rayleigh-Taylor instabilities (wet plumes) [Richard and Iwamori, 2010].

The presence of hydrous rocks also reduces the density of the material. The increased buoyancy, reduces the driving force of the subduction [Nakao et al., 2016]. Furthermore, hydration of the mantle wedge should reduce the convergence rate even more, because the lower density influences the normal stresses operating in the overriding plate and thus reduces trench retreat [Royden and Husson, 2006, Nakao et al., 2018]. It has been shown by Nakao et al. [2016], that also the tensile stresses in the shallow parts of the slab are reduced due to lower density. This may further suppress back-arc spreading due to insufficient negative buoyancy [Nakao et al., 2018].

2. Numerical model

The mantle convection model applied in the numerical modelling experiments presented in this thesis is described in the following subsections.

2.1 Governing equations

Thermal convection in our model is described by a system of partial differential equations (PDEs) derived from conservation of mass, momentum and energy. Here we apply an extended Boussinesq approximation (EBA) [Christensen and Yuen, 1985, Ita and King, 1994]. This implies an incompressible viscous fluid, with a divergence-free velocity field and density variations that are accounted for only in the buoyancy term of the momentum equation.
Mass conservation for the incompressible fluid medium, as described by the continuity equation, implies a divergence free flow field, with components v_j,

$$\partial_j v_j = 0. \tag{2.1}$$

Conservation of momentum for the highly viscous fluid in creeping flow is described with Stokes equation for an infinite Prandtl number [Schubert et al., 2001].

$$\partial_j \sigma_{ij} + \rho g_i = 0. \tag{2.2}$$

The stress tensor σ_{ij} is rewritten in terms of thermodynamic pressure P and deviatoric stress τ_{ij}, with $\sigma_{ij} = -P\delta_{ij} + \tau_{ij}$. Pressure is split in $P = p + \Delta P$ with p and ΔP, hydrostatic and dynamic pressure respectively. Density ρ is split as $\rho = \rho_r + \Delta\rho$, with ρ_r a reference value, and $\partial\rho_i = \rho_r g_i$.
Substitution in eq. 2.2 gives a reduced Stokes equation with density perturbations $\Delta\rho$ as a driving term,

$$-\partial_i \Delta P + \partial_j \tau_{ij} + \Delta\rho g_i = 0. \tag{2.3}$$

The shear stress tensor of the viscous material is expressed in the effective viscosity that may depend on material composition, through weight fractions, $X_j, j = 1, ...n_c$, of material components, temperature T, hydrostatic pressure p, material phase Γ, (section 2.2.7), and bound water content w_b,

$$\tau_{ij} = \eta_{eff}(X, T, p, \sigma, \Gamma, w_b)\dot{\epsilon}_{ij}, \tag{2.4}$$

η_{eff} is the effective viscosity and $\dot{\epsilon}_{ij} = \partial_i v_j + \partial_j v_i$ are the components of the strain rate tensor, expressed in the velocity vector components.

g_i are the components of the gravity acceleration vector and $\Delta\rho$ is the density variation with respect to a reference value ρ_r, due to variation of material composition, temperature, material phase constrained by a pressure-temperature phase diagram, and compound bound water content,

$$\Delta\rho = \rho(X, P, T, w_b) - \rho_r. \tag{2.5}$$

The thermal equation derived from energy conservation is,

$$\rho c_p \frac{\mathrm{dT}}{\mathrm{dt}} - \alpha T \frac{\mathrm{dp}}{\mathrm{dt}} + \rho \Delta Q_{ph} = \partial_j (k \partial_j T) + \tau_{ij} \partial_j v_i + \rho H. \tag{2.6}$$

Here c_p is the specific heat at constant pressure, and α is the thermal expansion coefficient. ΔQ_{ph} is the latent heat per unit mass and unit time produced in solid state phase transitions, specified in section 2.2.7. k is the thermal conductivity, and H is the heat production per unit mass and unit time by radiogenic heating. Terms on the left in (eq. 2.6) represent the rate of change of heat content, adiabatic heating and latent heat exchange respectively. The terms on the right represent thermal diffusion, viscous dissipation and radiogenic heating.
The equations are solved on 2-D rectangular box domains. Boundary conditions applied for the solution of Stokes equation (eq. 2.3) are, in most of our models: impermeable and free slip, i.e. setting the normal velocity component and the tangential shear stress zero. Some of the models have a prescribed tangential velocity component, instead of free slip, on part of the boundary. This way a plate velocity may be prescribed in a kinematically driven convection model. For the energy equation we apply a prescribed temperature on the top and bottom boundaries and a zero heat flow condtion on the vertical side boundaries.
In the following sections the physical properties that appear in the coefficients of the governing equations will be further specified.

2.2 Model material properties

The mantle convection model used in our numerical modelling experiments applies composite materials in a mechanical mixture model. The material components may have contrasting values and parameterizations of the physical properties that occur in the coefficients of the model PDE's (eq. 2.3) and (eq. 2.6). We apply appropriate averaging for evaluating effective or compound values of the physical properties for the mixture, in particular for viscosity in section 2.2.4, density in section 2.2.5, phase characteristics in section 2.2.7 and water dependent properties in section 2.4
The material composition is described by component weight fractions $X_j, j = 1, ...n_c$, with $X_{n_c} = 1 - \sum_{j=1}^{n_c-1} X_j$. Our model does not include material diffusion and chemical reactions. This implies that the weight fractions are invariant,

$$\frac{\mathrm{dX_j}}{\mathrm{dt}} = 0, j = 1, ...n_c. \tag{2.7}$$

Most of our convection models include two material components: basaltic oceanic crust and general peridotitic mantle material respectively.

2.2.1 Mantle rheology

The rheology of the dry mantle material, including the lithospheric plates, is described by a composite model [van den Berg et al., 1993], including several solid state creep mechanisms. The effective viscosity combines multiple deformation mechanisms, diffusion creep, dislocation creep [Karato and Wu, 1993], and a power-law stress limiter [Čížková et al., 2002]. Diffusion creep viscosity is expressed as,

$$\eta_{diff} = A_{diff}^{-1} \exp\left(\frac{E_{diff} + pV_{diff}}{RT}\right), \tag{2.8}$$

where A_{diff} is pre-exponential parameter of diffusion creep, E_{diff} is activation energy of diffusion creep, p is hydrostatic pressure, V_{diff} is activation volume of diffusion creep, R is the gas constant and T is the absolute temperature. Dislocation creep viscosity is defined by,

$$\eta_{disl} = A_{disl}^{-1/n} \ \dot{\epsilon}_{\|}^{(1-n)/n} \ \exp\left(\frac{E_{disl} + pV_{disl}}{nRT}\right). \tag{2.9}$$

Here A_{disl}, E_{disl} and V_{disl} are pre-exponential parameter, activation energy and activation volume of dislocation creep viscosity and the exponent $n = 3.5$ [Kameyama et al., 1999]. $\dot{\epsilon}_{\|}$ is the second invariant of the strain rate tensor defined as,

$$\dot{\epsilon}_{\|} = \frac{1}{2}\sqrt{\dot{\epsilon}_{ij}\dot{\epsilon}_{ij}}. \tag{2.10}$$

A power-law stress limitor is used as an approximation of Peierls creep [Androvičová et al., 2013] with viscosity

$$\eta_y = \sigma_y \dot{\epsilon}_y^{\ -(1/n_y)} \ \dot{\epsilon}_{\|}^{(1/n_y)-1}, \tag{2.11}$$

where $\dot{\epsilon}_y$ is a reference strain rate and σ_y is the stress limit. The exponent n_y is usually taken within the range of 5-10, here we use $n_y = 10$ Values of stress limit σ_y are based on stress estimates in the subducting slab and are usually in the range of $0.1 - 1$ GPa.
Parameters of the above described diffusion and dislocation creep applied in our models are based on experiments on wet olivine [Hirth and Kohlstedt, 2003a].
Viscosities of individual creep mechanisms are combined into an effective viscosity [van den Berg et al., 1993] as

$$\eta_{eff} = \left(\frac{1}{\eta_{diff}} + \frac{1}{\eta_{disl}} + \frac{1}{\eta_y}\right)^{-1}, \tag{2.12}$$

The lack of observed seismic anisotropy in most of the lower mantle is usually interpreted as an absence of lattice preferred orientation associated with dislocation creep. The lower mantle is therefore assumed to be primarily deformed through diffusion creep [Karato et al., 1995]. In line with that, our lower mantle $\eta_{eff} = \eta_{diff}$ with parameters based on slab sinking speed analysis [Čížková et al., 2012]. If the stress in the lower mantle slab should exceed the yield stress, a stress limiter may be also applied in the lower mantle. The boundary between upper and lower mantle is defined by an endothermic phase transition (see section 2.2.7) that approximates the transformation of ringwoodite into bridgemanite and periclase near 660 km depth. This is reflected in the contrasting upper/lower mantle viscosities in our phase dependent rheology.

2.2.2 Crustal rheology

Our subduction models include a compositionally distinct layer of crustal material, the viscosity of which facilitates the decoupling of the subducting and overriding plates. This crustal layer has either constant(low) viscosity, or in more advanced models, is assumed to have a composite rheology inlcuding stress and or water dependent mechanisms. In the models where crust is considered to deform nonlinearly, the composite rheology combines dislocation creep [Ranalli, 1995] and a Byerlee type deformation [Karato, 2008](further referred to as pseudoplasticity). The crustal dislocation creep viscosity is parameterized as,

$$\eta^c_{disl} = A_c^{-1/n_c}\ \dot{\epsilon}_{\|}^{(1-n_c)/n_c}\ \exp\left(\frac{E_c + pV_c}{n_c RT}\right). \tag{2.13}$$

Where A_c, n_c, E_c and V_c are pre-exponential parameter, exponent, activation energy and activation volume of the dislocation creep for the crustal material. Pseudoplastic viscosity is defined as

$$\eta_{pl} = \frac{\sigma^c_y}{2\dot{\epsilon}_{\|}}, \tag{2.14}$$

where σ^c_y is a stress limit in the crust, increasing with hydrostatic pressure p as

$$\sigma^c_y = \tau_c + \mu p\,. \tag{2.15}$$

Here τ_c is the cohesion and μ a friction coefficient. Crustal effective viscosity is then calculated as

$$\eta^c_{eff} = \left(\frac{1}{\eta^c_{disl}} + \frac{1}{\eta_{pl}}\right)^{-1}. \tag{2.16}$$

2.2.3 Effect of water on rheology

In models where crustal or mantle material contains bound water, its effect on viscosity is parametrized with the weight fraction of bound water. Here we apply a parametrization similar as in [Arcay et al., 2005] by introducing water dependent viscosity prefactors, $f_w(w_b)$, for diffusion and dislocation creep and for the friction factor of Byerlee type plasticity.
The viscosity of diffusion creep (eq. 2.8) is then modified as

$$\eta_{diff} = A_{diff}^{-1} f_w(w_b) \exp\left(\frac{E_{diff} + pV_{diff}}{RT}\right), \tag{2.17}$$

and dislocation creep viscosity (eq. 2.9) becomes

$$\eta_{disl} = A_{disl}^{-1/n} f_w(w_b)\, \dot{\epsilon}_{\|}^{(1-n)/n} \exp\left(\frac{E_{disl} + pV_{disl}}{nRT}\right). \tag{2.18}$$

For the stress limit of the Byerlee type plasticity,

$$\tau_y^c = \tau_c + f_w(w_b)\mu p. \tag{2.19}$$

The bound water effect in these cases is mediated by a prefactor function $f_w(w_b)$, which is defined as,

$$f_w(w_b) = (1 - f_m)\exp(-w_b/w_{b_{ref}}) + f_m, \tag{2.20}$$

where w_b is the weight fraction of bound water, $w_{b_{ref}} = 6.2 \times 10^{-4}$ is a reference water content [Arcay et al., 2005] corresponding to a low hydration value, and $f_m < 1$ defines the viscosity contrast between hydrated material and dry material ($f_w(0) = 1$). Parameter f_m may be considered in the range of approximately $0.01 - 0.5$ [Arcay et al., 2005]. Here, we will consider f_m a free parameter and its effect will be tested.

2.2.4 Compound viscosity of the composite material

Our model includes multiple material components represented as a mechanical mixture. Effective (compound) material properties for the mixture are expressed in terms of the component (endmember) weight fractions X_j, or volume fractions ϕ_j and corresponding component properties. For the compound viscosity, we apply harmonic averaging based on the volume fractions,

$$\eta^{-1} = \sum_{j=1}^{n_c} \phi_j \eta_j^{-1}. \tag{2.21}$$

The volume fractions ϕ_j are expressed in the weight fractions X_j as, $\phi_j = X_j(\rho/\rho_j)$.

2.2.5 Density model and equation of state

Buoyancy, as a result of density variations $\Delta\rho$, in (eq. 2.5), is the main driving force in our thermo-chemical convection models. The equation of state for density of the mechanical mixture, is expressed in the component density values ρ_j and weight fractions X_j as,

$$\rho(X,P,T) = \left[\sum_{j=1}^{n_c} \frac{X_j}{\rho_j(P,T)}\right]^{-1}. \tag{2.22}$$

The component densities ρ_j in (eq. 2.22) are subject to thermal expansion and they depend on their material phase, defined by corresponding P,T phase diagrams. Thermal expansion is linearized with respect to an isothermal reference state T_r and the phase dependence is parametrized with phase functions $\Gamma_{ij}(P,T) \in [0,1]$ and phase related density increment values $\Delta\rho_{ij}$, (see section 2.2.7) as,

$$\rho_j(P,T) = \rho_{rj}\left[(1-\alpha_j(T-T_r)) + \sum_{i=1}^{n_{phj}} \frac{\Delta\rho_{ij}}{\rho_{rj}}\Gamma_{ij}(P,T)\right]. \tag{2.23}$$

Here n_{phj} is the number of phase transitions of material component j, and α_j is the thermal expansion coefficient. In the EBA approximation, these density variations are taken into account only in the buoyancy term of the momentum equation.

2.2.6 Effect of water on density

In the models that include water transportation, the density may further be affected by bound water. This is included in our model at the coumpound density level (eq. 2.22) with the following parametrization,

$$\rho(X,P,T,w_b) = \rho(X,P,T) \times (1-\beta w_b), \tag{2.24}$$

where w_b is the compound weight fraction of bound water and β is a water density coefficient [Nakao et al., 2016]. According to [Richard and Iwamori, 2010] the value of β is not well constrained under high-pressure conditions and hence β is usually taken into account as a free parameter in the range [0,2].

2.2.7 Implementation of material phase transitions

As mentioned before, in our convection model, we account for phase-dependent density and viscosity in the Stokes equation (eq. 2.3). Moreover, the energy equation (eq. 2.6) features the term $\rho\Delta Q_{ph}$, which represents the latent heat exchange during the phase transitions of the composite material. Here we present the parametrization of these phase-related components of our model. Our convection model incorporates the main phase transitions of the mineral component olivine $(Mg,Fe)_2SiO_4$ of the mantle peridotite material. These are the exothermic polymorphous phase transition at around 410 km depth, where forsterite $(\alpha - Mg_2SiO_4)$ changes its structure into the wadsleyite $(\beta - Mg_2SiO_4)$ and

the endothermic phase transition at around 660 km depth through which ringwoodite ($\gamma - Mg_2SiO_4$) transforms into bridgemanite ($MgSiO_3$) and periclase (MgO). The transition of wadsleyite to ringwoodite at around 520 km depth is not included in our models. Both phase transitions are associated with a density increase of several percent. Our model offers two approaches for evaluating phase dependent properties ρ, α, and c_p, in a convection model run. The first method involves parameterizing the PT phase diagrams using a phase parameter function $\Gamma(P,T)$. The second approach allows for these properties to be tabulated in PT space during a preprocessing step. This is done either by parameterization or by employing more general mineral physics techniques.

Parameterized phase transitions

The first method that uses parameterization of P,T diagrams employs phase parameter functions $\Gamma_{ij}(P,T)$ for distinct phase transitions. Here i and j are the phase and material index respectively. These phase functions are defined based on the phase boundary (Clapeyron) curves, represented as $P_{ij}(T)$,

$$\Gamma_{ij}(P,T) = \Gamma_{ij}(P - P_{ij}(T)) = \Gamma_{ij}(\Pi_{ij}(P,T)). \tag{2.25}$$

Here the Π_{ij} are excess pressure coordinates along an isotherm,

$$\Pi_{ij}(P,T) = P - P_{ij}(T). \tag{2.26}$$

We use a linear approximation for the Clapeyron curves,

$$P_{ij}(T) = P_{ijr} + \gamma_{ij}(T - T_{ijr}), \tag{2.27}$$

where the (P_{ijr}, T_{ijr}) define reference points on the individual phase boundary curves and $\gamma_{ij} = \mathrm{dP_{ij}/dT}$, are corresponding constant Clapeyron slopes. The phase functions $\Gamma_{ij} \in [0,1]$ are parameterized piecewise as smooth step functions around the transition pressure,

$$\Gamma_{ij}(\Pi_{ij}(P,T)) = \begin{cases} 0, & \frac{\Pi_{ij}}{\delta P_{ij}} < -\frac{1}{2} \\ \frac{1}{2}\left[1 + \sin\left(\pi \frac{\Pi_{ij}}{\delta P_{ij}}\right)\right], & -\frac{1}{2} \leq \frac{\Pi_{ij}}{\delta P_{ij}} \leq \frac{1}{2} \\ 1, & \frac{\Pi_{ij}}{\delta P_{ij}} > \frac{1}{2} \end{cases}. \tag{2.28}$$

Here δP_{ij} is the pressure width of the phase transition. This expression for $\Gamma_{ij}(P,T)$ is applied in the evaluation of the phase related density (eq. 2.23).

Latent heat exchange during phase transitions

The latent heat exchange associated with the phase transitions is included in the energy equation (eq. 2.6),

$$\Delta Q_{\mathrm{ph}} = \Delta c_p \frac{dT}{dt} - T\frac{\Delta\alpha}{\rho}\frac{dP}{dt}. \tag{2.29}$$

Here, $\Delta\alpha$ and Δc_p represent the contributions to the effective thermal expansivity α^* and the specific heat at constant pressure c_p^*, where $\alpha^* = \alpha + \Delta\alpha$ and $c_p^* = c_p + \Delta c_p$ and α and c_p denote the values for the involved phases.

$$\Delta c_p = -T\sum_{j=1}^{n_c} X_j \sum_{i=1}^{n_{\mathrm{ph}j}} \Delta S_{ij}\frac{d\Gamma_{ij}}{d\Pi_{ij}}\gamma_{ij} \tag{2.30}$$

$$\Delta\alpha = -\rho\sum_{j=1}^{n_c} X_j \sum_{i=1}^{n_{\mathrm{ph}j}} \Delta S_{ij}\frac{d\Gamma_{ij}}{d\Pi_{ij}} \tag{2.31}$$

Here ΔS_{ij} [1] is the specific entrophy contrast. The contributions $\Delta\alpha$ and Δc_p are non-zero during any phase transitions when $\frac{d\Gamma_{ij}}{dt} \neq 0$. The expression for these derivatives, derived from equation (eq. 2.28), is,

$$\frac{d\Gamma_{ij}}{d\Pi_{ij}} = \begin{cases} 0, & \frac{\Pi_{ij}}{\delta P_{ij}} < -\frac{1}{2} \\ \frac{\pi}{2\delta P_{ij}} \cdot \cos\left(\pi\left(\frac{\Pi_{ij}}{\delta P_{ij}}\right)\right), & -\frac{1}{2} \leq \frac{\Pi_{ij}}{\delta P_{ij}} \leq \frac{1}{2} \\ 0, & \frac{\Pi_{ij}}{\delta P_{ij}} > \frac{1}{2} \end{cases}. \tag{2.33}$$

Employing the Clausius-Clapeyron relation, the specific entropy contrasts ΔS_{ij} can be expressed in terms of the specific volume contrasts, $\Delta V_{ij} = \Delta(\rho^{-1})_{ij}$, and the Clapeyron slopes γ_{ij} associated with the respective phase transitions,

$$\gamma_{ij} = \frac{dP_{ij}}{dT} = \frac{\Delta S_{ij}}{\Delta V_{ij}} \implies \Delta S_{ij} = \gamma_{ij}\Delta(\rho^{-1})_{ij}. \tag{2.34}$$

Tabulated phase dependent properties

The second approach involves evaluating phase-dependent properties using interpolation tables in the pressure-temperature space, enabling a broader application of mineral physics grounded in semi-empirical lattice vibrational methods [Jacobs and van den Berg, 2011, Jacobs et al., 2013], ab-initio computational data [van den Berg et al., 2019], or thermodynamical calculations [Connolly and Kerrick, 1987, Connolly, 2005]. Within the framework of the current material model, which accounts for multiple components in a mechanical mixture, distinct P,T tables can be utilized for each component. The effective properties are then calculated from the endmember values and weight fractions, applying appropriate mixing formula. For density, we use a mixing formula (eq. 2.22). We represent the specific heat of a mixture as,

[1] Entrophy is defined as

$$S_j = S_{j0} + \sum_{i=1}^{n_{phj}} \Delta S_{ij}\Gamma_{ij} \tag{2.32}$$

$$c_p(X,P,T) = \sum_{j=1}^{n_c} X_j \, c_{p_j}(P,T). \tag{2.35}$$

The thermal expansivity is represented in terms of volume fractions ϕ_j

$$\alpha(X,P,T) = \rho \sum_{j=1}^{n_c} X_j \alpha_j \rho_j^{-1} = \sum_j \phi_j \alpha_j. \tag{2.36}$$

In the majority of our models, we include two material components: one representing basaltic oceanic crust and the other corresponding to general peridotitic mantle material. For the mantle component, we considered the phase transitions at depths of 410 and 660 km, including the effects of latent heat on specific heat and thermal expansivity.

2.3 Numerical solution of the governing equations

To numerically solve the set of equations (eq. 2.1), (eq. 2.3), (eq. 2.6) for velocity and temperature fields, we use finite element methods from the SEPRAN package library [Segal and Praagman, 2005, van den Berg et al., 2015].
The continuity (eq. 2.1) and Stokes equations (eq. 2.3) are solved employing a penalty method [Cuvelier et al., 1986] and Picard iterations [van den Berg et al., 1993, van den Berg et al., 2015].
The energy equation is integrated in time with a predictor - corrector scheme combining implicit Euler and Crank-Nicolson methods [van den Berg et al., 1993].
We employ particle tracer methods to simulate the distribution of material composition and transport of bound and free water. According to equation 2.7, the weight fractions of the material components, X_j, determine $n_c - 1$ invariant degrees of freedom for each particle within a set of n_{trac} tracers. To assess tracer field values, we employed two different approaches as outlined in van Hunen [2001, Appendix A]. The first method involves weighted averaging of tracer values around the evaluation point. The second method, known as particle-in-cell, projects tracer composition values onto an equidistantly spaced grid that covers the model domain, and bi-linear grid interpolation is then used to determine the corresponding composition fields [Hockney and Eastwood, 1988].
The tracer particles are advected by the convection flow field as simulated by the transport equation. We integrate the transport equations for the tracer coordinates by a 2nd or 4th Runge - Kutta method,

$$\frac{dx_{ij}}{dt} = v_j(x_i,t), \quad i = 1,\ldots,n_{\text{trac}}, \quad j = 1,2 \tag{2.37}$$

The velocity values $v_j(x_i)$ are determined by interpolating the finite element velocity field at the positions of the tracers.

In models that incorporate water transport, bound water content in hydrated materials, and the transport of free water with de/rehydration processes, the same set of tracer particles is employed. However, for these models, the tracers

are extended with additional degrees of freedom to accommodate the complexities of water transport.

2.4 Description of the water transport model

Material properties in mantle convection models, particularly rheology and density, depend on mineralogically bound water content (see sections 2.2.3 and 2.2.6). This is important for the dynamics of subduction and on broader scale for exploration of the global scale mantle water cycle which connects ocean and atmosphere with the core and mantle water reservoirs [e.g. Nakagawa and Iwamori, 2019, Nakagawa, 2023].

In our models, water content for the mechanical mixture material is defined using the weight fractions of bound and free water, denoted as $w_{bj}, w_{fj} = 1, ...n_c$, for each of the n_c material components. The combined bound water content w_b in the material mixture medium is represented in terms of weight fractions X_j of the material components,

$$w_b = \frac{m_b}{m} = \sum_{j=1}^{nc} \frac{m_{bj}}{m} = \sum_{j=1}^{nc} \frac{w_{bj} m_j}{m} = \sum_{j=1}^{nc} w_{bj} X_j. \tag{2.38}$$

Here m represents the mass of the material control volume, m_b and m_{bj} refer to the mass values of bound water for the entire mixture and for individual components, respectively. Similarly, the free water associated with the various material components is expressed as,

$$w_f = \sum_{j=1}^{nc} w_{fj} X_j. \tag{2.39}$$

The water weight fractions w_{bj} are represented as variables defined on the particle tracers, similar to material weight fractions X_j.

The bound water is then advected with the tracer particles within the flow field. The capacity of a material component to store bound water depends on pressure and temperature, as described in the water saturation diagrams $S_j(P,T), j = 1, ..., n_c$ (see section 2.5). The saturation S_j represents the maximum possible weight fraction of bound water in material component j. The water content, prescribed on the tracers, is evaluated every integration time step. If $S_j(P,T)$ is lower than the current bound water value w_{bj}, dehydration occurs and bound water reduces by $\Delta w_{bj} = w_{bj} - S_j(P,T)$. Conversely, when free water is available and any material component is undersaturated, the free water is distributed over these components. In case any free water remains after rehydration, it is transported upwards to the surface of the model domain through a free water migration process (see below).

2.4.1 Computation of water transport in the time dependent model

An equidistant spatial grid (referred to as the water grid) is employed to assess water content values in the same manner as the weight fractions of the material components. Tracer values for bound and free water are initially mapped onto the equidistant water grid. Water content values are then determined through bi-linear interpolation from this grid.

The water transport computational framework evolves through four distinct levels. These are respectively, the top level of the full water grid domain, proceeding to individual grid cell level, the tracer particle level, and finally the level of the individual material components of the tracer particles. The water transport computations are organized around the process of upward migration of free water in the following way.

The particle tracers carrying the water fractions w_{bj} are advected with the convective flow every model integration timestep. When particle tracers take a new position relative to the water grid, the tracer water content is cross-checked and equilibrated with the component saturation diagrams $S_j(P,T)$ for the new P- T conditions. Then, any available free water is moved upwards through the water grid column-wise until it reaches the top boundary. The free water migration is carried out in a top-down recursive scheme. Initially, all free water from the top cell is removed from the grid and recorded in a 1-D table that tracks the horizontal distribution of water flux through the top boundary. Subsequently, in a loop through the column cells, starting from the top, the free water from the cell below is transported up one cell level and redistributed among all the tracers in that cell. This is done by extracting all free water from the source cell and injecting it into the target cell as free water, where it is redistributed over all material components of the tracers, based on their saturation diagrams (see Fig. 2.1).

The approach described above results in the vertical transport of free water. This single-cell method is repeated multiple times to enable longer water migration paths per integration time step. This iterative multi-cell scheme utilizes a fixed water migration velocity u_{fw} as an input parameter. The number of migration steps per integration time step, $n_{step} = \frac{u_{fw}\Delta t}{\Delta y}$, varies with the grid cell size Δy and the variable, CFL controlled, time step Δt. Water migration scheme is illustrated in Appendix A in terms of simple kinematic lid-driven models.

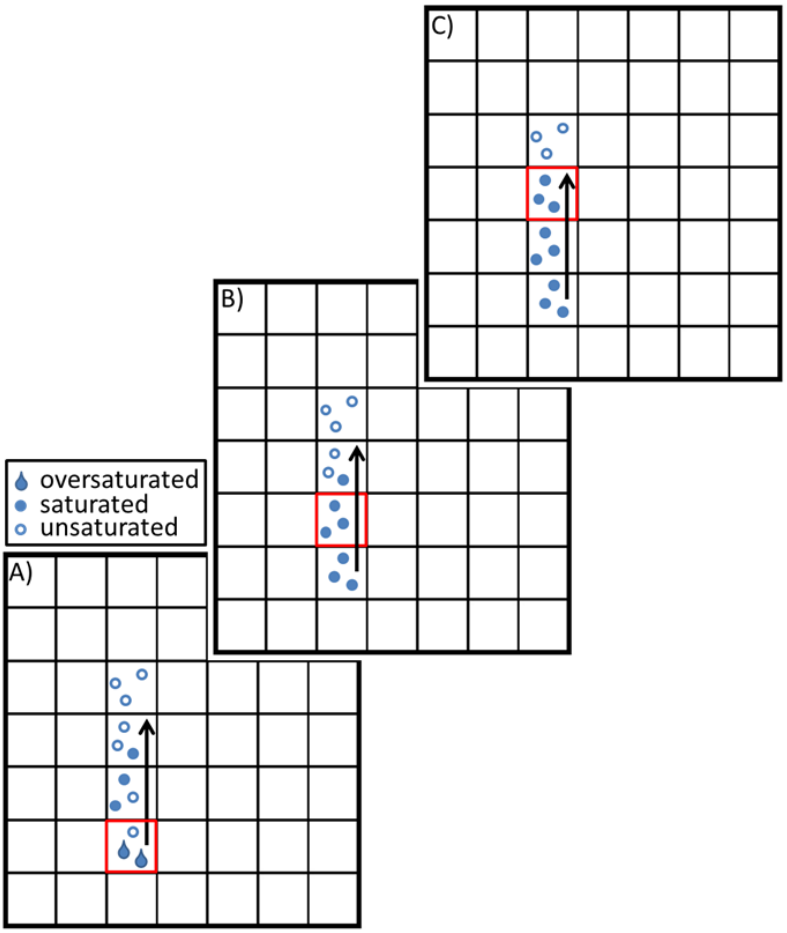

Figure 2.1: Cartoon scheme of the water migration through the cells of the background grid. Water drops represent oversaturated tracers, full blue dots are saturated tracers and blue circles are unsaturated tracers. The black vector represents the maximum possible distance that water can travel within the given integration time step. Panels A) - C) represent individual steps of dehydration and hydration within one time step related to red marked cells.

Formulation of the computational scheme

Let us now describe this approach in more detail. Subscripts i, j here used as indices, stand for tracers and material components respectively.

1. Domain level
   Free water migration is performed across the entire domain by iterating through the water grid columns and top-down loops over the grid cells within each column. During this process, the amount of free water present in a specific source grid cell, referred to as $m_{f_{inject}}$, is assessed and then migrated upward by injecting it into the target cell directly above.

2. Level of individual grid cells
   Free water injected to the target cell is redistributed over all N_c^{trac} tracers in a loop in the following steps.

   - First, for each tracer in the injected cell the water storage capacity w_{ui} or free water content w_{fi}, both expressed as weight fractions, are deter-

mined. The respective water amounts are calculated by multiplication by the tracer representative mass value as,

$$m_{ui} = w_{ui} m_i,\ m_{fi} = w_{fi} m_i. \tag{2.40}$$

Here tracer mass m_i is represented by the tracer compound density ρ_i and volume V_i as,

$$m_i = \rho_i V_i = \rho_i V_{cell} / N_c^{trac}. \tag{2.41}$$

Finally, the mass of the entire cell is given as,

$$m_c = \sum_i m_i. \tag{2.42}$$

Respective water amounts in the target cell are,

$$m_{uc} = \sum_{i=1}^{N_c^{trac}} m_{ui},\ m_{fc} = \sum_{i=1}^{N_c^{trac}} m_{fi}. \tag{2.43}$$

- It follows that the total amount of free water that is available in the injected target cell for redistribution is given as injected water and free water that was already there

$$m_{fa} = m_{f_{inject}} + m_{fc}. \tag{2.44}$$

The amount of free water that is subsequently bound in the tracers is

$$\delta m_{bc} = \min(m_{fa}, m_{uc}). \tag{2.45}$$

The rest of the water is distributed as free water over the tracers

$$\delta m_{fc} = m_{fa} - \delta m_{bc}. \tag{2.46}$$

- In case undersaturation occurs on a cell level, with $m_{uc} > 0$, fraction of the available water for rehydration, m_{fa}, is bound on individual tracers i, proportional to the degree of undersaturation as

$$\delta m_{bi} \equiv \delta m_{bc} \cdot \frac{m_{ui}}{m_{uc}}. \tag{2.47}$$

If any water remains after the rehydration step, it is distributed over the tracers in the injected target cell, proportionally to their mass as

$$\delta m_{fi} \equiv \delta m_{fc} \cdot \frac{m_i}{m_c}. \tag{2.48}$$

- The total amount of bound and free water, that tracer i accommodates, is initially specified as

$$\delta m_{wi} = \delta m_{bi} + \delta m_{fi}. \tag{2.49}$$

This combined amount of water δm_{wi} is added to the tracer free water weight fraction as

$$w_{fi} \Rightarrow w_{fi} + \frac{\delta m_{wi}}{m_i} \tag{2.50}$$

and is re-equilibrated over the material components.

3. Level of material components of individual tracer particles

Redistribution of water on tracer i on a component level j is done during tracer equilibration after water is added to the tracer water content in the following steps:

- The saturation level of material components j is assessed by determining the weight fraction of bound water, w_{bij}, and the weight fractions of either undersaturation

$$w_{uij} = S_j - w_{bij} \tag{2.51}$$

or oversaturation

$$w_{oij} = \begin{cases} 0, & S_j - w_{bij} > 0 \\ w_{bij} - S_j, & S_j - w_{bij} < 0 \end{cases}. \tag{2.52}$$

Here $S_j(P,T)$ are water saturation diagrams of respective material components.

- The total weight fraction of water available for redistribution over the material components j is

$$w_{ai} = w_{fi} + w_{oi}. \tag{2.53}$$

The amount of water to be stored as bound water, constrained by the storage capacity, is determined by

$$\delta w_{bi} = min(w_{ai}, w_{ui}). \tag{2.54}$$

The remaining water is kept as tracer compound free water

$$\delta w_{fi} = w_{ai} - \delta w_{bi}. \tag{2.55}$$

- Water is allocated to the material components based on their storage capacities, and components that are oversaturated release excess water until they reach their saturation level as

$$\delta w_{bij} = \begin{cases} \frac{w_{uij}}{w_{ui}} \times \delta w_{bi}, & w_{uij} > 0 \\ -w_{oij}, & w_{oij} > 0 \end{cases}. \tag{2.56}$$

Finally, the updated bound water amount on the component level is

$$w_{bij} \Rightarrow w_{bij} + \delta w_{bij}. \tag{2.57}$$

2.5 Saturation diagrams

When incorporating dehydration and water transport into numerical models of subduction, saturation diagrams that specify maximum amount of bound water in material at given PT conditions, need to be provided. Saturation diagrams describe the stability fields of the mineral assemblages as a function of pressure and temperature. Each of the mineral assemblages is able to accommodate certain amount of bound water. The boundaries between the stability fields of the saturation diagram mark where the phase change from one mineral assemblage to another takes place. This phase change is usually accompanied by a change of the bound water content.

Saturation diagrams are either based on thermodynamical calculations or are obtained experimentally. Perple_X [Connolly, 2005, Connolly and Kerrick, 1987] is a widely used software package for thermodynamical calculations, based on minimizing Gibbs free energy to obtain stable mineral assemblages (chemical equilibrium). The limitation of these calculations concerning H_2O may lie in the thermodynamic datasets depth validity. Most of the commonly used datasets are valid only to the depths <410 km [e.g. Holland and Powell, 1998]. Thermodynamic datasets encompass various information, such as the inventory of system components with their respective molar weights, standard state properties like heat capacity, entropy, and enthalpy, as well as data on heat capacity and volumetric functions specific to individual phases and chemical species. In our models we employ saturation diagrams based on high pressure experiments [Iwamori, 2004, 2007], that are valid up to 25 GPa ($\sim$ 700 km).

2.5.1 Crustal material saturation diagram

The crustal material is represented by the saturation diagram (Fig. 2.2) of Iwamori [2007], based on experiments of Schmidt and Poli [1998]. These experiments were conducted on a MORB - like bulk composition ($SiO_2 - Al_2O_3 - FeO - MgO - CaO - Na_2O - H_2O$) at pressures ranging from 1.8 to 12 GPa and temperatures between 850 K and 1400 K with 5 wt% H_2O saturation at pressures to 4 GPa and 2 or 1 wt% H_2O at higher pressures. Since all of the experiments contained omphacite and garnet (eclogitic assemblage), numerous hydrous minerals were present at pressures exceeding the stability range of amphibole. These include lawsonite, zoisite, chloritoid (potentially talc or staurolite).

The saturation diagram of a basaltic system (Fig. 2.2) shows continuous changes in water saturation in comparison to the sharp boundaries in the peridotitic system (Fig. 2.3). This is caused by the presence of numerous H_2O-related reactions (incorporating, e.g. lawsonite, amphibole, talc, phengite and chlorite) with solid solutions [Schmidt and Poli, 1998, Iwamori, 1998, Ono, 1998]. At low pressures (< 2 GPa) and temperatures (< 700 K), more than 5wt% of bound water can be stored in the crustal material. Significant reduction in H_2O content is observed at $\sim$ 2.5 GPa, where dehydration of amphibolite results in the formation of eclogite, and lawsonite becomes the major hydrous phase in the system. Water content also decreases with increasing temperature for T > 800 K in the low pressure re-

gion (< 2.5 GPa), where amphibole is dominating as a hydrous phase and starts to decompose.

Experiments of Schmidt and Poli [1998] were conducted for pressures ≤ 10 GPa and temperature ≤ 1273 K. In [Iwamori, 2004, 2007] this limited range was extended to 25 GPa in pressure and 2500 K in temperature by employing linear extrapolation. Water content for temperatures above 1273 K and pressure over 10 GPa was assumed to be zero.

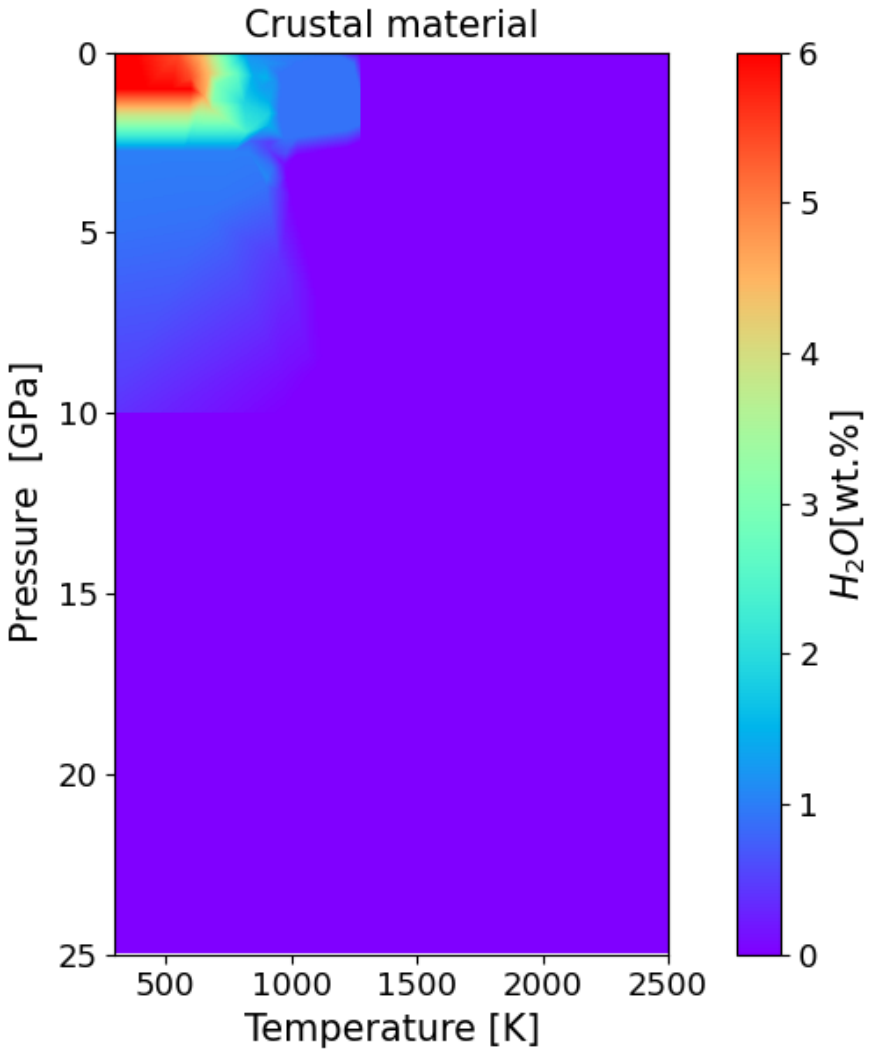

Figure 2.2: Saturation H_2O diagram of the solid phases of a MORB composition as a function of pressure (0 - 25 GPa) and temperature (300 - 2500 K) [Iwamori, 2007], originated from [Schmidt and Poli, 1998, Iwamori, 1998].

2.5.2 Mantle material saturation diagram

To track water in mantle material, we employ a phase (saturation) diagram from Iwamori [2004, 2007] for peridotitic rocks (Fig. 2.3). This saturation diagram has been adapted by combining stability field of multiple peridotite systems [Iwamori, 2004, Kawamoto, 2004, Komabayashi et al., 2004]: $MgO - Al_2O_3 - SiO_2 - H_2O$ [e.g. Fockenberg, 1998, Pawley, 2003], $MgO - SiO_2 - H_2O$ [e.g. Kanzaki,

1991, Ohtani et al., 2001] and KLB-1 natural peridotitic system [e.g. Kawamoto et al., 1995, Hirose, 2002, Kawamoto, 2004]. The maximum H_2O content of these mineral assemblages (Fig. 2 in Iwamori [2007]) was calculated utilizing a least squares calculation in accordance with mass balance [Schmidt and Poli, 1998].

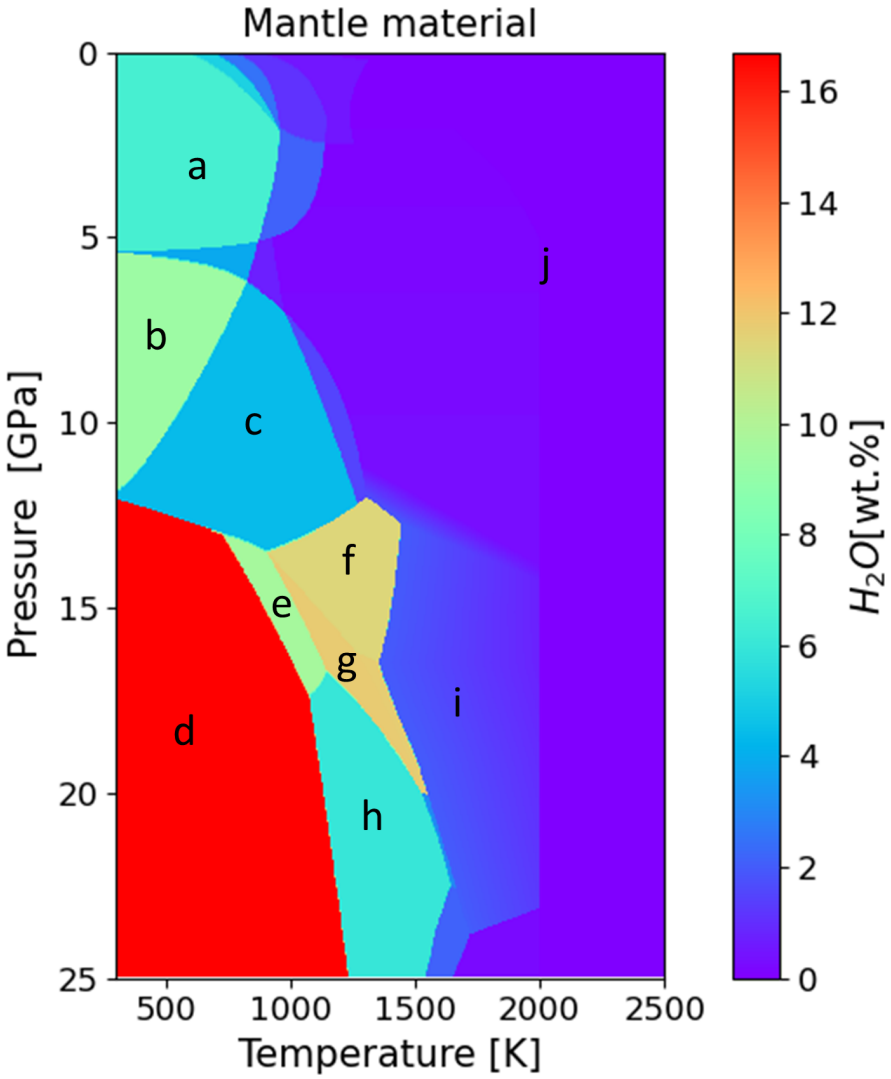

Figure 2.3: Saturation H_2O diagram of the solid phases of peridotitic mantle as a function of pressure (0 - 25 GPa) and temperature (300 - 2500 K) [Iwamori, 2004, 2007]

The stability fields in the saturation diagram (Fig. 2.3) correspond to stability of serpentine and chlorite at temperatures $< 900 - 1000$ K and pressures < 5 GPa with a maximum H_2O saturation of ~ 7 wt% (field a in Fig. 2.3). At low pressures < 5GPa, and higher temperatures $> 900 - 1000$ K these two minerals are not stable and no other hydrous phases are present in the peridotitic rocks (field j in Fig. 2.3). Consequently, water saturation at these PT conditions is close to 0 wt%. In the hydrous mineral family, serpentine and chlorite are identified as main players in the subduction zones. At higher pressures over 10 GPa and temperatures up to $1300-1500$ K DHMS phases are stable (fields b-i in Fig. 2.3), namely, phase A, phase E, superhydrous phase B and phase D. By the presence of these DHMS phases, peridotite is able to accommodate over 10wt% of H_2O.

Maximum possible H_2O content decreases when the major hydrous phases are no longer stable. Above the pressure and temperature of the DHMS stability fields (fields b-i in Fig. 2.3), peridotites may still accommodate H_2O in the nominally anhydrous minerals. These come into play particularly in the PT conditions of the transition zone. There (field i in 2.3) wadsleyite and ringwoodite (both polymorphs of olivine) are able to contain $2-3$wt% of H_2O [Kohlstedt et al., 1996, Inoue et al., 1995, Litasov et al., 2003]. Since solubility of H_2O decreases with temperature in wadsleyite and ringwoodite, the water content of the peridotitic rocks in the transition zone decreases with temperature from 2wt% at the top of the transition zone to 0wt% at the boundary between the transition zone and lower mantle, where majority of the DHMS phases are not stable anymore. Above 2000 K water content is 0wt%.

2.5.3 Saturation diagrams in our numerical models

In the numerical experiments, presented in chapter 6 we are employing experimentally constrained saturation diagrams of Iwamori [2004, 2007] (Figs 2.2, 2.3). The depth of our numerical models (2000 km) spans larger pressure range than the original diagrams which are available for the upper mantle and transition zone only. We, therefore, assume that saturation beyond P,T conditions of Iwamori [2007] is 0wt%. For the computational purposes these saturation diagrams were prepared in the form of P - T - H_2O saturation look-up tables with a 2.2 K step in temperature and 0.035 GPa step in pressure.

3. Feedbacks between subduction dynamics and slab deformation: combined effects of nonlinear rheology of a weak decoupling layer and phase transitions

This chapter was published as [Pokorný et al., 2021] in Physics of the Earth and Planetary Interiors

3.1 Introduction

The main source of information about the deformation of subducting slabs in the Earth mantle is seismic tomography [Bijwaard et al., 1998, Fukao and Obayashi, 2013, Zhao et al., 2017, van der Meer et al., 2018]. It shows that though some subducting slabs directly penetrate the lower mantle, in most subduction areas they are significantly deformed in the lower part of the upper mantle and at least temporarily delayed in this region [Goes et al., 2017]. Subduction of lithospheric plates is a highly complex geodynamical problem affected by many factors and the effects that control slab stagnation/penetration have been studied in numerous modeling studies. The primary control is exerted by slab and mantle rheology [e.g. Čížková et al., 2002, Billen and Hirth, 2007] and effects of phase transitions [e.g. Christensen, 1996, Schmeling et al., 1999, van Hunen et al., 2001, Bina et al., 2001, Torii and Yoshioka, 2007, Billen, 2010, Arredondo and Billen, 2017, Holt et al., 2015, Faccenda and Zilio, 2017, Goes et al., 2017]. As the slab stagnation/penetration is closely related to trench migration [Čížková and Bina, 2019], also the processes occuring at shallow depths such as e.g. dehydratation of the subducting material that affects both viscosity and density in proximity of the slab at shallow depths [Arcay et al., 2005, Iwamori, 2007, Duarte et al., 2015, Nakao et al., 2016, 2018], slab stiffness and its viscosity contrast with respect to the mantle [e.g. Ribe, 2010, Stegman et al., 2010] or the properties of the overriding plate [Garel et al., 2014, Holt et al., 2015] were shown to play important role.

Among other parameters, the properties of the mechanical decoupling between subducting and overriding plate have been shown to have major influence on the subducting slab behavior. A thin weak layer, often refered to as the crust, lowers the friction at the contact and facilitates subduction [Běhounková and Čížková, 2008, Chertova et al., 2012, Agrusta et al., 2014]. The decoupling effect of such a weak zone may be affected by the abundance of sediments on the top of the subducting plate. Presence of the sedimentary layer may reduce the weak zone viscosity by 1-2 orders of magnitude relative to the astenosphere.

This softening allows faster plate velocities and can thus affect the whole subducting dynamics [Behr and Becker, 2018]. Models with constant crustal viscosity have already shown, that magnitude of the crustal viscosity plays an important role in determining the subducting plate velocity [Androvičová et al., 2013] and also in terms of its deformation in the transition zone and the ability of the slab to penetrate the lower mantle[Čížková and Bina, 2013, Goes et al., 2017]. Furthermore low-viscosity crust allows effective decoupling of the plates and results in faster rollback. Enhancement of rollback is associated with stagnation of the slab above the endothermic phase transition at 660 km depth [Torii and Yoshioka, 2007, Agrusta et al., 2017, Čížková and Bina, 2019]. On the other hand high-viscosity of the crust suppresses rollback and thereby facilitates slab penetration into the lower mantle.

Here we will further elaborate on the effects of the rheological properties of the (crustal) decoupling layer to the slab deformation. First, we will discuss in more detail the models with constant crustal viscosity and demonstrate the effects of its thickness. We will quantify the combined effect of these two parameters on the slab behavior by introducing a resistance parameter that controls the lubricating effect of a weak crustal layer, and evaluate slab stagnation/penetration in connection with this crustal resistance.

Using constant crustal viscosity may be a numerical convenience that allows plate decoupling without reflecting the real constitution law of crustal materials. It has however been shown in crustal rock experiments that crust deforms nonlinearly under the temperature and pressure conditions of subduction [Ranalli, 1995, Shelton and Tullis, 1981]. Therefore in the second part of the paper we will assume that the crustal layer deforms nonlinearly through dislocation creep and stress-limiting Byerlee type pseudoplastic deformation. We will then demonstrate how the feedback between slab velocity and a nonlinear strainrate dependent crustal viscosity affects slab penetration/stagnation at 660 km depth. Finally, we will adress the effect of phase transitions in the models with nonlinear crustal rheology.

3.2 Model setup

We solve the system of partial differential equations describing convection in the Earth's mantle in an extended Boussinesq approximation [EBA, Ita and King, 1994] without internal heating. Numerical solution of the governing equations is obtained with the SEPRAN finite element toolkit [Segal and Praagman, 2005, van den Berg et al., 2015].

Our 2D Cartesian model domain is 10 000 km wide and covers a region from the surface to 2000 km depth. The subducting lithospheric plate stretches from a mid-ocean ridge situated in the upper left corner to the trench located in the middle of the model domain. The age of the subducting plate follows a halfspace model and reaches the age of 100 Ma at the trench. The overriding plate stretches from the second mid-ocean ridge in the upper right corner and has the same age as the subducting plate. An initial temperature distribution (Fig. 3.1a)

is obtained in a short (6 Ma) preliminary run where a constant convergence velocity of 2.5 cm/year is prescribed on the top of the subducting plate. During this pre-run the tip of the subducting plate is driven to a depth of 200 km (Fig. 3.1a). Then the kinematic boundary condition is switched off and an impermeable free slip is prescribed on all boundaries. Thermal boundary conditions include reflective side boundaries and constant temperature prescribed at the top (273 K) and at the bottom of the model domain (2132 K). Density anomalies in our EBA model are linearly proportional to temperature anomalies with reference density $\rho_0 = 3416\,\mathrm{kg/m^3}$ and depth dependent thermal expansivity [Katsura et al., 2009]. Thermal expansivity varies with depth from $3 \times 10^{-5}\,\mathrm{K^{-1}}$ at the surface to $1.2 \times 10^{-5}\,\mathrm{K^{-1}}$ at the depth of 2000 km at the bottom of the model domain [Hansen et al., 1993]. Thermal diffusivity is held constant $10^{-6}\,\mathrm{m^2\,s^{-1}}$. An increase of initial temperature with depth is illustrated in Fig. 3.1b.

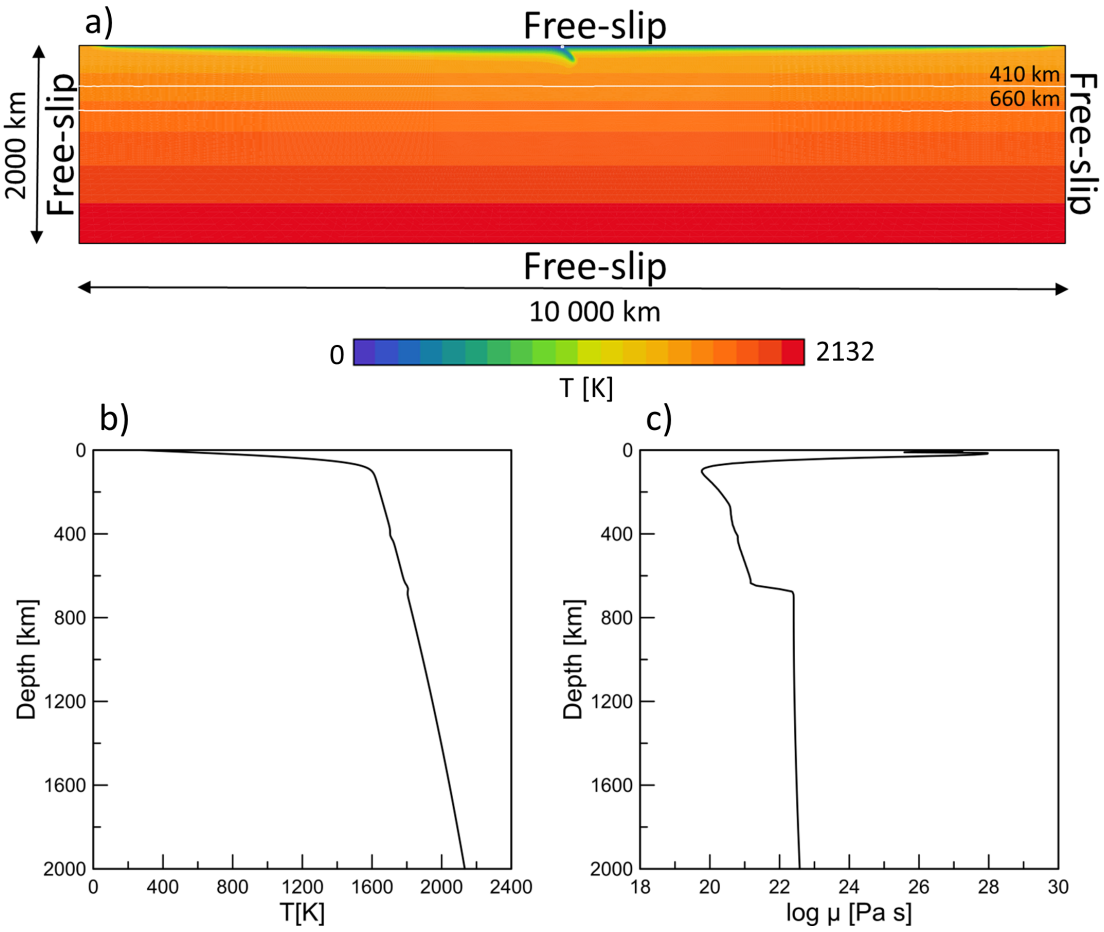

Figure 3.1: Panel a): Model setup and initial temperature. Model domain is 2000 km deep and 10000 km wide. At all boundaries an impermeable free slip is prescribed. White lines indicate the position of the major mantle phase transitions. Panel b): Vertical profile of temperature at x=2000 km from the ridge. Panel c): Vertical profile of viscosity at x=2000 km from the ridge.

Mechanical decoupling of the two plates is facilitated by a low-viscosity layer prescribed on the top of the subducting plate. Such a weak layer is often used in subduction modeling as a numerical convenience that allows relative sliding of the two plates. It should mimick the effects of a weak crust that has rather complex structure with a fine sediment layer at the top and presumably upper and lower crustal layers with different rheological properties underlying it [Liao et al., 2017]. In the present paper we approximate this complex decoupling structure by a single layer of weak material with uniform properties. The crustal material is advected using 10^6 material tracers initially positioned within the crust and its near neighbourhood. Crustal tracers are laid along the surface of the subducting plate from the mid-ocean ridge in the upper-left corner to the trench at the contact of subducting and overriding plates 5000 km from the ridge. Crustal tracers are not being added during the model evolution which means that when this 5000 km long subducting plate was subducted and all weak crust was consumed, the subducting plate would get locked and subduction would terminate. All our model runs are stopped before that moment. At the depth of 150 km where the decoupling effect of a weak layer is no more needed, the viscosity of the decoupling layer is replaced by mantle viscosity for numerical convenience. Spatial resolution of the finite element mesh varies within the model domain. Maximum resolution of 3 km is in the contact area of the plates up to the depth of 200 km, the resolution in the transition zone and upper part of the lower mantle is 10 km and then the element size is growing towards the boundaries of the model domain. The main mantle phase transitions, i.e. exothermic at 410 km depth, where the polymorphous transition from forsterite to wadsleyite takes place, and endothermic at 660 km depth, where ringwoodite changes to bridgmanite and periclase, are included in the model. We take into account both the buoyancy and latent heat effects associated with these transitions. Since the limitation of mantle material to olivine may overestimate the effects of the phase transition [Arredondo and Billen, 2016] and taking into account the uncertainties in the evaluation of the Clapeyron slopes, we test its effects by varying both γ_{410} (1 MPa/K, 2MPa/K) and γ_{660} (-1.5 MPa/K, -2.5 MPa/K). Density contrast associated with the 410 km and 660 km phase transitions is 8 and 10% respectively (see table 3.1). Phase transitions are implemented using a phase function [Christensen and Yuen, 1985] with harmonic parameterization [Čížková et al., 2007].

In order to evaluate some characteristic model quantities in the postprocessing phase we make use of passive (monitor) material tracers. A first group of these monitor tracers is prescribed in the crust and is used to calculate the average viscosity of this decoupling layer. Initially 8000 tracers are evenly distributed within the crust. In order to calculate the average viscosity at the contact of the plates, we divide all crustal tracers that are at certain moment in the depth interval of 15-100 km into 15 km depth subintervals and calculate the harmonic average of viscosity in these subintervals. Geometric mean of these values is then used to produce one characteristic crustal viscosity. The second group of passive tracers is placed within the subcrustal subducting lithospheric plate. These tracers are then used to determine the penetration depth of the slab. In every timestep we simply identify the deepest tracer from this second group. Finally, a single tracer initially positioned in the overriding plate to the right from the trench is used to monitor trench velocity.

Table 3.1
Model parameters

symbol	Meaning	Value	Units
Upper mantle rheology			
A_{diff}	Pre-exponential parameter of diffusion creep[a]	1×10^{-9}	$Pa^{-1}\ s^{-1}$
A_{disl}	Pre-exponential parameter of dislocation creep[a]	31.5×10^{-18}	$Pa^{-n}\ s^{-1}$
E_{diff}	Activation energy of diffusion creep[a]	3.35×10^{5}	$J\ mol^{-1}$
E_{disl}	Activation energy of dislocation creep[a]	4.8×10^{5}	$J\ mol^{-1}$
V_{diff}	Activation volume of diffusion creep[a]	4.0×10^{-6}	$m^3\ mol^{-1}$
V_{disl}	Activation volume of dislocation creep[a]	11×10^{-6}	$m^3\ mol^{-1}$
η_{diff}	Viscosity of diffusion creep	–	$Pa\ s$
η_{disl}	Viscosity of dislocation creep	–	$Pa\ s$
η_y	Power-law stress limitor viscosity	–	$Pa\ s$
n	dislocation creep exponent	3.5	–
$\dot{\epsilon}_y$	Reference strain rate	1×10^{-15}	s^{-1}
σ_y	Stress limit	$2 - 5 \times 10^{8}$	Pa
p	Hydrostatic pressure	–	Pa
n_y	Stress limit exponent	10	–
R	Gas constant	8.314	$J\ K^{-1}\ mol^{-1}$
T	Temperature	–	K
$\dot{\epsilon}_{\|\|}$	Second invariant of strainrate	–	s^{-1}
Lower mantle rheology			
A_{diff}	Pre-exponential parameter of diffusion creep	1.3×10^{-16}	$Pa^{-1}\ s^{-1}$
E_{diff}	Activation energy of diffusion creep[b]	2×10^{5}	$J\ mol^{-1}$
V_{diff}	Activation volume of diffusion creep[b]	1.1×10^{-6}	$m^3\ mol^{-1}$
Other model parameters			
κ	Thermal diffusivity	10^{-6}	$m^2\ s^{-1}$
g	Gravitational acceleration	9.8	$m^2\ s^{-2}$
ρ_0	Reference density	3416	$kg\ m^{-3}$
c_p	Specific heat	1250	$J\ kg^{-1}\ K^{-1}$
α_0	Surface thermal expansivity	3×10^{-5}	K^{-1}
γ_{410}	Clapeyron slope of 410 km phase transition[c]	$1 - 2 \times 10^{6}$	$Pa\ K^{-1}$
γ_{660}	Clapeyron slope of 660 km phase transition[c]	$(-1.5) - (-2.5) \times 10^{6}$	$Pa\ K^{-1}$
$\delta_{\rho 410}$	Density contrast of 410 km phase transition[d]	273	$kg\ m^{-3}$
$\delta_{\rho 660}$	Density contrast of 660 km phase transition[d]	341	$kg\ m^{-3}$

[a] Parameters of wet olivine based on Hirth and Kohstedt (2003).
[b] Čížková et al. (2012).
[c] Bina and Helffrich (1994).
[d] Steinbach and Yuen (1995).

3.3 Rheology

In our models we assume two materials, mantle (including the lithospheric plates) and crust. The rheology of the mantle material is described by a composite model [van den Berg et al., 1993, Čížková et al., 2002], where the effective viscosity combines three deformation mechanisms: diffusion creep, dislocation creep and a power-law stress limiter as an approximation of Peierls creep [Androvičová et al., 2013]. The viscosities of the individual creep mechanisms are defined as follows. Diffusion creep viscosity is

$$\eta_{diff} = A_{diff}^{-1} \exp\left(\frac{E_{diff} + pV_{diff}}{RT}\right), \tag{3.1}$$

Where A_{diff} is pre-exponential parameter of diffusion creep, E_{diff} is activation energy of diffusion creep, p is hydrostatic pressure, V_{diff} is activation volume of diffusion creep, R is the gas constant and T is the absolute temperature. Dislocation creep viscosity is defined as:

$$\eta_{disl} = A_{disl}^{-1/n} \, \dot{\epsilon}_{\|}^{(1-n)/n} \, \exp\left(\frac{E_{disl} + pV_{disl}}{nRT}\right). \tag{3.2}$$

Here A_{disl}, E_{disl} and V_{disl} are pre-exponential parameter, activation energy and activation volume of dislocation creep, $\dot{\epsilon}_{\|}$ is the second invariant of the strain rate tensor and the exponent $n = 3.5$ [Kameyama et al., 1999]. Finally the power-law stress limiter viscosity is formulated as:

$$\eta_y = \sigma_y \dot{\epsilon}_y{}^{-(1/n_y)} \, \dot{\epsilon}_{\|}^{(1/n_y)-1} \tag{3.3}$$

where $\dot{\epsilon}_y$ is a reference strain rate and σ_y is the corresponding stress limit. The exponent n_y is usually taken within the range of 5-10, here we apply $n_y = 10$. The stress limit is based on stress estimates in the subducting slab. Values are usually in the range of $0.1 - 1$ GPa. Here we mostly use $\sigma_y = 0.2$ GPa, but some tests are also performed for $\sigma_y = 0.5$ GPa. Parameters of the above mechanisms are based on experiments on olivine [Hirth and Kohlstedt, 2003a] and are specified in table 3.1. Viscosities of individual creep mechanisms are combined into an effective viscosity as

$$\frac{1}{\eta_{eff}} = \frac{1}{\eta_{diff}} + \frac{1}{\eta_{disl}} + \frac{1}{\eta_y} + \frac{1}{\eta_{max}}, \tag{3.4}$$

where the maximum cut-off viscosity $\eta_{max} = 10^{29}$ Pa s. In the lower mantle the deformation is assumed to be predominantly through diffusion creep [Karato et al., 1995]. We therefore take $\eta_{eff} = \eta_{diff}$ in the lower mantle with parameters based on slab sinking speed analysis [Čížková et al., 2012]. The viscosity increase at 660-km interface $\Delta\eta_{660} \sim 20$ (Fig. 3.1c).

The primary focus of the present paper is to demonstrate the effects of rheological description of the decoupling crust. To that end we perform numerical experiments in two groups of models. For reference we first run numerical experiments in a series of models with a constant crustal viscosity and we vary both the thickness of the crustal layer and its viscosity. Crustal material is prescribed in a layer of constant thickness positioned along the surface of the subducting plate and along an arc that separates the subducting and overriding plates. We test three initial thicknesses of this compositionally different material (7, 10 and 15 km) and three values of its constant viscosity $10^{20}, 5 \times 10^{20}$ and 10^{21} Pa s. In this group of 9 models we evaluate the combined effects of the crustal viscosity and thickness on the slab deformation and its ability to penetrate the lower mantle. Sandiford and Moresi [2019] have demonstrated that the thickness of the weak decoupling layer varies during the slab evolution, it is therefore problematic to use the initial thickness of the compositionally different crust as a measure of the weak layer. Furthermore, in order to obtain viscosity in the vicinity of the boundary between the crustal and lithospheric material, we apply harmonic averaging of their viscosities weighted with the volume fraction of crustal/mantle material.

This averaging prefers lower (crustal) viscosity and thus effectively makes the decoupling (low viscosity) layer thicker than is the layer of the compositionally distinct crustal material. Therefore we will refer to the thickness of the model crust as 'thin', 'intermediate' and 'thick' and we will report time variations of its effective thicknes d_{cr}^{eff} measured during the calculation (the thickness of the low viscosity chanel at the depth of 40 km taken perpendicular to the slab direction).

The main focus of this paper are the models of the second group. In these models the crustal layer has a composite nonlinear rheology that combines dislocation creep [Ranalli, 1995] and a Byerlee type deformation component [Karato, 2008] as an approximation of brittle failure, further referred to as pseudoplastic deformation. Similarly to mantle material (eq. (2) above), dislocation creep viscosity is defined as

$$\eta_{disl}^{c} = A_c^{-1/n_c}\, \dot{\epsilon}_{\parallel}^{(1-n_c)/n_c}\, \exp\left(\frac{E_c + pV_c}{n_c RT}\right). \tag{3.5}$$

Here A_c,n_c,E_c and V_c are pre-exponential parameter, exponent, activation energy and activation volume of the dislocation creep in the crust. Pseudoplastic deformation is defined by the viscosity component η_{pl}:

$$\eta_{pl} = \frac{\sigma_y^c}{2\dot{\epsilon}_{\parallel}}\,, \tag{3.6}$$

where σ_y^c is stress limit in the crust. This stress limit σ_y^c increases with lithostatic pressure as

$$\sigma_y^c = \tau_c + \mu p\,. \tag{3.7}$$

Here τ_c is the cohesion and μ friction coefficient. Crustal effective viscosity is then calculated as

$$\frac{1}{\eta_{eff}^{c}} = \frac{1}{\eta_{disl}^{c}} + \frac{1}{\eta_{pl}} \tag{3.8}$$

Parameters of both deformation mechanisms are given in table 3.2. In order to assess the sensitivity of the results to parameter choice, we evaluate several models. In the reference model PwlM1 the parameters of both dislocation creep and pseudoplastic deformation are based on experiments on quartzite [Liao et al., 2017, Ranalli, 1995]. Models PwlM2 and PwlM3 have modified parameters of the pseudoplastic deformation (see table 3.2) and yield lower and higher viscosities η_{pl} than the reference model. The influence of the dislocation creep parameters was further tested in model PwlM4 where we used dislocation creep parameters based on the experiments on diabase [Shelton and Tullis, 1981] which is compositionally equivalent to volcanic basalt or plutonic gabbros present in the oceanic crust. All model experiments with the nonlinear crustal model were carried out with intermediate crustal thickness and mantle material yield stress σ_y (eq.(3)) of 0.2 GPa.

Table 3.2
Models with nonlinear crustal rheology

Symbol	Meaning	PwlM1	PwlM2	PwlM3	Units
A_c	Pre-exponential parameter of dislocation creep	2.5×10^{-17}	2.5×10^{-17}	2.5×10^{-17}	$Pa^{-1}\ s^{-1}$
E_c	Activation energy of dislocation creep	1.54×10^5	1.54×10^5	1.54×10^5	$J\ mol^{-1}$
V_c	Activation volume of dislocation creep	0	0	0	$m^3\ mol^{-1}$
n_c	dislocation creep exponent	2.3	2.3	2.3	–
τ_c	Cohesion	1×10^7	0.5×10^7	2×10^7	Pa
μ_c	Friction coefficient	0.1	0.05	0.2	–
γ_{410}	Clapeyron slope 410 km phase transition	2	2	2	MPa/K
γ_{660}	Clapeyron slope 660 km phase transition	-2.5	-2.5	-2.5	MPa/K
		PwlM4	PwlM1_0PT	PwlM1_660	Units
A_c	Pre-exponential parameter of dislocation creep	8.8×10^{-25}	2.5×10^{-17}	2.5×10^{-17}	$Pa^{-1}\ s^{-1}$
E_c	Activation energy of dislocation creep	2.6×10^5	1.54×10^5	1.54×10^5	$J\ mol^{-1}$
V_c	Activation volume of dislocation creep	10	0	0	$m^3\ mol^{-1}$
n_c	dislocation creep exponent	3.4	2.3	2.3	–
τ_c	Cohesion	2×10^7	1×10^7	1×10^7	Pa
μ_c	Friction coefficient	0.2	0.1	0.1	–
γ_{410}	Clapeyron slope 410 km phase transition	2	0	0	MPa/K
γ_{660}	Clapeyron slope 660 km phase transition	-2.5	0	-2.5	MPa/K

3.4 Results

3.4.1 Constant viscosity crust

Previous work has shown that a constant viscosity of the crust has a significant influence on the velocity of the subducting plate [Androvičová et al., 2013] and also on its deformation in the transition zone and ability to penetrate the lower mantle [Čížková and Bina, 2013, Goes et al., 2017, Čížková and Bina, 2019]. In the first group of our experiments we will further evaluate the combined effects of crustal thickness and its (constant) viscosity. We will demonstrate a trade-off between these two parameters. To that end we performed nine model runs with three different values of constant crustal viscosity $10^{20}, 5 \times 10^{20}$ and 10^{21} Pa s and three values of initial crustal thickness - 7, 10 and 15 km (refered to as thin, intermediate and thick further on). The stress limit of the mantle material was 0.2 GPa in these experiments. For all models from this group we used the same values of Clapeyron slopes ($\gamma_{410} = 2$MPa/K and $\gamma_{660} = -2.5$MPa/K).

Evolution of two models - with weak (10^{20} Pas) and strong (10^{21} Pas) crust - is shown in Fig. 3.2. Both models have intermediate crustal thickness. Panels 2a-2c show three snapshots that illustrate the model with weak crust. It reaches the endothermic phase boundary at 660-km depth after 4 Ma evolution from the initial state (Fig. 3.1a). Slab material in the transition zone squeezed between the extra negative buoyancy of the 410-km elevation and positive buoyancy of the depressed 660-km phase transition is weakened thanks to the nonlinear mantle rheology and forms a first buckle. After that the slab buckles quasiperiodically and remains stagnant in the transition zone (Fig. 3.1bc). During buckling, the slab oscillates between stages of fast rollback (3 - 5 cm/year) when new buckles start and stages of limited or no rollback while buckles are being tightened when the bottom of buckle approaches the 660-km boundary [Čížková and Bina, 2013]. Slab dip angle oscilates between the values of ∼30 deg and 70 deg (Fig. 3, solid red line), low dip angle being associated with faster trench rollback and vice versa (cf. Fig. 3.3, solid black line).

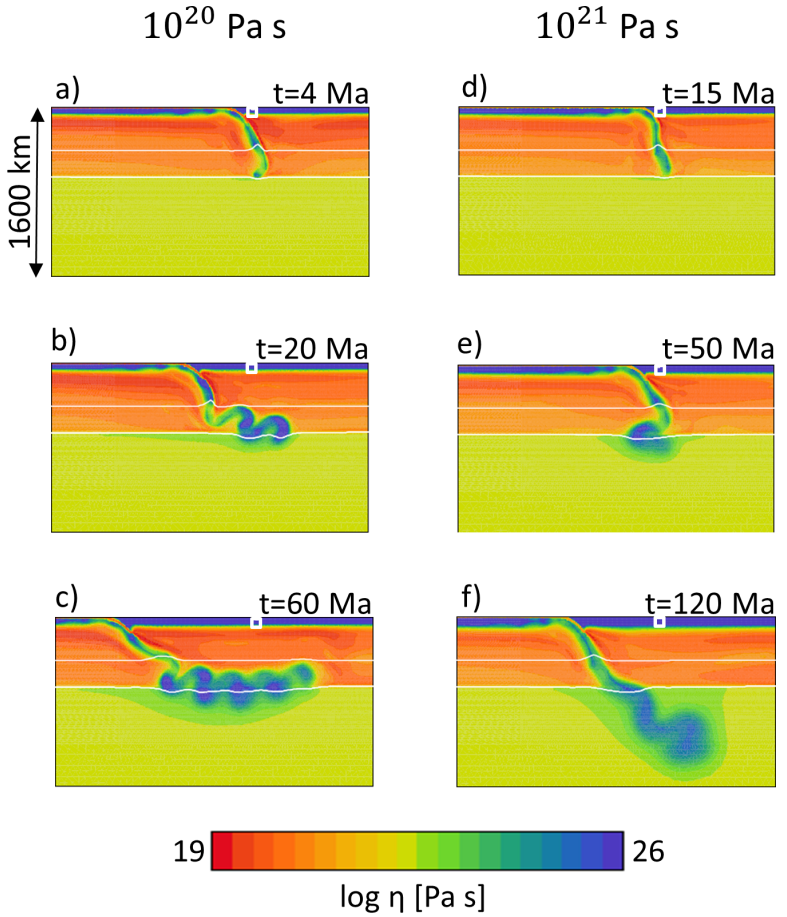

Figure 3.2: Zoomed-in plots showing time evolution of viscosity in the 3000 km wide and 1600 km deep window for models with low viscosity crust of 10^{20} *Pa s (a-c) and for high viscosity crust of* 10^{21} *Pa s (d-f). Both models have intermediate-thick crust. White lines indicate positions of the phase transitions at 410-km and 660-km depths.*

The model with a strong crust (Fig. 3.1d-f) results in much slower rollback (0.5 - 1 cm/year, Fig. 3.3 dashed black line) and penetrative slab. Here higher crustal viscosity causes higher friction near the contact of the subducting and overriding plates and slab rotates towards vertical, displaying significantly higher dip angles (50 - 90 deg, Fig. 3.3 dashed red line). The slab thus buckles largely vertically showing limited rollback [Čížková and Bina, 2013, Goes et al., 2017].
In Fig. 3.4 we compare all models with constant crustal viscosity. We show here a single snapshot of viscosity for each model. This snapshot is taken at the moment when a 2500 km long part of the slab has been subducted. By comparing these snapshots we can conclude that increasing of the crustal thickness has a similar effect as decreasing the crustal viscosity. Models with efficient crustal decoupling (either through higher crustal thickness or lower crustal viscosity) result in stagnation at 660 km depth while models with less efficient decoupling have penetrating slabs. These observations illustrate a trade off between the viscosity of the weak crustal layer and its thickness.

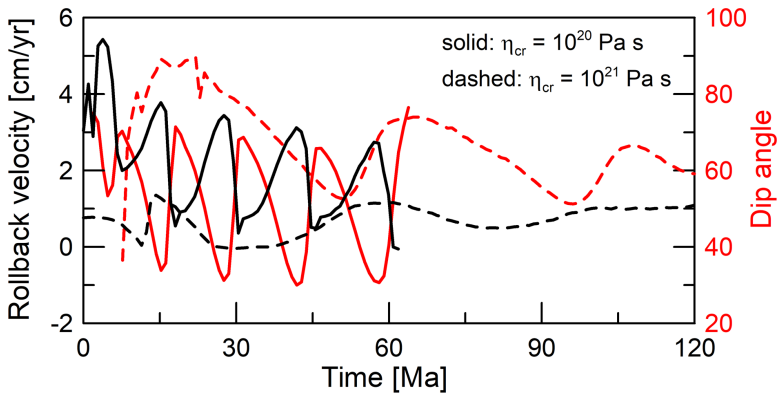

Figure 3.3: Time evolution of rollback velocity (black lines) and slab dip angle in the depth interval 200-300 km (red lines) for two models with intermediate crustal thickness. Solid lines are for the model with weak crust (10^{20} Pa s) and dashed lines for the model with strong crust (10^{21} Pa s).

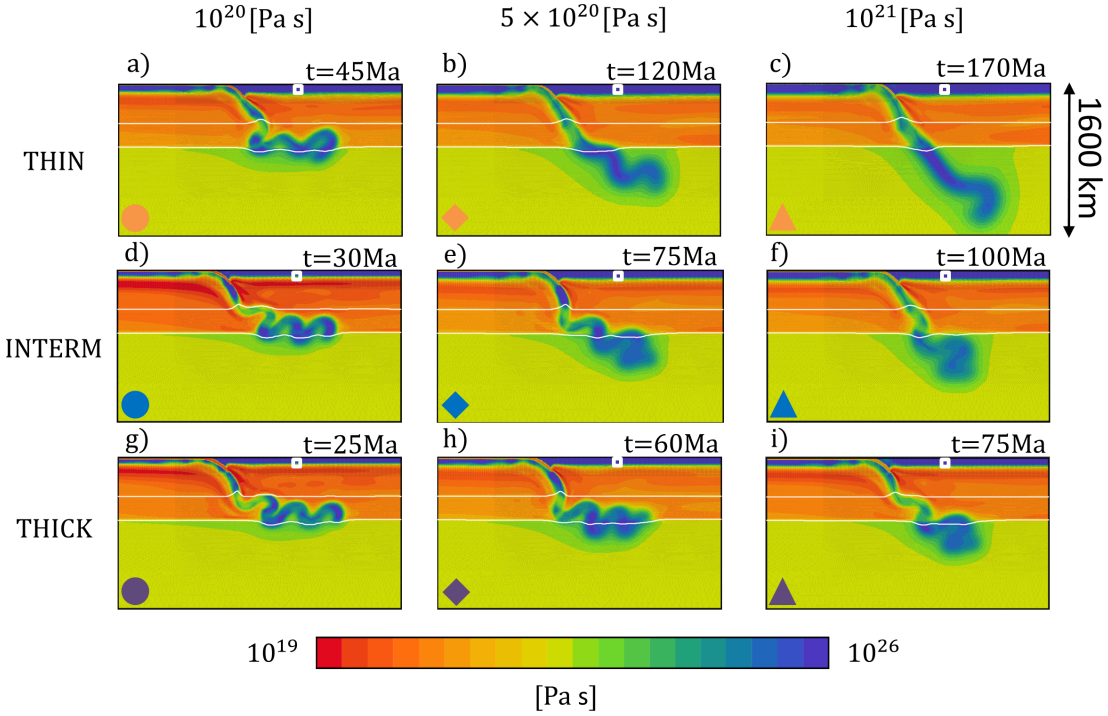

Figure 3.4: Zoomed-in plots showing 3000 km wide and 1600 km deep window for models with three different crustal thickness and viscosity values. Snapshot is taken at the moment when a 2500 km long part of the slab has been subducted. Panels a, b and c show models with thin crust, panels d, e and f represent intermediate crust thickness models and panels g, h and i have show models with thick crust. Left column (panels a, d, g) shows models with the low crustal viscosity of 10^{20} Pa s, middle column (panels b, e, h) is for models with intermediate crustal viscosity of 5×10^{20} Pa s and right column (panels c, f, i) represents models with the strong crust with viscosity 10^{21} Pa s. White lines indicate positions of the phase transitions at 410 and 660 km depth. White squares mark the initial position of the trench. Symbols in the lower-left corner represent each model in Fig. 3.13.

3.4.2 Nonlinear crustal rheology

In our second group of experiments we prescribe a more realistic, composite nonlinear rheology in the crustal layer with a combination of dislocation creep and pseudoplastic deformation. First, we will demonstrate the time evolution of a model with dislocation creep and pseudoplastic parameters based on Ranalli [1995] as implemented in the upper crust by Liao et al. [2017]. We will further denote this model PwlM1 as the reference model case. Fig. 3.5 shows 6 snapshots of the evolution of this reference model. After approximately 5 Ma of subduction, the slab tip reaches the phase boundary at 410 km and is accelerated by the extra negative buoyancy exerted by the exothermic phase transition (cf. black line in Fig. 3.6a). Consequently, the strainrate within the crustal channel increases and that reduces crustal viscosity (see associated local minimum of average crustal viscosity in Fig. 3.6a, red line). Maximum plate velocity during this accelerating phase reaches as high as 130 cm/year, though only for a very short period of 1 Ma. The slab tip promptly approaches the 660 km boundary and simultaneously plate velocity decreases steeply due to the combined effects of the endothermic phase transition and viscous resistance of the stiffer lower mantle. Strainrate in the crustal channel decreases and the average crustal viscosity increases. The slab arrives at the 660 km phase boundary under a steep angle close to the vertical and develops a backward deflection. Stresses exerted by extra buoyancy due to both phase transitions weaken the slab in the transition zone and the first buckle forms at $\sim$12 Ma (see associated local increase of plate velocity on the black line in Fig. 3.6a). Second buckle starts to develop at about 40 Ma while the accumulated slab material is slowly sinking through the 660 km phase boundary into the lower mantle. At about 70-80 Ma another buckle develops which produces another local maximum in the plate velocity curve and corresponding decrease in the crustal viscosity. The slab, which was initially temporarily stagnant around 30-40 Ma changes thereafter into a penetrative mode.

Slab dip evolution in model PwlM1 is shown in Fig. 3.6b (red line) together with the rollback velocity (black line). In the early stages of subduction the low dip-angle is associated with rollback episodes and subhorizontal buckling at the 660-km boundary. In later stages the anticorrelation between shallow slab dip angle and rollback disappears as rollback is no more controlled by slab deformation in the upper mantle and transition zone. It is increasingly affected by the large scale return flow from the lower mantle. At $\sim$120 Ma the flat-lying part of the slab makes its way through the endothermic phase boundary and starts its decsent through the lower mantle. At that time the dip angle is 60 deg and trench rolls back with 2cm/year.

Variations of crustal rheological parameters

Further we will assess the sensitivity of the system to the variations in crustal rheological parameters. First we will vary the pseudoplastic rheology. In case of model PwlM2 with twice lower cohesion and pressure gradient μ (Fig. 3.7ab) the crustal viscosity is lower at the very beginning of the subduction process (cf. green and black lines in Fig. 3.8b, first $\sim$5Ma). It results in higher plate velocity (Fig. 3.8a, green line), than in reference model PwlM1 (cf. Fig. 3.8a,

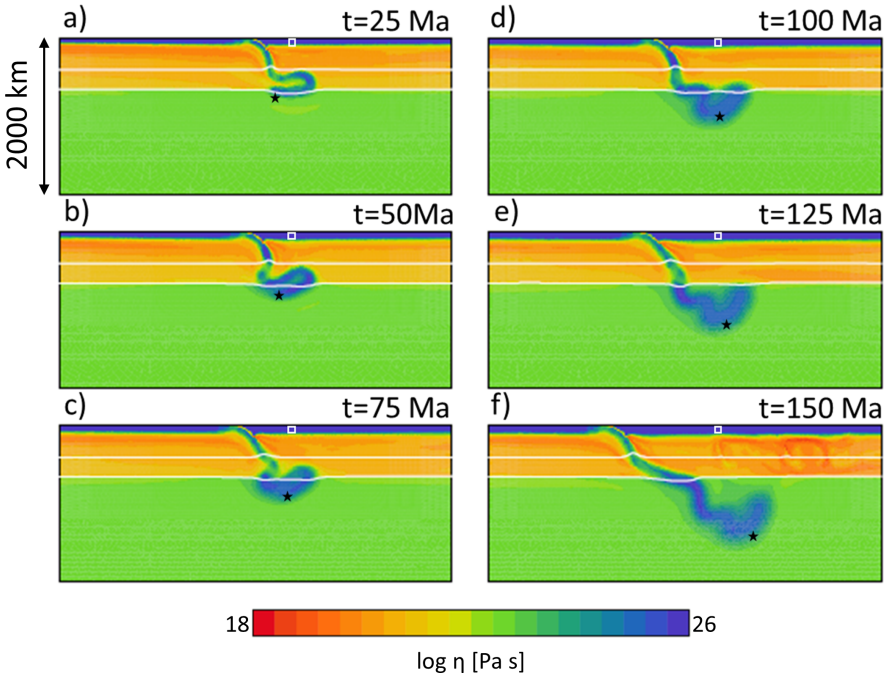

Figure 3.5: Reference model PwlM1 with nonlinear crustal rheology (combination of dislocation creep and pseudoplastic deformation). Thickness of the crust is 10km. Part of the model domain, 2000 km deep and 3000 km wide, is shown. Six snapshots of viscosity are shown with a timestep of 25 Ma. White lines indicate position of the phase transitions at 410 and 660 km depth. White square marks initial position of the trench. Black stars indicate the position of the tracer used for determining the penetration depth.

black line). The first maximum corresponding to the acceleration due to the 410-km exothermic phase transition reaches an extreme value of 250 cm/year and also the secondary and tertiary maxima attained at 53 Ma and 103 Ma during forming of the subsequent buckles are significantly higher than in the reference case (4 cm/year and 2.8 cm/year compared to 2 cm/year in the reference case). The slab rolls back and stagnates at the endothermic phase transition at 660 km depth (Fig. 3.7a,b). On the other hand, higher pseudoplastic stress limit entailed by twice higher cohesion and pressure gradient μ in model PwlM3 (Fig. 3.7cd) causes higher crustal viscosity in shallow parts of the crust.
Due to the higher crustal viscosity it is harder for the plates to decouple. It implies lower plate velocity (Fig. 3.8a) and steeper dip angle as the (slow) slab is rotating towards the vertical in the shallow upper mantle and consequently the rollback is significantly reduced with respect to the reference model PwlM1 and the slab penetrates the lower mantle. We should note here a seemingly counterintuitive behaviour of crustal viscosities in models PwlM1 - PwlM3 with variable crustal strength as illustrated in Fig. 3.8b. One may expect that model PwlM3 should exhibit higher crustal viscosities then the other two models, while the opposite situation is observed e.g.$\sim$30 Ma.

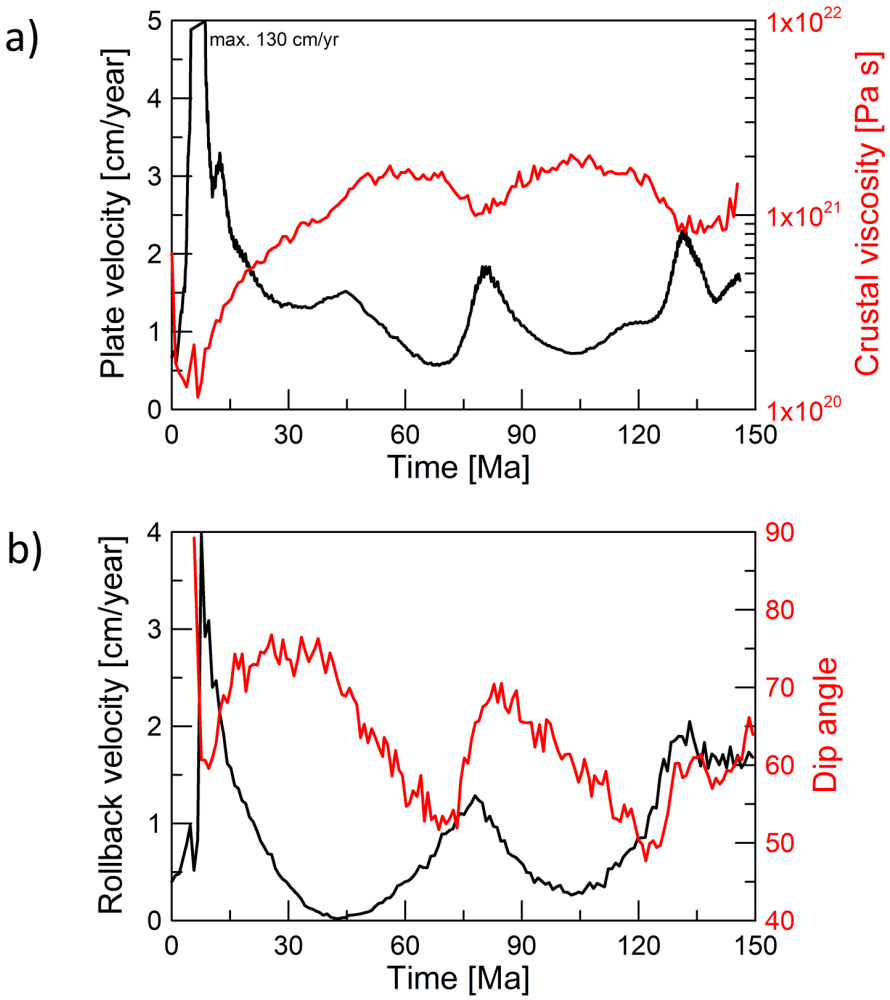

Figure 3.6: Time development of some characteristics of the model PwlM1. a) plate velocity and average crustal viscosity, b) rollback velocity and slab dip angle in the depth interval 200-300 km.

This comparison just illustrates that it is necessary to view these processes as strongly nonlinear and time dependent. The minimum in model PwlM3 at ∼30 Ma corresponds to the moment when the slab crosses the 410-km phase transition and accelerates. This crossing of 410-km occured much later than in models PwlM1 and PwlM2, because the crustal viscosity at the beginning of slab descent in PwlM3 is higher and the slab is consequently slower in the first 30 Ma (cf. Fig. 3.8a). The general trend of the three curves presented in Fig. 3.8b however reflects the fact that viscosity in model PwlM3 is higher than in PwlM1 which is still stronger than PwlM2. We have also investigated the effect of varying the parameters of the dislocation creep. To that end we executed model PwlM4 with pseudoplastic parameters identical to model PwlM3 and with parameters of dislocation creep based on Shelton and Tullis (1981). We did not notice significant difference in character of subducting slab behaviour between these two models PwlM3 and PwlM4. We therefore conclude that pseudoplastic deformation as a dominant deformation mechanism in shallow part of the slab (see Fig. 3.9) has a stronger influence on slab behaviour than the parameters of dislocation creep.

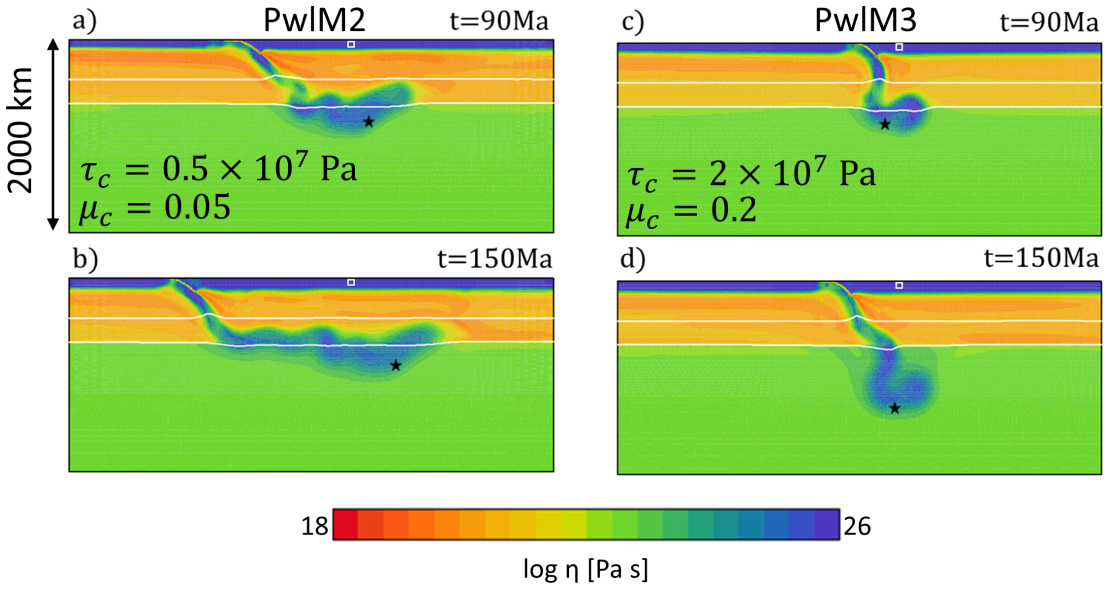

Figure 3.7: Two snapshots of viscosity in model PwlM2 (a,b) and PwlM3 (c,d). Zoom of the model domain 2000 km deep and 3000 km wide. White lines indicate positions of the phase transitions at 410 and 660 km depth. White square marks initial position of the trench. Black stars indicate the position of the lowest tracer used for determining the penetration depth.

Effects of phase transition parameters

Finally we have tested the influence of the strength of the phase transitions on the slab behaviour. Fig. 3.10 shows snapshots taken at 120 Ma for four models with contrasting Clapeyron slopes of both major phase transitions $\gamma_{410}(1\text{MPa/K}, 2\text{MPa/K})$ and $\gamma_{660}(-1.5\text{MPa/K}, -2.5\text{MPa/K})$. Other (rheology) parameters remain the same as in model PwlM1. Fig. 3.10a presents the snapshot of model PwlM1 with reference Clapeyron slopes ($\gamma_{410} = 2\text{MPa/K}$ and $\gamma_{660} = -2.5\text{MPa/K}$). At 120 Ma the slab has rolled back by ~ 800 km and after temporary stagnation at 660 km depth has already started to penetrate the lower mantle. In case of the lower value of the Clapeyron slope of the endothermic phase transition at 660 km depth (Fig. 3.10b), slab mobility is increased with respect to the reference model due to the lower resistance of the endothermic phase transition. This results in faster subduction, faster rollback and deeper penetration of the slab. On the other hand, if we decrease the Clapeyron slope of the exothermic transition at 410 km depth while keeping the higher (reference) Clapeyron slope of the 660 km phase transition (Fig. 3.10c) the subducting plate has slightly faster rollback than in the reference model PwlM1 and less penetration to the lower mantle. It also exhibits less buckling due to reduced stress exerted by the petrological buoyancy anomalies associated with both phase transitions on the slab in the transition zone. Finally if both Clapeyron slopes are reduced (Fig. 3.10d) the slab penetrates the lower mantle while still experiencing fast rollback. Low Clapeyron slope of the 410 km phase transition results in negligible buckling.

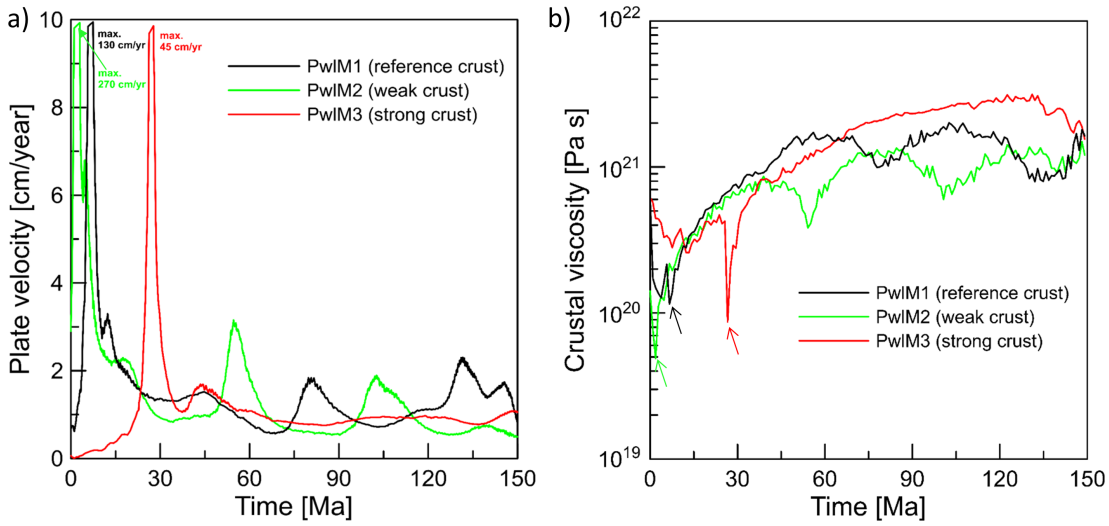

Figure 3.8: Time evolution of the plate velocity in models PwlM1 (black line), PwlM2 (green line) and PwlM3 (red line). Plate velocity is measured in subcrustal lithosphere 2000 km to the right from the left-hand-side ridge. Maximum value of plate velocity in the moment of acceleration by the exothermic phase transition of 410 km depth is 250 cm/year for PwlM2 model, 130 cm/year for the PwlM1 and 45 cm/year for the PwlM3 model. b) Time evolution of the crustal average viscosity in the same models. Color arrows indicate minimum of viscosity corespondig to the maximum of velocity as indicated on Fig. 3.8a.

3.5 Discussion

In numerical modeling of subduction an entrained weak layer is widely used to decouple the subducting and overriding plate [Sandiford and Moresi, 2019] with either constant viscosity [e.g. Běhounková and Čížková, 2008, Chertova et al., 2012, Holt et al., 2015, Agrusta et al., 2017, Briaud et al., 2020] or nonlinear rheology [e.g. Crameri and Tackley, 2014, Garel et al., 2014, Liao et al., 2017, Li et al., 2019]. The magnitude of crustal viscosity was reported to affect plate velocities [Androvičová et al., 2013, Holt et al., 2015] and higher crustal viscosity inhibits rollback [Čížková and Bina, 2013, Arredondo and Billen, 2017, Holt et al., 2015]. Consequently, also the deeper deformation of subducted slabs and slab potential stagnation at the base of the upper mantle is strongly sensitive to the decoupling of the subducting and overriding plates. While low (constant) viscosity of the crust results in fast rollback and stagnation, strong crust results in reduced rollback and easier penetration to the lower mantle [e.g. Čížková and Bina, 2013, Goes et al., 2017, Čížková and Bina, 2019]. Despite that, numerical modeling studies seldom pay attention to an explicit discussion of the effects of weak crustal layer parameterisations. Sandiford and Moresi [2019] have recently shown that the lubrication effect of the weak crustal layer is further affected by its thickness which evolves with time in the models with constant viscosity crust. They demonstrated that transient thinning of the crust may hamper lubrication if the temporarily thinned layer is not properly resolved. Here we conducted an analysis of the combined effects of the crustal thickness and crustal viscosity magnitude and mainly of its nonlinear rheological description and we investigated the effects on slab velocity, rollback and stagnation in the transition zone.

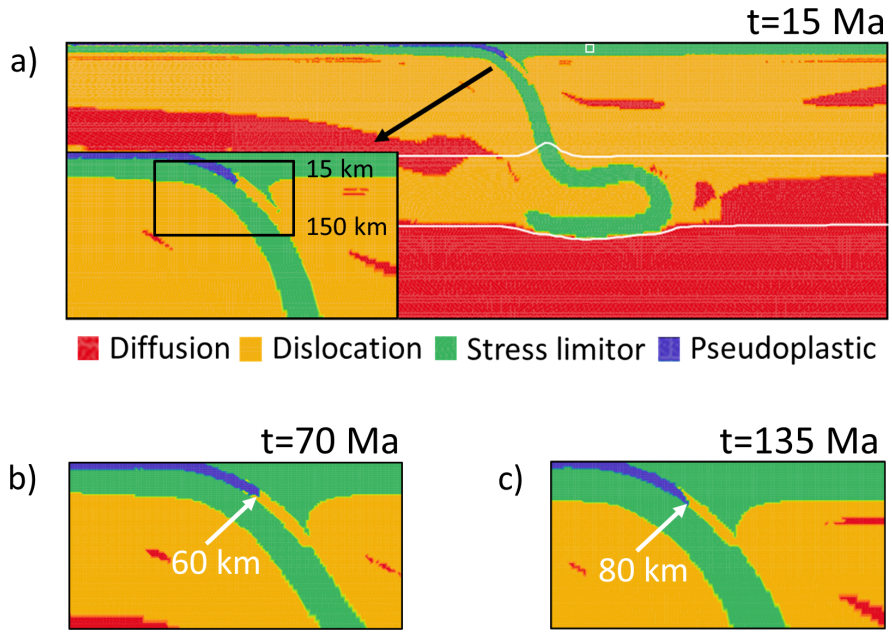

Figure 3.9: Dominant deformation mechanism in model PwlM1, time t=15 Ma. Blue color indicates pseudoplastic deformation, green color stress limiter, yellow dislocation creep and red is for diffusion creep. We show part of the model domain, 1000 km deep and 3000 km wide. White lines indicate positions of the phase transitions at 410 and 660 km depth. The white square marks the initial position of the trench. Closeup in the lower left corner shows the detail of the contact of the plates 300 km deep and 600 km wide. Black rectangle marks the depth range used for calculations of the average crustal viscosity. b) Detail of the plates contact at 70 Ma. White arrow marks the transition between pseudoplastic deformation dominated and dislocation creep dominated areas in the crust. Horizontal velocity of the plate is 0.6 cm/year and mean strainrate in the crust is $1.9 \times 10^{-14} s^{-1}$. *c) The same as b), but for 135 Ma. Horizontal velocity of the plate is 1.95 cm/year and mean strainrate in the crust is* $5.8 \times 10^{-14} s^{-1}$

3.5.1 Effects of crustal resistance to slab penetration

Models with constant viscosity crust

Models with constant crustal viscosity show that the lubricating effect of the weak crust is dependent both on crustal thickness and magnitude of its viscosity and that increasing crustal thickness has the same effect as decreasing its viscosity. This can be quantified by a frictional resistance parameter R that we introduce as the ratio of the viscosity over the effective thickness of the weak crustal layer $R = \frac{\eta_{cr}}{d_{cr}^{eff}}$. Thickness of the weak decoupling crustal layer varies between 6 km and 18 km over the time span of the model calculation in the models with thin crust. The average values of d_{cr}^{eff} used for resistance calculations are 13 - 14 km for the three models with $\eta_{cr} = 10^{20} - 10^{21}$ Pa s. For intermediate crustal thickness models the average d_{cr}^{eff} is 16 - 19 km and for thick crust models it is 23 - 26 km. The resistance characterises the efficiency of the decoupling - low resistance (weak and/or thick decoupling layer) means well decoupled plates white high resistance (strong and/or thin decoupling layer) is in models with strong coupling of the plates. In Fig. 3.11 we plot the resistance against the

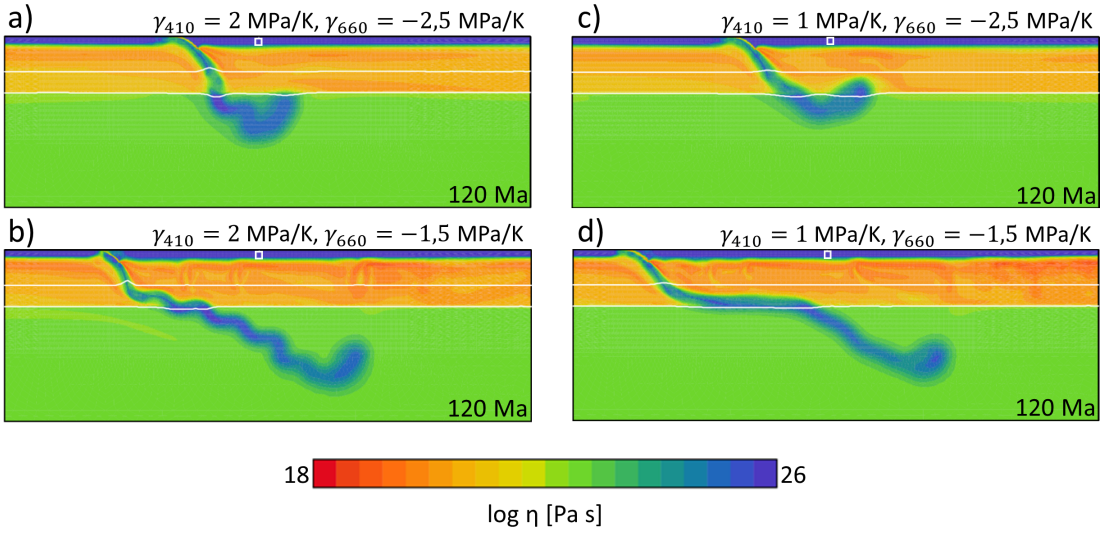

Figure 3.10: One snapshot at 120 Ma of viscosity in four models with varying Clapeyron slopes of 410 km and 660 km phase transitions. Reference nonlinear crustal rheology is used. Part of the model domain 2000 km deep and 6000 km wide is shown. White lines indicate positions of the phase transitions at 410 and 660 km depth. White square marks initial position of the trench.

penetration depth of the slab after 150 Ma in order to quantify the penetrative vs. stagnant slab behavior. Each model is represented by one symbol - yellow symbols are for thin crust, blue for intermediate and violet symbols are for thick crust, circles are for models with weak crust, diamonds for intermediate crustal viscosity and triangles for strong crust. The symbols representing stagnant slabs correspond to pentration depths in the shallow lower mantle close to the 660 km boundary, while penetrating slabs will be found deeper in the lower mantle. The transition between stagnant and penetrative slabs is characterised by a resistance value $R_{crit} \approx 2 - 3 \times 10^{16}$ Pa s m^{-1}. By introducing the resistance parameter we want to emphasize that the decoupling efficiency of the weak layer is not controlled by the layer viscosity alone, but rather by the combination of viscosity and thickness. We should however point out that the threshold resistance R_{crit} that separates longer-term stagnant models from penetrative ones reported above is not unique.

As the slab penetration/stagnation is influenced by many other model characteristics (apart from the subducting-overriding plates decoupling) the critical resistance may be different for different model parameters such as viscosity jump at 660-km or Clapeyron slope of the endothermic phase transition. For example for models with higher stress limit of 0.5 GPa the character of the slab behavior is similar, but the transition between stagnant and penetrative models occurs at higher value of $R \approx 7 \times 10^{16}$ Pa s m^{-1}.

Models with nonlinear crust

Models with nonlinear crustal rheology show more complicated interaction with the 660-km phase and viscous boundary. The viscosity of the weak decoupling crustal layer is now responding to the slab dynamics and a feedback between the

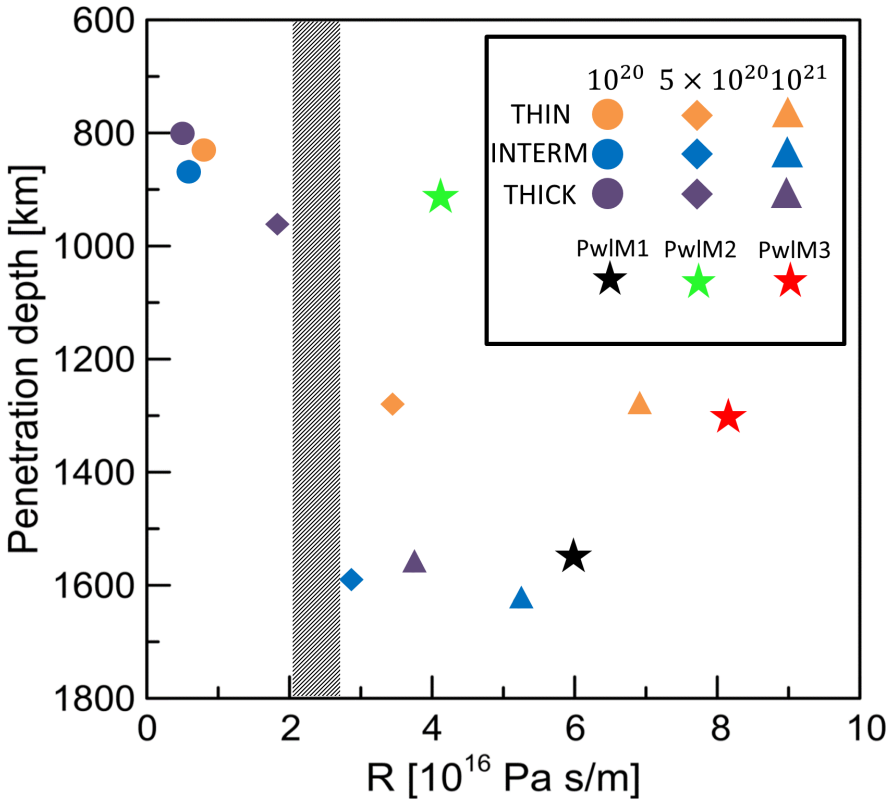

Figure 3.11: Penetration depth at 150 Ma as a function of crustal resistance R. R is defined as the ratio between crustal viscosity and its average thickness. Each symbol represents one of the models with constant viscosity crust shown in Fig. 3.4 (circles, diamonds and triangles) or models with nonlinear crustal rheology (asterisks).

slab velocity and crustal viscosity is observed. Crustal viscosity is anti-correlated with subducting plate velocity - crustal viscosity decreases as the strain-rate increases during slab acceleration, while it increases as the slab slows down and strain-rate is reduced. Both subducting plate velocity and crustal viscosity thus simultaneously reflect the changes in subduction dynamics as slab interacts with the phase transitions and forms buckles in the transition zone.

Slab rollback is clearly correlated with shallow slab dip angle - low dip angle facilitates rollback (possibly accompanied by subhorizontal buckling) and slab stagnation, while steeply dipping slabs are associated with vertical buckling, show limited rollback and penetrate to the lower mantle. Slab dip angle has been shown to evolve with time and reflect kinematics of the subducting and overriding plates, mantle viscosity and petrological buoyancy of the phase transitions [Cerpa et al., 2014, Yang et al., 2018], but also the crustal viscosity [Čížková and Bina, 2013]. Mostly as a result of the forementioned feedback mechanisms average crustal viscosity in our models PwlM1-PwlM3 with nonlinear crustal viscosity varies with time. For the rheological parameters that we used, its variations lie between 5×10^{19} Pa s and 2×10^{21} Pa s. At the beginning, during slab acceleration, the average viscosity of crust in the models PwlM1 and PwlM2 with relatively weak plastic component of crustal rheology is low, so is dip angle and therefore these slabs develop rollback and (temporary) stagnation at 660 km boundary. As the

slabs decelerate while interacting with the 660-km boundary, the higher viscosity favours less rollback and strenghtens tendency to penetration. In the model with strong plastic parameters the viscosity is relatively high even in the early stages of subduction and the slab penetrates the lower mantle without a significant stagnation period.

In order to compare the nonlinear crust models with previously discussed models with constant viscosity crust (par. 5.1.1), we tried to evaluate crustal resistance also for models PwlM1-PwlM3. Though it may not necessarily be straightforward that the style of slab deformation should be controlled by the average viscosity within the subduction channel, we may still try and use this average $\eta_{av}(t)$ together with $d_{cr}^{eff}(t)$ to evaluate the resistance $R(t) = \eta_{av}(t)/d_{cr}^{eff}(t)$ as a function of time. Its average values (averaged over 150 Ma subduction evolution) we then plotted in Fig. 3.11 against the corresponding penetration depths (black, green and red asterisks). Similarly to constant crustal viscosity models, we observe the division between the long-term stagnant model PwlM2 with weak crust that appears in the upper-left part of the graph while the penetrative models PwlM1, PwlM3 with stronger crust are located in the lower-right part of the graph. The division between the stagnant and penetrative models is however shifted towards higher resistance. Apparently the time varying nature of crustal resistance in nonlinear models makes inferences about slab deformation more complicated and using one (average) resistance to characterise the models is problematic.

Stagnation/penetration behavior is therefore further illustrated in Fig. 3.12 where the penetration depth and sinking velocity are plotted as a function of time. Stagnant slabs are characterised by a penetration depth that remains less than $\sim$800 km in a long term run. An example of a long term stagnant slab is in the model with constant crustal viscosity of 10^{20} Pa s (cf. Fig. 3.4a). Its penetration depth is in Fig. 3.12a demonstrated by the blue line and its sinking velocity (Fig. 3.12b) remains close to zero. For a penetrative slab (e.g. the model with constant crustal viscosity of 10^{21} Pa s presented in Fig. 3.4c) on the other hand the penetration depth curve does not have a flat part (see Fig. 3.12a, yellow line) as the slab is descending to the lower mantle without significant hindrance. Its sinking speed (Fig. 3.12b yellow line) in later stages of slab descent reaches 1cm/year, which is in agreement with slab sinking speed inferred by van der Meer et al. [2010]. The reference model PwlM1 with nonlinear crustal rheology produces the penetration curve somewhere in between (black line in Fig. 3.12a). It exhibits a flat stagnant part up to approximately 30 Ma and then the penetration depth starts to increase steadily demonstrating the basic characteristic behaviour of the reference model with nonlinear crustal rheology.

3.5.2 Effects of phase transitions in combination with a weak decoupling layer

As discussed above (cf. Fig. 3.10), the strength of both phase transitions affects slab behavior in the transition zone. In order to isolate the effects of the phase transitions from the effects of nonlinear rheology of the decoupling layer, we investigated five additional models. Three of them are with constant viscosity of

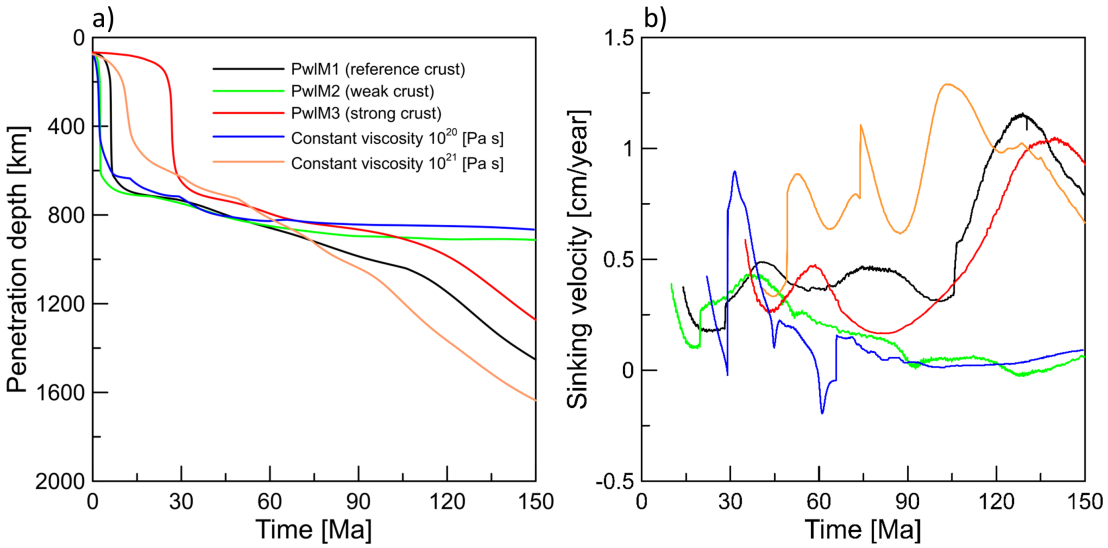

Figure 3.12: Panel a): Slab penetration depth monitored by the position of the deepest tracer located in the slab. Panel b): Sinking velocity computed from the position of the deepest tracer located in the slab. The color legend is the same as in panel a).

crust ($10^{20}, 5 \times 10^{20}$ and 10^{21} Pa s) and without phase transitions. The other two have nonlinear crustal rheology with the same parameters as model PwlM1, but now without phase transitions (PwlM1_0PT) and also the model that has only one phase transition an endothermic one at 660-km depth (PwlM1_660). Fig. 3.13 shows plate velocities in these models compared with the model PwlM1. Let us start with the models with constant crustal viscosity (blue, orange and purple lines in Fig. 3.13). At the beginning the slab tip is at the depth of 200 km and it starts to subduct with plate velocity ∼1–2 cm/year. As the slab subducts the increasing negative buoyancy anomaly results in increasing plate velocity. In case of the stiff crust ($\eta_{cr} = 10^{21}$ Pa s (purple)) the maximum plate velocity of 4 cm/year is attained at 25 Ma. Weaker crust (blue and orange lines) results in more efficient lubrication and therefore the maxima of plate velocity are reached earlier and the maximum is higher (25 cm/year at 5 Ma in case of the weakest crust with $\eta_{cr} = 10^{20}$ Pa s).

At the moment when the slab tip approaches the stiffer lower mantle, it slows down and the plate velocity decreases. Now let us look at the effects of nonlinear crustal viscosity, also in the model without phase transitions (PwlM1_0PT green line in Fig. 3.13). At the beginning the plate is slower than in the model with constant viscosity 10^{20} Pa s (cf. blue and green lines), because the nonlinear rheology yields higher viscosity at low deformation rates. However, as the slab tip subducts deeper and developes more negative buyoancy, the slab accelerates and ensuing higher velocity and deformation rate results in crustal viscosity reduction. Crustal viscosity then decreases below 10^{20} Pa s and therefore the maximum velocity of 33 cm/year attained in the model PwlM1_0PT is higher than in case with $\eta_{cr} = 10^{20}$ Pa s. Model PwlM1_660 which includes only the endothermic phase transition at 660 km shows a very similar behavior as the model without phase transitions. It is slightly slower from the very beginning, because the

660-km phase boundary exerts a small resistive force to the downwelling mantle material pushed to the lower mantle in front of the downgoing cold slab tip before the tip itself reaches the phase transition. A small difference between the curves with and without the endothermic phase transitions suggests that the primary role is played by the viscous resistance of a strong lower mantle and that the phase transition has only a secondary effect here. On the contrary, adding the exothermic phase transition at 410-km depth (model PwlM1 (black line)) results in a very strong acceleration thanks to the feedback between the slab velocity and crustal viscosity - maximum plate velocity is now 130 cm/year.

Since our mantle material composition is limited to olivin, we use relatively mild values of the Clapeyron slopes of the major phase transitions, as the overall buoyancy effect of the phase transitions in the pyrolitic mantle should be significantly reduced with respect to pure olivine composition [Arredondo and Billen, 2016]. Even then we obtain a very strong slab acceleration when its tip first encounters the 410-km phase transition. Extremely high plate velocity maximum (more than 1 m/yr in case of a reference plasticity parameterisation) is only attained in a very short time interval. Moreover we have to keep in mind that here we probably encounter one of the limitations of a 2D model setup. The slab tip crosses the 410-km boundary at the same moment along its whole (infinite) length. In real world this effect will always be smaller as a 3D plate will be passing through the phase boundary gradually, so the acceleration will be significantly smaller.

3.5.3 Deformation partitioning in the weak layer between pseudo-plastic and dislocation creep

As discussed in section 3.4.2, slab behavior is strongly sensitive to the variations of parameters of pseudoplastic deformation that dominates at shallow depths (Fig. 3.9a). Our pseudoplastic deformation approximates brittle failure which should dominate at low temperature and high strainrate. As both temperaure and strainrate within crustal channel vary with time during slab evolution one may expect that the transition between brittle (pseudoplastic) and ductile (dislocation creep) deformation will also develop in time. The average transition depth between the Byerlee type pseudoplastic deformation and viscous dislocation creep in our reference model PwlM1 is ~ 60 km during the subduction evolution. During slab acceleration periods, when crustal viscosity decreases and plate velocity and strainrate increase, the pseudoplastic deformation dominates up to larger depths of ~ 80 km. This is illustrated in Fig. 3.9bc, where the transition depth between pseudoplastic deformation and dislocation creep is marked for two snapshots - at 70 Ma when the plate velocity is 0.6 cm/year (cf. Fig. 8a, black line) and at 135 Ma when plate velocity reaches local maximum of 1.95 cm/year. The shift of the transition depth from 60 km to 80 km during slab acceleration at 135 Ma illustrates its strainrate dependence. One should also note that at 135 Ma (Fig. 3.9c) the boundary between brittle deformation dominated and ductile deformation dominated areas is tilted, with dislocation creep dominating in the right half of the crustal chanel. This is probably due to the increased temperature near the boundary between the subducting and overriding plates. During slab acceleration the contact zone of the plates is heated by viscous dissipation and

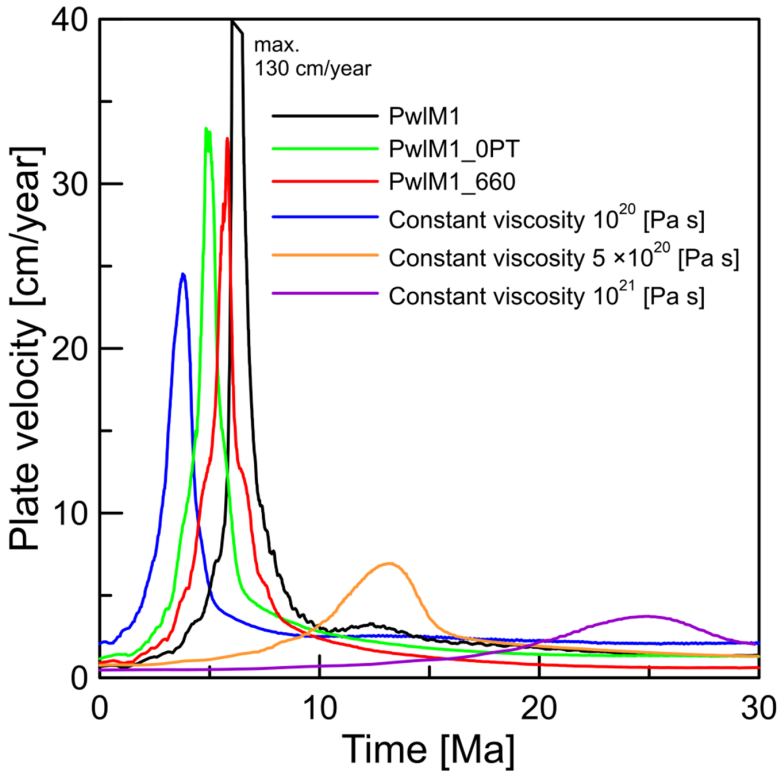

Figure 3.13: Time development of the plate velocity in models with reference nonlinear crustal rheology PwlM1. Crust thickness is 10 km, stress limit of 2×10^8 *Pa. Black line shows model with both 410 km and 660 km phase transition, green line is for model without phase transitions and red line for model with only 660 km phase transition. For comparison we also show models with constant crustal viscosity of* 10^{20} *Pa s (blue line),* 5×10^{20} *Pa s (yellow line) and* 10^{21} *Pa s (purple line).*

temperature in the right half of the crustal channel is by 50 K warmer than the minimum temperature in the slab center (450 K).

3.5.4 Concluding Remarks

The decoupling between the subducting and overriding plates is one of the factors that have strong influence on the slab interaction with the transition zone. The style of deformation, stagnation or lower mantle penetration, appears to be a treshold phenomenon and a small change of other model parameters, e.g. shifting the viscosity transition between the upper and lower mantle to 1000 km depth [Čížková and Bina, 2019], can change the slab behavior from stagnant to penetrative. From that perspective our analysis of the effects of nonlinear crustal rheology shows the situation to be even more complex, since the feedback between the (time variable) crustal viscosity and slab velocity further complicates the subtle balance of thermal and petrological buoyancy that controls slab penetration. The decoupling effects of the (wet) crustal material that in natural subduction zones occur on very fine spatial scales were investigated in terms of reginal scale models focused on the subduction process at shallow depths [e.g. Gerya and Meilick, 2010]. Our crust parameterisation does not take into account

fine and complex substructure of the crust with a fine sedimental layer at the top underlayed with pillow basaltic lavas, sheeted dike complex and gabro cumulates. Such complex structure is at present beyond the reach of our whole mantle scale models, where resolving crustal structures on kilometer scales remains a challenge. It is therefore difficult to make definitive conclusions about slab stagnation/penetration on the basis of our models. We do however stress the fact that nonlinear crustal rheology strenghtens transient behavior of the subducting slabs and enforces slab penetration after transient period of stagnation. This is probably a more realistic scenario of slab interaction with the transition zone, because in real world observations (mapped by seismic tomography) we do not observe very long term stagnant slabs as are predicted by the models with a low crustal viscosity. In various subduction regions a temporary stagnation is observed (e.g. Japan, Izu-Bonin, Tonga), sometimes followed by penetration [van der Meer et al., 2018]. The lateral extent of flat lying part is however typically limited to 1000-1500 km [Goes et al., 2017] while our weak crust models report subhorizontal buckling and stagnation at 660 km for periods of time longer than 100 Ma resulting in flat-lying slab portions of more than 2000 km.

4. 2D stress rotation in the Tonga subduction region

This chapter was published as Pokorný et al. [2023] in Earth and Planetary Science Letters

4.1 Introduction

The dynamics of oceanic plates subducting into the Earth's mantle are unique for each subduction region and depend on various parameters [e.g. Billen and Hirth, 2007, Faccenda and Zilio, 2017, Nakao et al., 2018, Behr et al., 2022, Cerpa et al., 2022]. Some slabs penetrate almost vertically into the lower mantle while others are rolling back and subhorizontally buckling in the transition zone [e.g. Goes et al., 2017, Pokorný et al., 2021]. The differences in the slab topologies are expressed in different stress and strainrate fields in the vicinity and within the cold slabs and are related to deep seismicity [e.g. Ohuchi et al., 2017, Billen, 2020].

One of the widely studied and yet not at all entirely understood regions is subduction of the Pacific plate at Tonga-Kermadec-Hikurangi zone. The onset of subduction of the Pacific plate under the Australian plate along this boundary still remains enigmatic and subject of debate with a wide time window of 85-30 Myr for the subduction initiation in the Tonga - Kermadec zone [e.g. Hall, 2002, Schellart et al., 2006, van de Lagemaat et al., 2018, Sutherland et al., 2020]. Currently, the convergence velocity along the subduction line varies between 11 cm/yr and 5 cm/yr, while the rollback velocity is decreasing from 15 cm/yr in the north to $\sim$1 cm/yr in the south [Schellart et al., 2008, Schellart and Spakman, 2012].

Seismic tomography resolves a high velocity associated with the subducted slab in the upper mantle and transition zone with a dip angle slightly increasing from the north towards the south [Fukao and Obayashi, 2013]. This region of high seismic velocities is associated with seismicity down to the base of the transition zone with a few events observed as deep as 680 km. Seismic tomography further suggests that the slab is lying flat close to the top of the lower mantle. The details of this slab stagnation are, however, not clear, with indications for slab (temporarily) trapped either above and/or below the 660-km boundary. Fig. 4.1 shows one vertical section of seismic velocity anomalies in northern Tonga, plotted for two tomographic models [Fukao and Obayashi, 2013, Amaru, 2007]. In each snapshot two alternative interpretations of possible slab shape are shaded in green. Note that these interpretations differ among panels (a) and (b), as Amaru [2007] (panel (b)) seems to localise the heel of the stagnant slab above the 660-km boundary, while the model of Fukao and Obayashi [2013] indicates stagnation below this interface.

The spatial distribution of deep earthquakes in the subduction zones is usually taken as a first-order approximation of the slab geometry. Furthermore, analysis

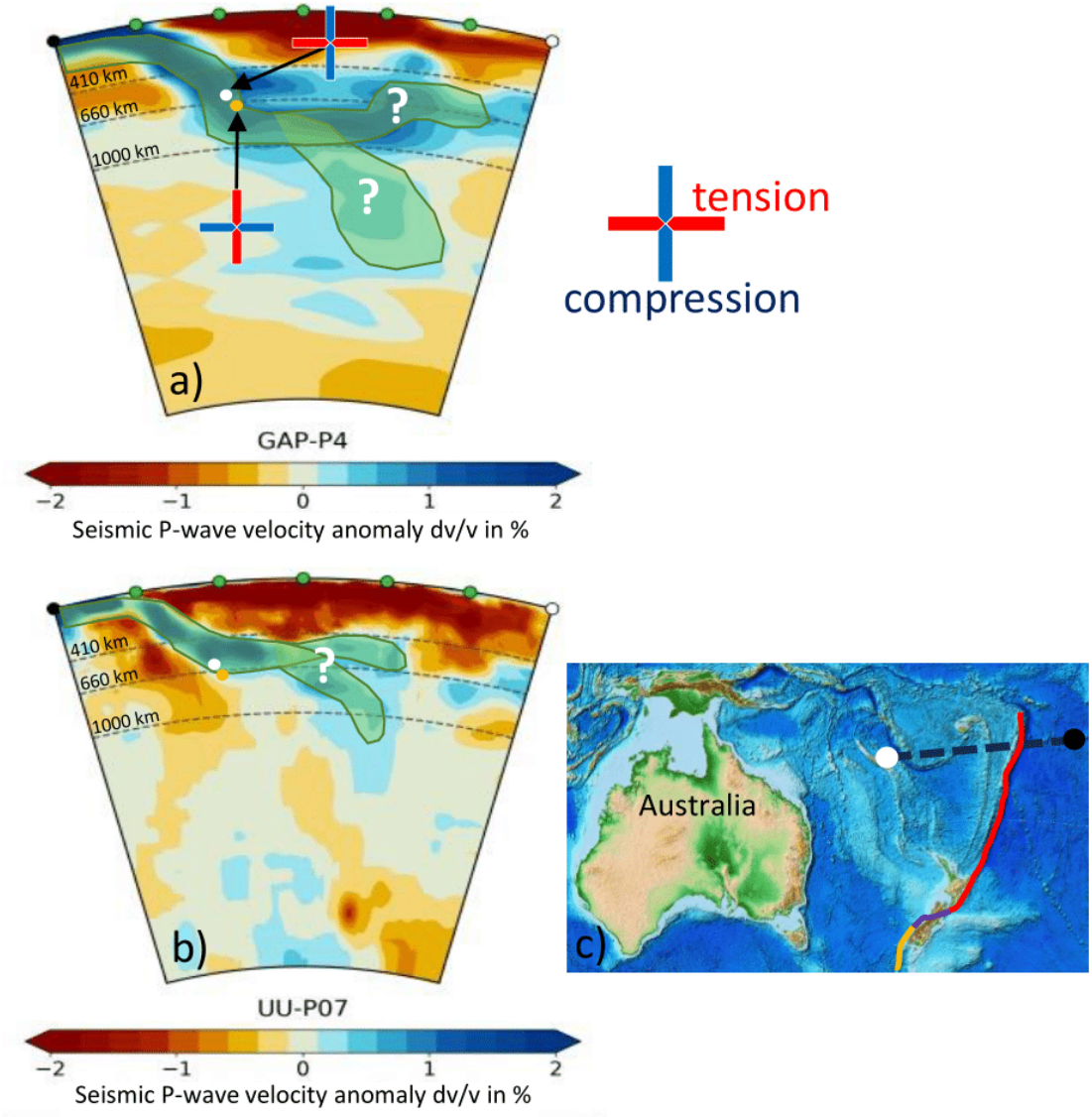

Figure 4.1: Tomographic images obtained using the tool SubMachine [Hosseini et al., 2018, https://www.earth.ox.ac.uk/ smachine/cgi/index.php] in northern Tonga. a) GAP-P4 model [Obayashi et al., 2013, Fukao and Obayashi, 2013]. Green shaded areas suggest possible scenarios of slab deformation. White and yellow dots indicate the seismic events that are characterized by contrasting stress orientations. Dashed lines indicate the depths 410, 660 and 1000 km. b) The same as a), but for model UU-P07 [Amaru, 2007]. c) Topography map [Amante and Eakins, 2009] showing the location of tomographic cross-sections (dashed black line). Coordinates of end points indicated by black and white dot are [160.0° E, 16.0° S] and [168.0° W, 18.0° S]. Red line depicts the Tonga -Kermadec - Hikurangi trench, purple line shows the Alpine transformational fault crossing the south island of New Zealand and yellow line shows the Puysegur trench. Note that we show the sections viewed from the north.

of seismogenic stresses may provide an indication as to the directions of tectonic stress in the subducting slab and thus may help to constrain geodynamic subduction models [Vassiliou et al., 1984, Gurnis and Hager, 1988, Zahradník et al., 2017]. In the case of deep earthquakes close to the base of the transition zone,

one should expect down-dip compressional stresses due to the resistance to slab penetration into the lower mantle. Work by Fukao et al. [2014], however, suggests that the focal mechanisms of deep earthquakes in the northern part of the Tonga-Kermadec subduction zone (specifically in Tonga sections B and C of Fukao and Obayashi [2013]) exhibit a change in local stress regime, from the typical down-dip compression over the depth range 590-620 km to unusual subhorizontal compression at depths greater than 680 km. These events may potentially be located in the slab just below the phase boundary separating the transition zone and lower mantle (for schematic indication of their position see yellow dot in Fig. 4.1a. The shallower events observed at depths $\sim$ 600 km, on the other hand, show usual downdip compression (Fig. 4.1a, white dot).

As summarized in a recent review by Zhan [2020]: "Deep earthquakes exist because of a combination of ongoing deformation that sustains stress and mechanisms of shear instability that release the stress seismically." These two factors can be quite independent. At the elevated pressures and temperatures of deep seismicity, the relevant shear instability is unlikely to be brittle faulting. The most commonly proposed mechanisms of deep seismogenic shear instability include polymorphic transformational faulting in metastable olivine, high-pressure dehydration embrittlement, and thermal runaway of localized shear heating, or perhaps some combination of these mechanisms, all of which yield weak, narrow bands of low-strength nanometric product phases or melt [Green, 2017]. Details of the dominant shear instability mechanism(s) are not yet clear, but the drivers of ongoing deformation sustaining stress are more well understood. These include forces arising from thermal buoyancy, petrological buoyancy (arising from phase changes), and viscous resistance. Such forces acting on the slab give rise to in-plane (stretching or shortening) stresses as well as geometric bending (flexural) stresses. Evidence of stress contributions from bending is also seen in intermediate-depth seismicity [Sandiford et al., 2020, Sippl et al., 2022]. Here we are primarily concerned with exploring the deformation mechanisms responsible for maintaining slab stress fields as illuminated by deep earthquake focal mechanisms in our study region.

We aim to construct a dynamic slab model that agrees closely with several key observations about this subduction zone. Namely: (i) slab geometry in the upper mantle and transition zone should roughly agree with the shape of the tomographically inferred seismically fast anomaly and the positions of earthquake foci [Fukao and Obayashi, 2013]; (ii) the slab should reach the top of the lower mantle since seismicity is observed as deep as 680 km; (iii) the slab should flatten around 660 km depth; (iv) stress orientations within the slab should change from down-dip (nearly vertical) compression at about 600 km to horizontal compression at $\sim$680 km, where the horizontal distance between these two regions is very small.

The Pacific slab in the Tonga-Kermadec region ranks among the oldest and fastest subducting plates on the Earth. Therefore an exceptionally cold plate is probably reaching the transition zone here with potential consequences for slab dynamics. The petrological buoyancy associated with the phase transitions is strong, and the observed stress rotation between the earthquakes above and below the 660-km

phase boundary might be explained by the combination of thermal and petrological buoyancy around this phase change: namely the competing effects of positive petrological buoyancy of the deflected 660-km phase boundary in the slab above the boundary and negative thermal buoyancy of the deeper portion of the subducted slab below the interface. Cold slab is potentially strong, and therefore the bending forces associated with buckling in the transition zone and uppermost lower mantle may also be expected to play a significant role (one should however note, that such exceptionally cold slab may be weakened through grain-size reduction and delayed grain growth after the exothermic phase transition at 410 km depth [Karato et al., 2001, Čížková et al., 2002, Gerya et al., 2021]). We will present here the results of a modelling study that examines the abovementioned effects in terms of 2D dynamic models of free subduction tailored to specific conditions of the Pacific slab. We evaluate the effects of phase transitions, slab rheology, and mantle viscosity stratification on the stress distribution and address the question of whether the conditions of the exceptionally old and cold slab could explain the observed change of stress orientations at the boundary between the transition zone and lower mantle.

4.2 Methods

We employ the finite-element method implemented in the SEPRAN package [Segal and Praagman, 2005] to solve the governing equations in an extended Boussinesq approximation [EBA, Ita and King, 1994] without internal heating. The Stokes problem is solved using the penalty function method and Picard iterations, the thermal equation is time integrated using the predictor-corrector method with the implicit Euler scheme as the predictor and the Crank-Nicholson 2nd order scheme for the correction step [van den Berg et al., 2015]. FEM mesh resolution is increasing from 3 km at the contact of the plates to 9 km in the transition zone and then gradually towards the boundaries of the model domain.

We represent our model domain with a 2D box 12000 km wide and 2000 km deep. The initial temperature distribution follows a halfspace model within the lithospheric plates, and it is followed by the adiabatic profile with a potential temperature of 1573 K beneath them. The trench is situated in the middle of the upper boundary, ∼6000 km from the left-hand side ridge (Fig. 4.2). Another ridge is positioned in the right-hand side upper corner on the overriding plate. We assume that the overriding plate is 30 Myr old at the trench [Müller et al., 2016]. The effect of subducting Pacific plate age at the trench was tested: we executed three groups of models with ages 90 Myr, 120 Myr, and 150 Myr.

The depth-dependent thermal expansivity decreases from the surface value of $3 \times 10^{-5}\,\mathrm{K}^{-1}$ to $1.2 \times 10^{-5}\,\mathrm{K}^{-1}$ at the bottom of the box at a depth of 2000 km [Katsura et al., 2009]. Thermal diffusivity is constant $10^{-6}\,\mathrm{m}^2\,\mathrm{s}^{-1}$. For the top and bottom boundaries of the box we prescribe a constant temperature of 273 K and 2132 K, respectively. The left and right vertical boundaries are reflective. The onset of subduction is facilitated with a short preliminary kinematic run where a convergence velocity of 4 cm/yr is prescribed between the subducting and overriding plates. Following strategy of van Hunen et al. [2000] in this kinematic prerun

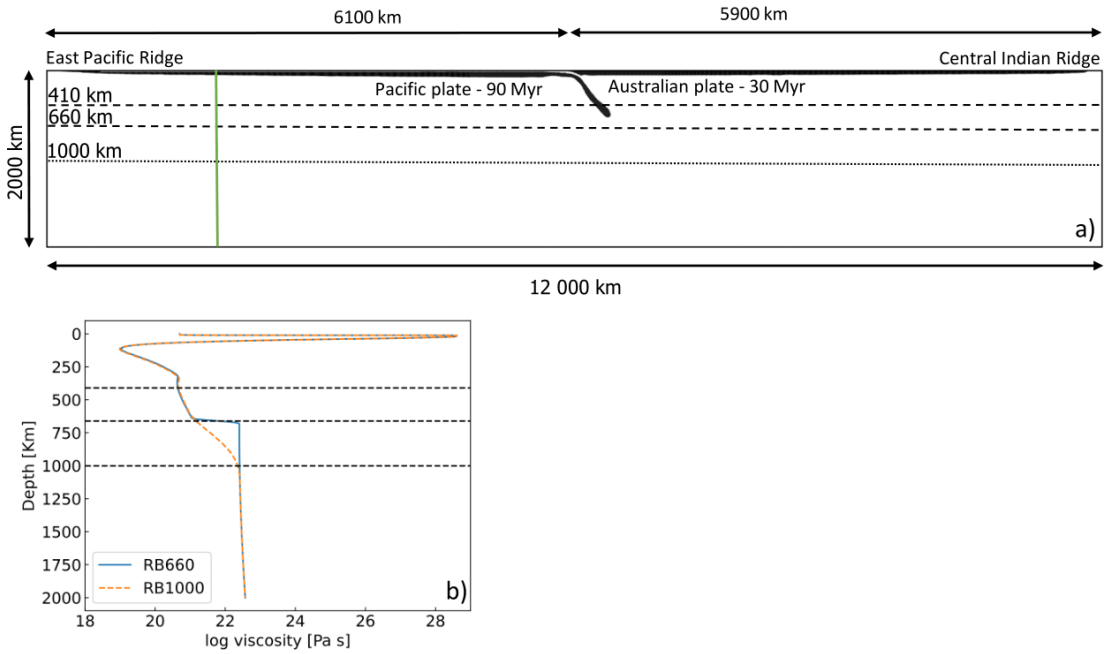

Figure 4.2: a) Model domain 12,000 km wide and 2000 km deep. Dashed lines indicate phase transitions nominally at 410 km and 660 km depths; dotted line is for the rheological boundary at 1000 km used in some models. b) Viscosity as function of depth taken along green profile in panel (a). Blue line shows viscosity profile for models with rheological boundary at 660 km depth. Orange dashed line shows viscosity for models with rheological boundary at 1000 km depth.

we use a reference frame associated with the top surface of the overriding plate, where no-slip is assumed. On all other boundaries a constant horizontal velocity is prescribed, which results in flow field corresponding to the trench rollback situation. This way slab tip is driven to the depth of $\sim$ 400 km while maintaining an almost constant dip-angle (Fig. 4.2a). After 14.25 Myr the kinematic boundary condition is switched off and impermeable free-slip is employed on all boundaries.

In our model the phase transitions are implemented using a phase function [Christensen and Yuen, 1985] with harmonic parameterization [Čížková et al., 2007]. We employ the exothermic phase transition at 410 km depth where forsterite transforms to its polymorph wadsleyite and the endothermic phase transition at 660 km depth where ringwoodite changes to bridgmanite and ferropericlase. Both buoyancy and latent heat effects associated with these transitions are taken into account. The effect of Clapeyron slopes of both phase transitions is tested in a range $\gamma_{410} = 1, 2$ MPa/K and $\gamma_{660} = -1.5, -2.5$ MPa/K.

Our composite rheological model [van den Berg et al., 1993, Čížková et al., 2002] combines diffusion creep, dislocation creep, and a power-law stress limiter as an approximation of Peierls creep [Androvičová et al., 2013]. The respective viscosities of the individual creep mechanisms are as follows:

$$\eta_{diff} = A_{diff}^{-1} \exp\left(\frac{E_{diff} + pV_{diff}}{RT}\right), \tag{4.1}$$

where A_{diff} is pre-exponential parameter of diffusion creep, E_{diff} is activation energy of diffusion creep, p is hydrostatic pressure, V_{diff} is activation volume of diffusion creep, R is the gas constant and T is the absolute temperature. Dislocation creep viscosity is defined as:

$$\eta_{disl} = A_{disl}^{-1/n} \ \dot{\epsilon}_{\|}^{(1-n)/n} \ \exp\left(\frac{E_{disl} + pV_{disl}}{nRT}\right). \tag{4.2}$$

Here A_{disl}, E_{disl} and V_{disl} are pre-exponential parameter, activation energy, and activation volume of dislocation creep, $\dot{\epsilon}_{\|}$ is the second invariant of the strain rate tensor, and the exponent $n = 3.5$ [Kameyama et al., 1999]. Finally the power-law stress limiter viscosity reads:

$$\eta_y = \sigma_y \dot{\epsilon}_y \ ^{-(1/n_y)} \ \dot{\epsilon}_{\|}^{(1/n_y)-1} \tag{4.3}$$

where $\dot{\epsilon}_y$ is a reference strainrate and σ_y is the yield stress. The exponent $n_y = 10$. Values of σ_y were tested in the range of $0.2 - 0.5$ GPa. Viscosities of individual creep mechanisms are combined into an effective viscosity:

$$\eta_{eff} = \left(\frac{1}{\eta_{diff}} + \frac{1}{\eta_{disl}} + \frac{1}{\eta_y}\right)^{-1}, \tag{4.4}$$

Parameters of individual creep mechanisms in the upper mantle and the transition zone are based on olivine experiments [Hirth and Kohlstedt, 2003a] and are given in table 4.1. Rheology of the lower mantle combines diffusion creep with parameters based on [Čížková et al., 2012] and a power-law stress limiter with the same limit as in the upper mantle. The rheological boundary (increase of viscosity) between the transition zone and lower mantle is traditionally assumed to be associated with the seismically inferred bridgmanite-forming phase transition at 660-km depth. Recently however there have been indications that this gradual viscosity increase might be shifted deeper into the lower mantle to a depth of ∼1000 km [Rudolph et al., 2015] and thus explain deeper stagnation of some subducted slabs. Following Čížková and Bina [2019] we therefore test here two groups of models - one with viscosity increase at the top of the lower mantle located at 660-km depth and the other one with deeper layering at 1000 km (Fig. 4.2b).

In order to lower the friction between the subducting and overriding plates a weak layer approach is often used [e.g. Běhounková and Čížková, 2008, Chertova et al., 2012, Sandiford and Moresi, 2019, Behr et al., 2022]. Here we prescribe a weak crustal layer along the top of the subducting plate and in the subduction channel. This layer is 10 km thick and has constant viscosity of 5×10^{20} Pas .

Table 4.1
Model parameters

symbol	Meaning	Value	Units
Upper mantle rheology			
A_{diff}	Pre-exponential parameter of diffusion creep[a]	1×10^{-9}	$Pa^{-1}\ s^{-1}$
A_{disl}	Pre-exponential parameter of dislocation creep[a]	31.5×10^{-18}	$Pa^{-n}\ s^{-1}$
E_{diff}	Activation energy of diffusion creep[a]	3.35×10^{5}	$J\ mol^{-1}$
E_{disl}	Activation energy of dislocation creep[a]	4.8×10^{5}	$J\ mol^{-1}$
V_{diff}	Activation volume of diffusion creep[a]	4.0×10^{-6}	$m^3\ mol^{-1}$
V_{disl}	Activation volume of dislocation creep[a]	11×10^{-6}	$m^3\ mol^{-1}$
η_{diff}	Viscosity of diffusion creep	$-$	$Pa\ s$
η_{disl}	Viscosity of dislocation creep	$-$	$Pa\ s$
η_y	Power-law stress limitor viscosity	$-$	$Pa\ s$
n	dislocation creep exponent	3.5	–
$\dot{\epsilon}_y$	Reference strain rate	1×10^{-15}	s^{-1}
σ_y	Stress limit	$2 - 5 \times 10^{8}$	Pa
p	Hydrostatic pressure	$-$	Pa
n_y	Stress limit exponent	10	–
R	Gas constant	8.314	$J\ K^{-1}\ mol^{-1}$
T	Temperature	$-$	K
$\dot{\epsilon}_{\|}$	Second invariant of strainrate	$-$	s^{-1}
Lower mantle rheology			
A_{diff}	Pre-exponential parameter of diffusion creep	1.3×10^{-16}	$Pa^{-1}\ s^{-1}$
E_{diff}	Activation energy of diffusion creep[b]	2×10^{5}	$J\ mol^{-1}$
V_{diff}	Activation volume of diffusion creep[b]	1.1×10^{-6}	$m^3\ mol^{-1}$
σ_y	Stress limit	$2 - 5 \times 10^{8}$	Pa
Other model parameters			
κ	Thermal diffusivity	10^{-6}	$m^2\ s^{-1}$
g	Gravitational acceleration	9.8	$m^2\ s^{-2}$
ρ_0	Reference density	3416	$kg\ m^{-3}$
c_p	Specific heat	1250	$J\ kg^{-1}\ K^{-1}$
α_0	Surface thermal expansivity	3×10^{-5}	K^{-1}
γ_{410}	Clapeyron slope of 410 km phase transition[c]	$1 - 2 \times 10^{6}$	$Pa\ K^{-1}$
γ_{660}	Clapeyron slope of 660 km phase transition[c]	$(-1.5) - (-2.5) \times 10^{6}$	$Pa\ K^{-1}$
$\delta_{\rho 410}$	Density contrast of 410 km phase transition[d]	273	$kg\ m^{-3}$
$\delta_{\rho 660}$	Density contrast of 660 km phase transition[d]	341	$kg\ m^{-3}$

[a] Parameters of wet olivine based on Hirth and Kohlstedt [2003b]
[b] Čížková et al. [2012].
[c] Bina and Helffrich [1994].
[d] Steinbach and Yuen [1995].

4.3 Results

4.3.1 Stress in simplified slab models

Before discussing the dynamic models where the slab deformation is a complicated function of the combination of parameters, we will first try to illuminate purely the effects of phase transitions on stress distribution in the transition zone. To that end we will use simplified instantaneous flow models, where effects of individual factors can easily be isolated and compared. Models will be started from the same temperature distribution of a developed slab (Fig. 4.3a). For this temperature distribution we will calculate instantaneous velocity and stress fields in several models with different viscosities and the presence or absence of phase transitions.

First, we executed models with uniform viscosity without phase transitions. Fig. 4.3c shows principal deviatoric stresses, with red showing the tensile stresses while blue is for compression. A cold anomaly of a hanging isoviscous slab invokes vertical downward flow, with velocity accelerating from the impermeable free-slip surface until the mid-mantle level and then decelerating towards the bottom boundary. This velocity field is reflected in downward tensile stress in the upper part of the slab followed by downward compression in the deeper portion. Transition from tensile to compressive stress occurs at a depth of $\sim$ 600 - 700 km. If we add petrological buoyancy associated with phase transitions (Fig. 4.3d), the stress pattern in the transition zone changes remarkably. Thanks to upward acting resistive force associated with the deflection of the 660-km phase boundary, the transition zone is associated with vertical compression. Below the 660-km phase boundary the stress sign changes: the buoyancy force associated with the deflected 660-km transition is opposed by the negative buoyancy of the deepest portion of the slab hanging at the depth of $\sim$ 1000 km, which results in vertical tension just below the 660-km boundary. Such a stress distribution seems to be in agreement with the stress orientation as indicated by reported seismogenic stresses [Fukao et al., 2014].

Let us now see whether such stress pattern will be observed also in strong slabs. Fig. 4.3e shows the model with standard composite rheology and with an increase at the transition zone - lower mantle boundary at 660 km, without phase transitions. The slab is now significantly more viscous (Fig. 4.3b) than the ambient mantle. The strong slab acts as a stress guide: the resistance to the tip embedded in the stiff lower mantle is transmitted upward and results in vertical compression in the transition zone, where the slab is also influenced by the weight of its upper-mantle part. Just below the 660 km interface most of the slab body is still under downdip compression. Deeper at $\sim$ 800 km where the slab tip is deflecting towards the horizontal, a typical bending stress distribution is observed with downdip compression in the inner part of the buckle and downdip tension in the outer layer of folded slab.

When phase transitions are switched on (Fig. 4.3f), the petrological buoyancy of both phase transitions strengthen the downdip compression in the vertical slab in the transition zone. Buoyancy associated with the 660-km endothermic transition contributes to tensile stress associated with the bending of the slab in the lower mantle and consequently a small region of downdip tension is observed in the outer layer of bending slab tip just below the 660-km phase boundary. Most of the slab body is however still showing downdip compression.

Furthermore, we have tested the effect of shifting the viscosity increase in the lower mantle deeper to 1000 km. Both models without (Fig. 4.3g) and with phase transitions (Fig. 4.3h) show the maximum downdip compression shifted somewhat deeper to the bottom of the transition zone; otherwise, however, they do not differ significantly from the models with a viscosity increase at 660-km depth.

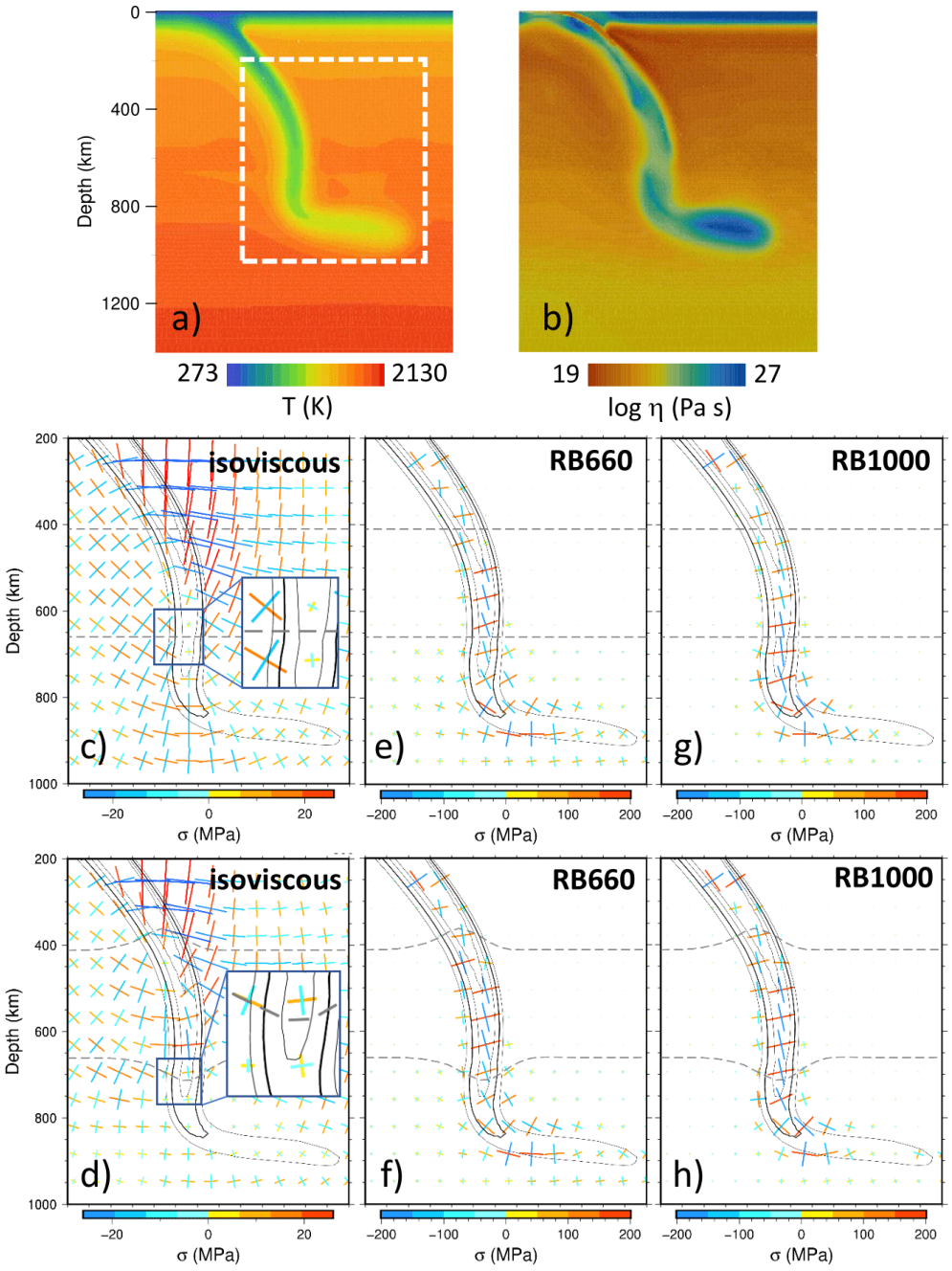

Figure 4.3: Temperature distribution of a developed slab used as an input of instantaneous slab models (only part of the model domain located around slab is shown). Dashed rectangle indicates close-up in which the stress distribution will be shown in plates c)-h). b) Corresponding viscosity in the models with composite rheology. c), d) Stress in isoviscous models without and with phase transitions. Blue is for compression and red represents extension. $\gamma_{410} = 2$ MPa/K, $\gamma_{660} = -2.5$ MPa/K. Overprinted are the isolines of temperature; thick line corresponds to 1200K and spacing between isotherms is 100K. e), f) Stress in composite rheology models without and with phase transitions. Increase of viscosity is at 660-km depth (model RB660 in Fig. 4.2b). g), h) Stress in composite rheology models without and with phase transitions. Increase of viscosity is at 1000-km depth (model RB1000 in Fig. 4.2b)

These results suggest that the phase transition-related buoyancy forces, especially the buoyancy of the deflected 660-km boundary, could indeed result in a transition from downward compression above 660 km to downward tension just below the 660-km phase transition. Such a switch as clearly observed in an isoviscous model is, however, in a strong slab overprinted by stresses transmitted up the slab from resistance of the stiff lower mantle and/or bending related forces. Pure buoyancy effects could thus in realistic strong slabs probably not fully explain the stress switch as indicated by seismic data. We will therefore further investigate whether it might be associated with slab bending and unbending due to phase transitions. Though bending stresses are often associated with mechanical deformation in elastic systems, here both the slab and the mantle are viscous. The dynamical system evolves in response to stresses arising from buoyancy in the slab and viscous flow in the mantle, leading to deformation of the slab, including flexure associated with internal bending stresses [Royden and Husson, 2006]. Deep earthquakes occur within slabs at high pressures ($10 < P < 25$ GPa) and sufficiently low temperatures ($T \leq 1000$ C) that strain energy may accumulate, ultimately to be released via some seismogenic failure mechanism (e.g., transformational faulting, dehydration embrittlement, or thermal runaway). The slabs deform internally but possess sufficiently high viscosity as to support high stresses [Billen, 2020], thus allowing upward transmission of slab-pull force as well as seismogenic deformation at depth [Bilek et al., 2005].

4.3.2 Stress in time-dependent slab models

In a subsequent set of calculations we will focus on the effects of bending and unbending due to phase transitions. The evolution of the slab will first be demonstrated on the model with 90 Myr old slab, yield stress 0.5 MPa, rheological interface at 660-km depth, and strong phase transitions (Clapeyron slopes 2 MPa/K and -2.5 MPa/K at 410 km and 660 km depths), which will be used as a reference model. Fig. 4.4a shows this model at the moment when the slab is affected by the combined resistance of the endothermic phase transition and increased viscosity at 660 km depth. The tip is thus flattening at the bottom of the transition zone. Fig. 4.4e shows the corresponding stress field in the transition zone.

The vertically dipping part of the slab is entering the transition zone, while the flattened tip is moving to the right and the fold is tightening. This is reflected in the stress pattern - stress in the bending part in the middle of the transition zone shows down-dip compression along the inner side of the developing buckle and tension on its left outer side. As for the flattened tip, its lower part is characterised by horizontal compression due to the drag of the more viscous lower mantle, while the upper part is stretching. At about 35 Myr (Fig. 4.4b) the flat slab tip is already at the 660-km phase boundary, and the slab is rolling-back while forming a buckle in the transition zone. The stress pattern in the slab within the transition zone is dominated by down-dip compression. These down-dip compressional stresses arise from the opposed petrological buoyancies of the 410- (negative buoyancy) and 660-km (positive buoyancy) phase boundaries and are transmitted up the cold slab. The tip of the slab which is lying flat at the 660-km boundary is mostly under horizontal compression due to resistance of the viscous lower mantle. Across the lowermost 50 km of the transition zone,

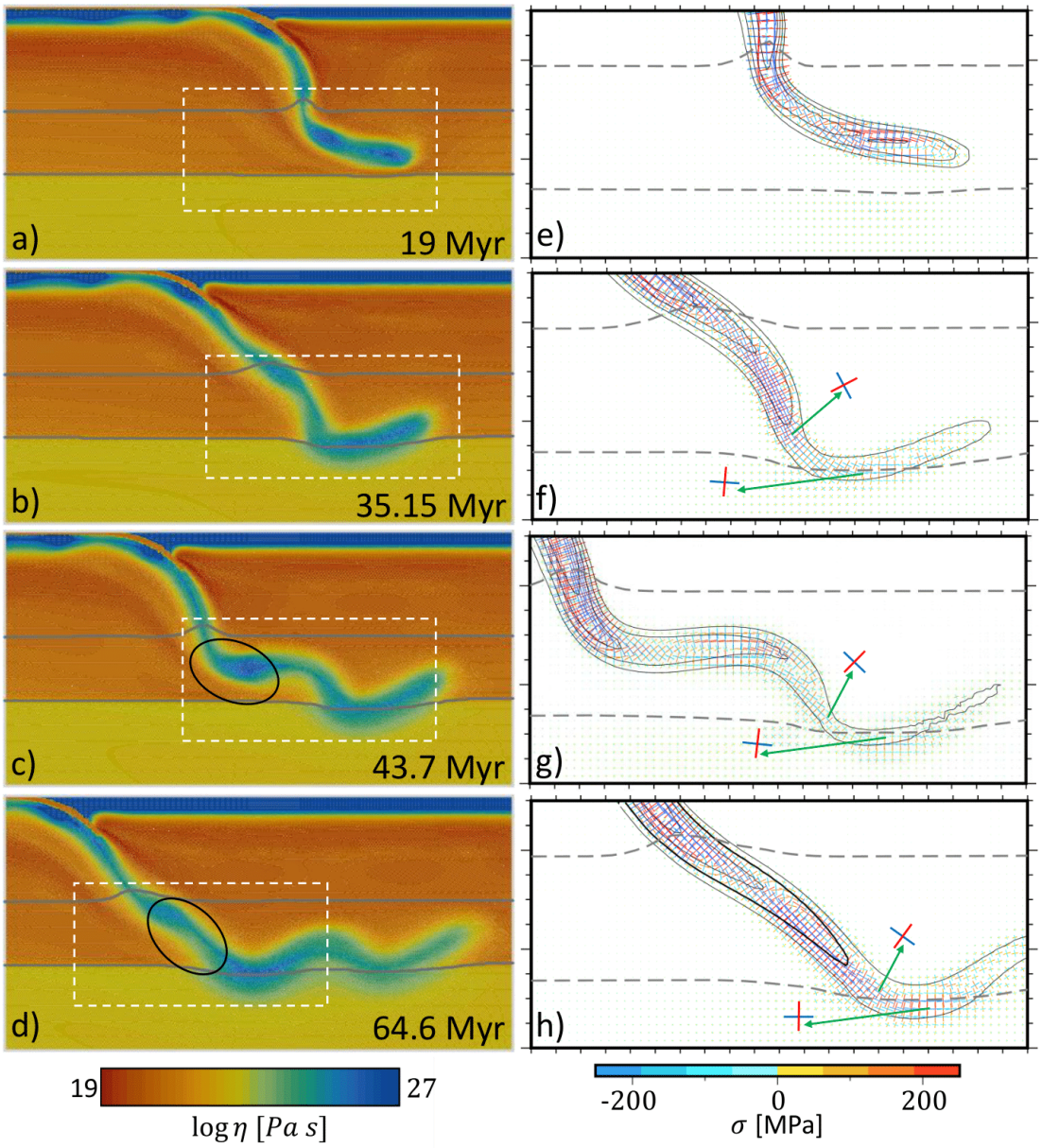

Figure 4.4: a)-d) Snapshots showing time evolution of viscosity in a zoomed window 2000 km wide and 1000 km deep. Gray lines indicate the position of the major phase transitions at 410 km and 660 km depths. White dashed rectangles indicates the area in which the stress is shown. e)-h) Corresponding principal stresses. Blue is for compression and red represents extension. Typical stress orientations above and below the 660-km interface are highlighted by green arrows. Overprinted are the isolines of temperature; thick line corresponds to 1200K and spacing between isotherms is 100K

the stress orientation is gradually changing from downdip compressional (close to vertical) to horizontal compression. Such a stress pattern might to some extent resemble the stress switch observed in seismic data; the horizontally compressed part is, however, rather shallow, and the horizontal distance between the vertically and horizontally compressed parts is rather large compared to observations. At 43.7 Myr (Fig. 4.4c) the sub-horizontal buckle that started 9 Myr ago is tight-

ening (its heel marked by a black ellipse is approaching the 660-km interface), slab dip in the lower transition zone is decreasing, and compressional stresses both above and below the 660-km interface are thus relatively shallowly dipping, too (Fig. 4.4g). The formation of a new buckle starts at around 64 Myr (Fig. 4.4d). Due to a relatively shallow dip angle in the transition zone, the difference between stress orientations above and below the 660-km interface remains rather small. The above snapshots suggest that conditions for the stress rotation are established when the flat part of the slab is supported by the resistance of 660-km boundary, while the vertical slab in the transition zone starts a new buckle while rolling back. However, this model disagrees with the observations (i) in a gradually (over a rather large horizontal distance) occurring transition of stress from vertical to horizontal compression and (ii) in insufficient slab penetration to the lower mantle.

The details of slab deformation in the transition zone depend on the strength of the phase transitions as well as on the rheology. In search of a model exhibiting stress orientations similar to those observed, we have performed a parametric study of slab deformation in the transition zone. We will now discuss its results with respect to stresses above and below the endothermic phase boundary. Fig. 4.5 presents a summary of these models. It illustrates a single snapshot for each model, selected based on their optimal conformity with the moment of the most pronounced stress switch. Each panel depicts the shape of the slab as delineated by a viscosity contour of 10^{23} Pas. For each model slab we tried to identify the nearest two points (one above and one below the 660-km boundary) that would show stress rotation from downdip vertical to downdip horizontal (white and yellow dots) if there is any. For these two points, principal deviatoric stress orientations are shown (red is tension, blue is compression). Models represent subducting slabs of different initial ages at the trench (90 - 150 Myr), two values of yield stress limiting slab strength (blue frames are for 0.2 GPa, orange frames for 0.5 GPa), and two combinations of phase transition Clapeyron slopes ($\gamma_{410} = 1$ MPa/K and $\gamma_{660} = -1.5$ MPa/K marked as 'weak', and $\gamma_{410} = 2$ MPa/K and $\gamma_{660} = -2.5$ MPa/K marked as 'strong'). Finally, we show models with rheological stratification at 660-km depth (solid frames) and at 1000-km depth (dashed frames).

Looking on the left half of Fig. 4.5, which shows models with an increase of viscosity at 660-km depth, one may generally conclude that none of them fits the observed slab shape and stress orientations. The slabs either do not fit the observed slab/stress dip angle that should be close to vertical at the base of transition zone, or the distance between the points displaying the contrasting stresses is too large - or both. Much more promising are the models in the right half of Fig. 4.5, which is for models where the viscosity increase in the lower mantle is decoupled from the endothermic phase transition and shifted to 1000-km depth. Among them, the models with higher yield stress of 0.5 GPa (orange frames) consistently show similar behaviour: the slab that initially flattened above the 660-km phase boundary penetrates to the lower mantle, and the resistance of a viscous interface at 1000-km depth results in temporary stagnation accompanied by a first episode of rollback and initiation of the first buckle in the transition

zone. And it is at this moment when we observe the stress switch on the upper surface of the slab, where the fold of the slab tip lying below the 660-km interface is just tightening, while the shallower part of the slab in the transition zone starts moving to the left.

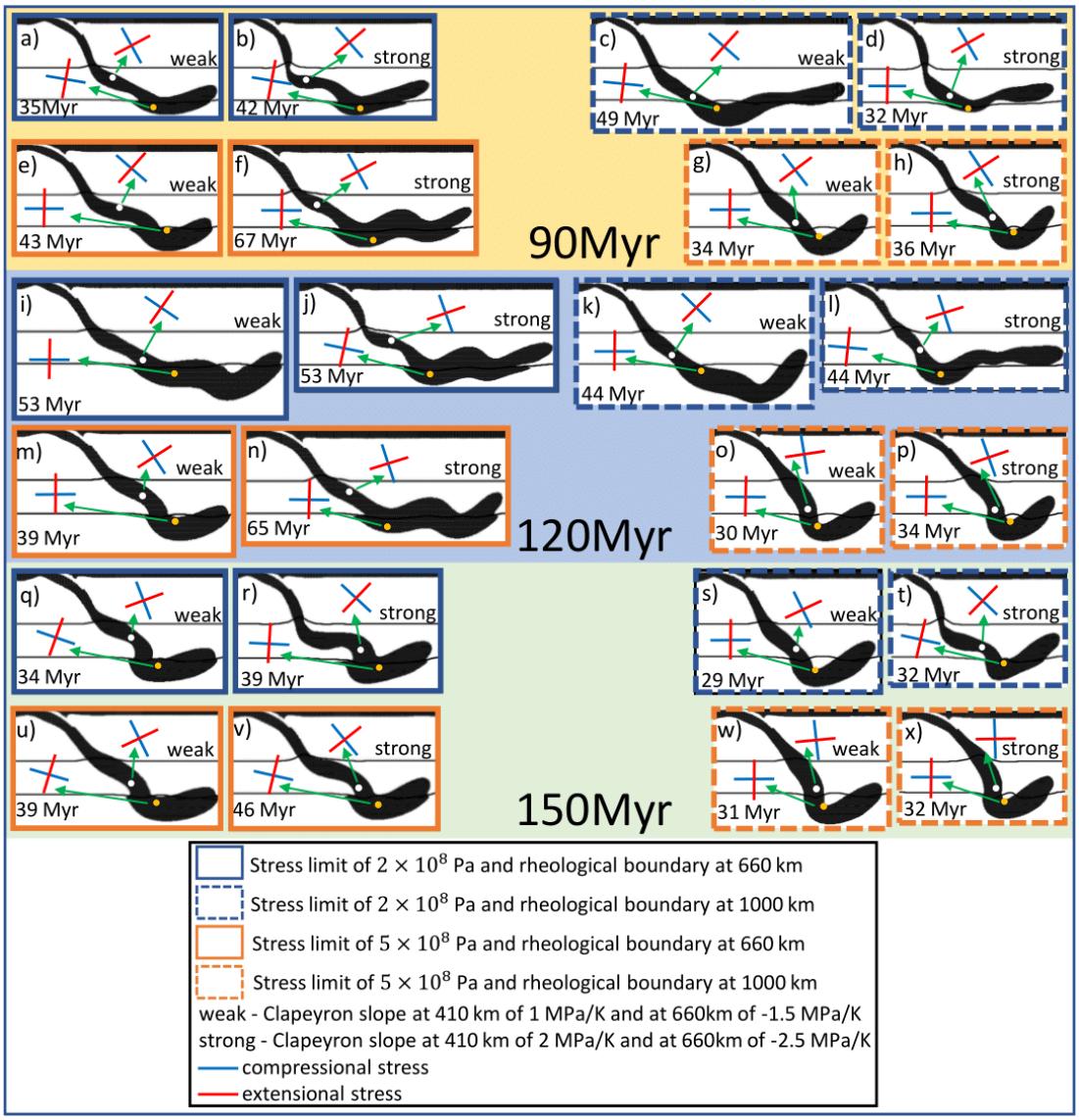

Figure 4.5: Summary of slab topologies for all studied models. Shape of the slab at one time representing each model is delineated by a viscosity contour-line of 10^{23} Pas. Blue rectangles border models with stress limit of 0.2 GPa, orange rectangles models with limit 0.5 GPa. Solid rectangles mark models with increase of viscosity at 660 km while dashed rectangles are for increase at 1000 km. Upper (yellow), middle(blue) and lower (green) thirds of the plot are for subducting plate age of 90 Myr, 120 Myr and 150 Myr respectively. Black lines indicate phase boundaries at 410 km and 660 km depths. White and yellow dots mark the areas above and below 660 km phase transition among which the stress rotation occurs to a certain extent. Stress orientations for these two points are pointed to by green arrows. Blue color represents compression and red is for extension

The oldest and coldest model slab (Fig. 4.5x) fits the observed slab geometry and stress switch best. This is caused by rather subtle differences in the rollback

behavior of the young and old plates. When the younger plate flat tip stagnates at the 660-km boundary (at ∼20 Myr), the viscosity within the slab in the transition zone is weakened thanks to the combined effect of both phase transitions, and a subhorizontal buckle starts to form, the trench starts to roll back, and the slab dip angle in the transition zone decreases. On the other hand, the older cold plate is significantly stronger, experiences less weakening in the transition zone due to the 'squeeze' between the phase transitions, and consequently the rollback episode starts later. Before the rollback episode actually starts, the slab at the base of the transition zone is almost vertical, and its angle with the flat tip below the interface remains lower, thus resulting in the preferred slab geometry of Fig. 4.5x.

4.4 Discussion and conclusions

The spatial variation of thermal and petrological buoyancy forces within the slab, especially along its length, gives rise not only to in-plane stresses but also to bending moments [Bina and Kawakatsu, 2010] which, supplemented by viscous forces from the surrounding mantle, result in slab deformation. Such deformation results in accumulated strain energy within the cold, highly viscous slab which is eventually released via a high-pressure seismogenic failure mechanism (transformational faulting, dehydration embrittlement, or thermal runaway). Our efforts aimed at explaining the unusual stress distribution in northern Tonga at the boundary between the transition zone and lower mantle investigated various mechanisms that affect slab deformation. We have shown that occurrence of the investigated stress rotation from vertical to subhorizontal compression is primarily caused by the bending forces of the cold and strong slab. We have shown that petrological buoyancy associated with an endothermic phase transition might result in stress rotation from vertical to horizontal compression only in very weak slabs. In the models where subducting plate rheology implies strong slabs through temperature, pressure, and stress dependence of viscosity, it is overprinted by stresses transmitted by a strong slab from resistance of the more viscous lower mantle.

Although our models do not explicitly include potential effects of metastable phases and grain-size weakening, these factors may also contribute to geodynamic stresses in the slab. Metastability would increase the degree of down-dip compression above 660 km and enhance the bending of the slab near 660 km. Such enhanced bending might assist in stress rotations. The enhanced positive buoyancy might diminish stress rotation unless all of the metastable material transforms before reaching 660 km, in which case the sudden transition from positive (petrological) to negative (thermal) buoyancy might amplify stress rotation.

It has also been suggested [Liu et al., 2021] that such complex stress patterns might arise from collision of the Tonga slab with a relic detached slab from the Vanuatu trench. Interpreting the nature of this inferred piece of detached slab is quite complicated. There exist some directly competing models (e.g. Okal and Kirby [1998] vs. Richards et al. [2011]). There have also been suggestions that such "fossil slabs contain material that is too warm for earthquake nucleation but may be near the critical stress susceptible to dynamic triggering." [Cai and

Wiens, 2016]. Here we suggest that such collision with a relic slab might not be a necessary condition for the observed stress rotations. Instead, we offer the novel observation that such rotation of principal stress axes may arise purely from the flexural response of the slab to buoyancy and viscous forces near the top of the lower mantle.

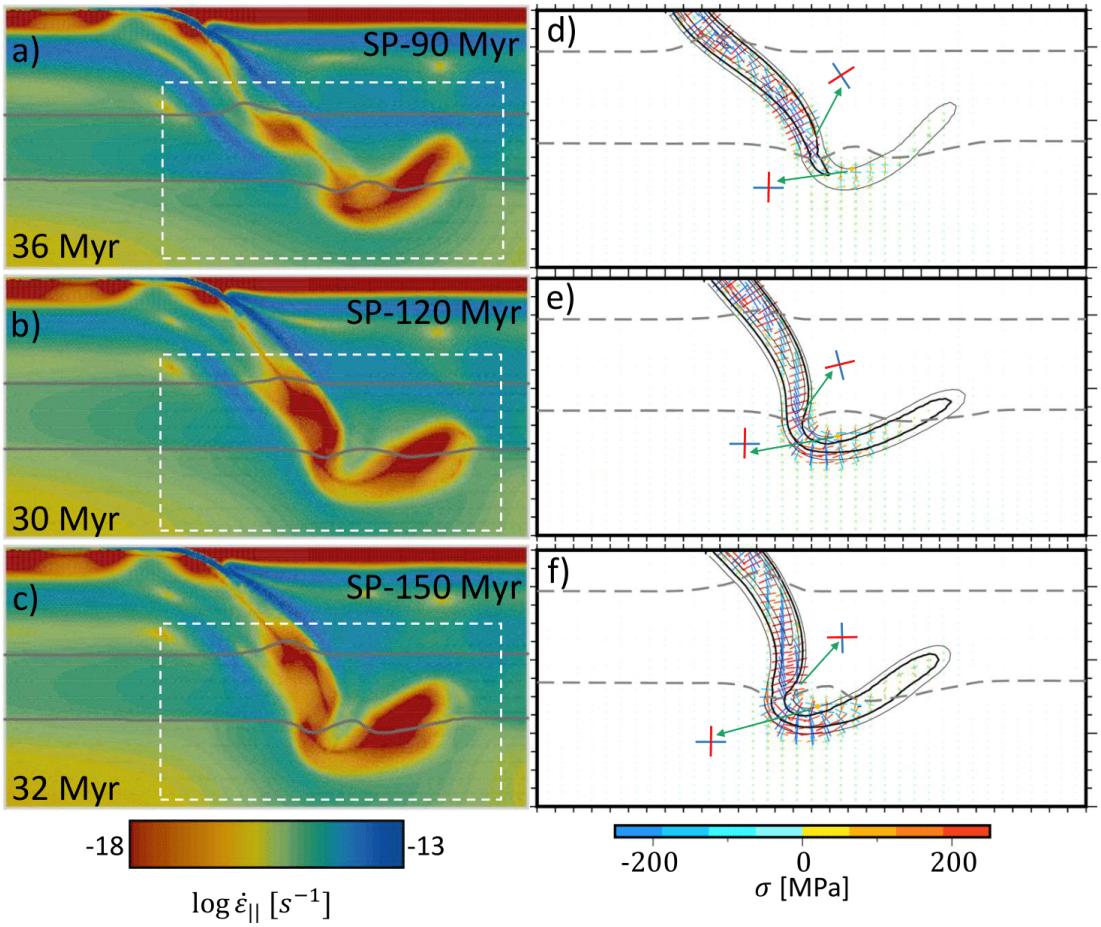

Figure 4.6: a) One snapshot of second invariant of strain-rate for model with youngest subducting plate (SP-90 Myr), yield stress 0.5 GPa, viscosity increase at 1000 km and strong phase transitions. Part of the model domain, 2000 km wide and 1000 km deep is shown. Dashed rectangle indicates the area for which stress is shown in panel d). Grey lines mark the phase transitions at 410 km and 660 km. b) The same but for model with intermediate age subducting plate (SP-120 Myr) and weak phase transitions. c) The same but for model with oldest subducting plate (SP-150 Myr) and strong phase transitions. d)-f) Corresponding principal stresses. Blue is for compression and red represents extension. Typical stress orientations above and below the 660-km interface are highlighted by green arrows. Overprinted are the isolines of temperature; thick line corresponds to 1200K and spacing between isotherms is 100K

We should note here that our 2D model does not aim at full description of this complex and inherently 3D subduction setup. It should rather be considered as an attempt to explore the individual mechanisms that affect stresses at the base of the transition zone and in the shallow lower mantle in Tonga. We do observe that such deep earthquakes with unusual stress orientations apparently are not

present in the southern part of the subduction zone, where tomographic models are dominated by the signal of recumbent or "stagnant" slab material between $\sim$ 660 km and $\sim$ 1000 km depth (and possibly below). Earthquakes exhibiting this interesting stress rotation are only reported in the northern part of the arc, where the tomography also shows recumbent slab material at or just above $\sim$ 660 km depth. One explanation for this apparent superposition of stagnant slabs at different depths is offered by the "origami illustration" of Fukao and Obayashi [2013], in which a lateral bend of the Tonga slab about a slab tear allows for regional "doubling" of the slab. Fukao and Obayashi [2013] further suggested that subhorizontal compressional stresses in the shallower northern slab might imply viscous resistance by the mantle of any horizontal advance of the stagnant slab. Here we further relate such stresses to bending within the stagnating slab.

The present study does not intend to establish a correlation between the observed deep earthquakes and their potential triggering mechanisms. Nevertheless, it is possible to make observations regarding the conditions necessary for these mechanisms. In particular, it is known that deep earthquakes are confined to regions where subducting slabs have relatively low temperatures (<900 to 1000 °C), as at temperatures above this range stresses are relaxed via viscous deformation [Billen, 2020]. Further, it has been shown that failure by both shear thermal instability [Ohuchi et al., 2017, Thielmann, 2018] and transformational faulting [Burnley et al., 1991] is influenced by high strain rate. It has been suggested [Billen, 2020] that deep seismicity may occur preferentially in regions of locally high strain rates. Figure 4.6 shows the second invariant of the (deviatoric) strain rate for our best models. It is encouraging that our models, such as that shown in Fig. 4.6c, yield an increase in strain rate just below 660 km depth within the folded slab, perhaps consistent with observed seismicity at $\sim$ 680 km. The picture above 660 km is less clear, however, as strain rates there appear to be lower, but this may be due to the omission from our models of the secondary phase transitions involving akimotoite (silicate ilmenite) and garnet which have been shown to elevate strain rates in the depth range of 550-650 km [Billen, 2020].

Finally, we note the apparent restriction of deep earthquakes with unusual subhorizontal compressive stresses to the vicinity of the upper surface of the slab, which might lead to speculation about the consistency of such an observation with dehydration-related mechanisms of seismogenesis[Ishii and Ohtani, 2021].

5. Slab buckling as a driver for rapid oscillations in Indian plate motion and subduction rate

This chapter was published as [van der Wiel et al., 2024] in Communications Earth & Environment (Erik van der Wiel and Jakub Pokorný contributed equally to this work)

5.1 Introduction

Plate kinematic reconstructions provide the quantitative constraints that underpin our understanding of the driving and resisting forces of plate tectonics: primarily slab pull and to a lesser extent,ridge push as driving forces [Forsyth and Uyeda, 1975, Lithgow-Bertelloni and Richards, 1998], and mantle drag as either driving or resisting plate motion (particularly by continental keels or slabs), and the resistance on subduction interfaces, as main additional forces [Behr and Becker, 2018, Coltice et al., 2019, Spakman et al., 2018]. An important constraint on plate reconstruction and relative plate motions since the Mesozoic is provided by marine magnetic anomalies that reveal plate motion change on various temporal scales. Reconstructions of major ocean basins usually provide one average Euler pole (plate motion data point) for stages of 3-10 Ma [e.g. Müller et al., 2019], even though more magnetic anomalies can be present in such stages. Such reconstructions reveal gradually changing plate motions on tens of millions of year time scales with occasional sudden cusps in plate motion between stages [Gordon et al., 1984, Torsvik et al., 2008, Doubrovine et al., 2012, Müller et al., 2022]. Gradual plate motion changes can be explained by changes in slab pull for example due to slow age variation of subducting lithosphere [Goes et al., 2011, Sdrolias and Müller, 2006], or in the lubrication of plate contacts by a sedimentary cover [Behr and Becker, 2018]. Cusps may correspond to changes in contributing forces through e.g., changes in slab pull due to subduction initiation or arrest [Pusok and Stegman, 2020, Gürer et al., 2022, Hu et al., 2022], by slab detachment [Bercovici et al., 2015] or resistance to subduction of large oceanic plateaus [Knesel et al., 2008], the arrival of a mantle plume-head that may lubricate or push plates [van Hinsbergen et al., 2011, 2021], or to the decrease of a plate area through breakup [e.g. Wortel and Cloetingh, 1981]. Only recently, high-resolution (0.5-1 Ma) plate kinematic reconstructions of India-Africa spreading during the Eocene [DeMets and Merkouriev, 2021] revealed surprisingly variable ocean spreading kinematics.

It has long been known that the spreading rate between India and Africa, and the convergence rate between India and Asia, between 65 and 50 Ma, was very high, close to 20 cm/a [Patriat and Achache, 1984, van Hinsbergen et al., 2011]. Those estimates were based on about one Euler pole every 5 Ma. White and Lister [2012] suspected that shorter-wavelength plate velocity oscillations may have occurred although being smoothed out in existing global plate tectonic reconstructions. Their suspicion was recently corroborated by the high-resolution

magnetic anomaly study of [DeMets and Merkouriev, 2021], which revealed that the interval of high India-Asia convergence rate contained rapid oscillations with an amplitude of 10 cm/a or more at a period of 6-8 Ma (see Fig.5.1). Such plate motion variations suggest oscillating changes in either slab pull, or friction on the plate contact with the mantle or the overriding plate, or a combination thereof may become more pronounced with higher rates of subducting plate motion.

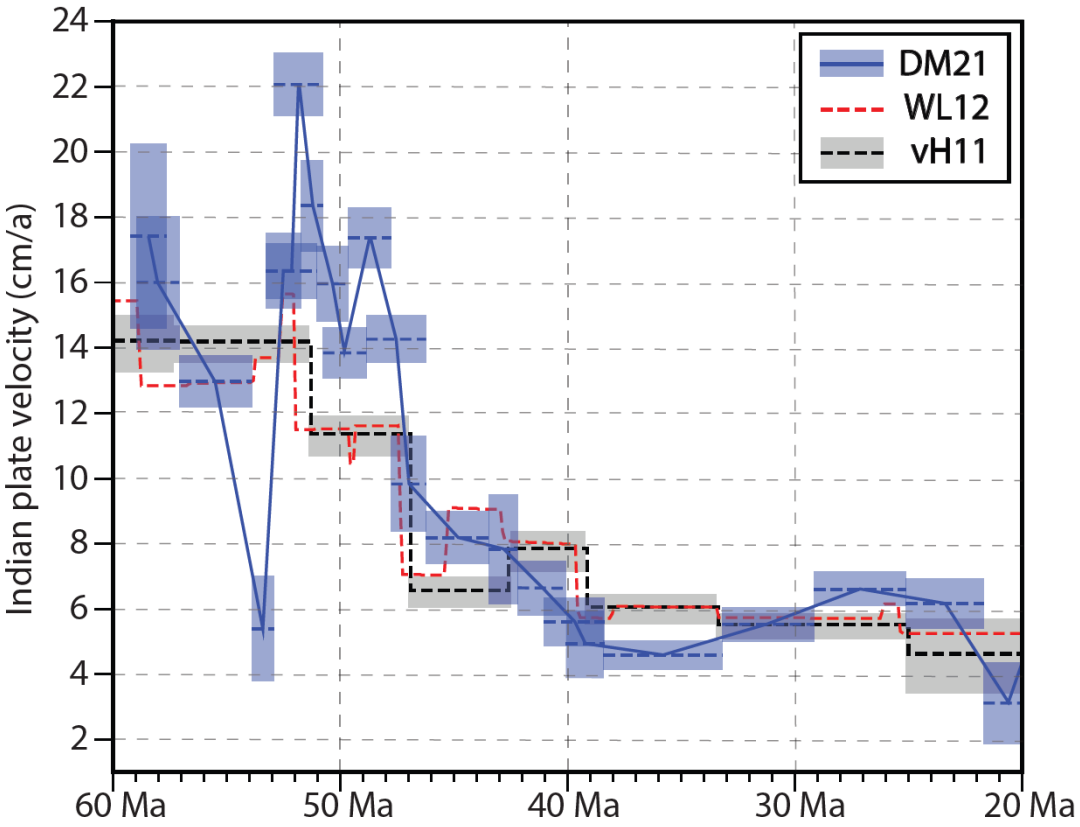

Figure 5.1: Indian plate velocity relative to Eurasia from 60 Ma ago to 20 Ma ago. Shown are the reconstructed velocities of the Indian plate from DM21 [DeMets and Merkouriev, 2021], WL12 [White and Lister, 2012] and vH11 [van Hinsbergen et al., 2011]. Blue and grey rectangles indicate error margins in reconstructions and time interval spanned by each stage velocity.

Subducting plate motions and changes therein must be accommodated in the underlying mantle. Correlations between imaged mantle structure and the global geological record of subduction show that the remnants of detached slabs in the lower mantle sink with rates of 1-1.5 cm/a, almost regardless of the rate at which they subducted at a trench [Butterworth et al., 2014, van der Meer et al., 2010, 2018]. Therefore, subducting slabs eventually decelerate from plate tectonic rates (up to 20-25 cm/a) [Hu et al., 2022, Zahirovic et al., 2015] to average lower mantle sinking rates of < 1.5 cm/a. To accommodate this requires some form of slab shortening or thickening. For instance, seismic tomographic imaging of the lower mantle below India have revealed a major, sufficiently resolved, 'thick' anomaly that is widely interpreted to represent the bulk of the Indian plate lithosphere that subducted since the Cretaceous onset of India-Asia convergence, including the lithosphere that subducted between 65 and 50 Ma [Van der Voo et al., 1999,

Replumaz et al., 2004, Parsons et al., 2021, Qayyum et al., 2022]. Its enormous volume represents much of the 8000 km of the India-Asia convergence, and the lithosphere involved must thus have drastically thickened during subduction [van der Meer et al., 2018]. Subduction modelling reveals that the deceleration of slabs in the mantle leads to thickening by slab buckling [Ribe et al., 2007, Goes et al., 2017]. Such buckling behaviour and the resulting stress field in the slab were shown to explain occurrence of earthquakes in the deepest upper mantle [Billen, 2020, Pokorný et al., 2023]. Even though the lower mantle tomographic resolution below India cannot resolve the internal buckling structure of the Indian slab remnant, detailed tomographic analyses of slabs in the mantle transition zone and in the top of the lower mantle elsewhere have shown slab buckling in the mantle transition zone [Chen et al., 2019, Wu et al., 2016]. Moreover, kinematic reconstruction of those tomographically imaged slabs, through systematic unfolding, reconstructed areas of lost lithosphere that reproduce plate kinematic reconstructions of convergence [Chen et al., 2019, Wu et al., 2016]. Such buckling, which potentially may become more pronounced with faster subduction, makes slabs fold backward and forward, creating an oscillating slab dip and slab motion [Schellart, 2005, Lee and King, 2011, Čížková and Bina, 2013, Garel et al., 2014, Holt et al., 2015, Billen and Arredondo, 2018, Xue et al., 2022]. Here, we hypothesize that pronounced slab buckling causes the rapid, large-amplitude Eocene plate motion fluctuations of India.

To test this hypothesis, we conduct numerical experiments with decoupled, freely subducting plates that buckle in the mantle transition zone, creating periodically changing plate motions [Pokorný et al., 2021]. We evaluate under which conditions fluctuations such as those reported for the India plate may occur. We will discuss our results in terms of the implications for our understanding of the driving forces of plate tectonics, and how obtaining detailed marine magnetic anomaly records may aid improving the predictive power of plate tectonic reconstructions for applications to plate boundary deformation and magmatic or mineralization processes.

5.2 Methods and model setup

A set of partial differential equations in an extended Boussinesq approximation [EBA; Ita and King, 1994] is used to describe our numerical model of subduction. These equations are solved by a finite element method implemented in the SEPRAN package [Segal and Praagman, 2005, van den Berg et al., 2015]. Our model domain is represented by a 2D box 10,000 km wide and 2,000 km deep . The subducting plate stretches from the ridge in the upper left corner to the trench in the middle of the upper surface. The initial temperature distribution in the subducting plate follows a half-space model followed by an adiabatic profile with a potential temperature of 1573 K beneath it.

We carried out two sets of simulations with similar matching parameters. The first set with an overriding plate that is allowed to move freely (subduction with possible rollback), while the second set features a fixed overriding plate (stationary trench – restricted rollback). Our overriding plate is modelled as a rigid

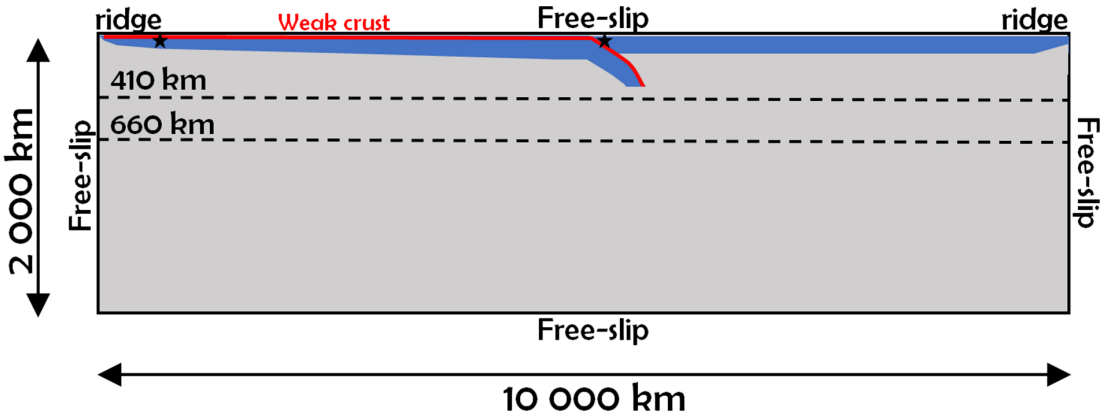

Figure 5.2: Model domain is 10 000 km wide and 2000 km deep. Dashed lines indicate major phase transitions at 410 and 660 km depth. Red line positioned at the top of the subducting slab indicates a 10 km thick weak crustal layer, effectively separating the plates. Two black asterisks represent tracers used to track the velocity of the subducting plate and overriding plate. Free slip boundary condition is prescribed on all boundaries.

undeformable plate, with a thickness controlled by the thermal age, as there is no evidence for upper plate extension in Tibet. Figure 5.2 illustrates time evolution of a reference model for both sets of simulations. In these reference models we assume a subducting and overriding plate age of 100 Ma at the trench and the viscosity of the crustal decoupling layer of 10^{20} Pa s.

Models of the first set have a mobile overriding plate with a ridge in the upper right corner. The rollback of trench induces the motion of the entire overriding plate towards the left, which is facilitated by the presence of a hot and low-viscosity mid-ocean ridge. The second set of models has a stagnant overriding plate with an age increasing from approximately ∼17 Ma at the right hand side to 100 Ma (i.e., for the reference model) at the trench. Cold and thus strong overriding plates cannot move to the left because of the impermeable free slip condition on the right vertical boundary. Therefore, rollback is prohibited and the trench remains stagnant during the model run. We evaluated the effects of the age of the subducting and overriding plates [Garel et al., 2014, Capitanio et al., 2010] – we tested ages at the trench ranging from 50 Ma to 200 Ma.

To obtain an initial slab with sufficient negative buoyancy that would facilitate subduction, we first execute a short kinematic run to develop the slab tip to a depth of approximately 200 km. Within this kinematic prerun a constant convergence velocity of 2.5 cm/a is prescribed on the top of the subducting plate. After 6 Ma the kinematic boundary condition is turned off and an impermeable free slip is prescribed on all boundaries.

Top and bottom model boundaries are considered isothermal with respective temperatures of 273 K and 2132 K while the vertical boundaries have zero heat flux. Thermal diffusivity is constant $10^{-6}\, m^2\, s^{-1}$ while thermal expansivity is depth dependent [Katsura et al., 2009] and decreases with depth from $3 \times 10^{-5}\, K^{-1}$ at the surface to $1.2 \times 10^{-5}\, K^{-1}$ at the bottom of the model domain (Hansen et al.,

1993).

We consider the major mantle phase transitions: the polymorphous exothermic transition of forsterite to wadsleyite at 410 km depth and the endothermic transition of ringwoodite to bridgmanite and periclase at a depth of 660 km with their associated petrological density contrasts (Table 5.1).These are incorporated through the harmonic parameterization [Čížková et al., 2007] of a phase function [Christensen and Yuen, 1985]. We first performed a parametric study where we varied the values of Clapeyron slopes in a usually accepted range ($\gamma_{410} = 1 - 3$ MPa/K, $\gamma_{660} = -2.5 - (-1.5)$ MPa/K) [Morishima et al., 1994, Bina and Helffrich, 1994, Katsura et al., 2003, 2004, Fei et al., 2004, Litasov et al., 2005, Litasov et al., Ishii et al., 2011, Su et al., 2022]. All these models result in quasiperiodic buckling of the slab, with observed periods of oscillations between ∼10-20 Ma. The style of buckling, like the interaction of a slab with the MTZ and the lower mantle, also depends on the strength of the Clapeyron slopes [Čížková et al., 2012, Pokorný et al., 2021]. Higher Clapeyron slope forthe 410-km phase transition increases slab pull and results in tighter folds while lower Clapeyron slopes reduce the slab pull with fast rollback and as a consequence lead to a lower slab dip [Čížková and Bina, 2013]. A stronger 660-km phase transition would result in reduced buckling periods. Based on the parametric study we chose a relatively strong $\gamma_{410} = 3$ MPa/K and weak $\gamma_{660} = -1.5$ MPa/K for the phase transitions. These values were chosen to accommodate realistic subduction behaviour, from subducting plate velocities [Zahirovic et al., 2015], to the transfer and sinking rates of slabs in the lower mantle, while still agreeing with results from X-ray diffraction experiments and thermodynamic estimates [Morishima et al., 1994, Bina and Helffrich, 1994, Katsura et al., 2003, 2004, Fei et al., 2004, Litasov et al., 2005, Litasov et al., Ishii et al., 2011, Su et al., 2022].

To evaluate the subducting plate velocity and trench retreat velocity in our models we use two passive particles, one initially positioned in the subcrustal lithosphere of the subducting plate (4600 km left of the trench) and the other one in the overriding plate close to the trench (Fig. 5.2).

5.2.1 Rheological description

Our subduction model incorporates crustal and mantle material. A low-viscosity crustal layer facilitating mechanical decoupling of the subducting and overriding plate is initially positioned along the top of the subducting plate and within the subduction channel (Fig. 5.2). Crustal material is tracked using 2 million tracers prescribed in the crust and its closest vicinity. The initial thickness of the crustal layer is 10 km.

Upper mantle material is described by a composite rheology model [Čížková et al., 2002, van den Berg et al., 1993] combining dislocation creep, diffusion creep and a power-law stress limiter which effectively approximates the Peierls creep [Androvičová et al., 2013].

In the diffusion and dislocation creep equations (eq. 5.1 and 5.2), the pressure and temperature dependence of viscosity follows Arrhenius law:

$$\eta_{diff} = A_{diff}^{-1} \exp\left(\frac{E_{diff} + pV_{diff}}{RT}\right) \tag{5.1}$$

$$\eta_{disl} = A_{disl}^{-1/n} \dot{\varepsilon}_{||}^{(1-n)/n} \exp\left(\frac{E_{disl} + pV_{disl}}{nRT}\right) \tag{5.2}$$

$$\eta_y = \sigma_y \dot{\varepsilon}_y^{-(1/n_y)} \dot{\varepsilon}_{||}^{(1/n_y)-1} \tag{5.3}$$

$$\eta_{eff} = \left(\frac{1}{\eta_{diff}} + \frac{1}{\eta_{disl}} + \frac{1}{\eta_y}\right)^{-1}, \tag{5.4}$$

Here $A_{diff/disl}$, $E_{diff/disl}$,, $V_{diff/disl}$ are pre-exponential parameter, activation energy, activation volume for diffusion and dislocation creep, $\dot{\varepsilon}_{||}$ is the second invariant of the strain rate tensor and n is the power-law exponent of the dislocation creep. A power law stress limiter viscosity is parametrized through the yield stress σ_y , reference strain rate $\dot{\varepsilon}_y$ and a power-law exponent n_y , which is set to 10 in our models (eq.5.3). Assuming unique stress, individual creep mechanism viscosities are combined into the effective viscosity through equation 5.4.

The lower mantle deformation is assumed to be mainly through diffusion creep [Karato et al., 1995], therefore we take $\eta_{eff} = \eta_{diff}$ in the lower mantle. Prefactor A_{diff} and activation parameters of lower mantle diffusion creep are based fitting the slab sinking rates, reported to be 10-15 mm/a [van der Meer et al., 2018]. The viscosity contrast between the lower and upper mantle is about an order of magnitude [Čížková et al., 2012].

The crust in our models is mostly assumed to have constant viscosity in a range of $\eta_c = 5 \times 10^{19} - 5 \times 10^{20}$ Pa s. We have also conducted several tests with the composite nonlinear rheology of the crust [Pokorný et al., 2021] combining dislocation creep [Ranalli, 1995] and a Byerlee type deformation [Karato, 2008] as an approximation of the brittle failure (pseudoplastic deformation). In these models, dislocation creep viscosity follows equation 5.5 (similar to equation 5.2), but the parameters A_c, E_c, V_c and n_c differ from mantle parameters of equation 5.2 (see table 5.1).

$$\eta_{disl}^c = A_c^{-1/n_c} \dot{\varepsilon}_{||}^{(1-n_c)/n_c} \exp\left(\frac{E_c + pV_c}{n_c RT}\right) \tag{5.5}$$

Pseudoplastic deformation limits the maximum stress in the crust to σ_y^c, where this stress limit increases with lithostatic pressure p through equation 5.6, here τ_c is the cohesion and μ is the friction coefficient. The pseudoplastic viscosity η_{pl} is then defined by equation 5.7 and the effective crustal viscosity is given by equation 5.8.

$$\sigma_y^c = \tau_c + \mu p, \tag{5.6}$$

$$\eta_{pl} = \frac{\sigma_y^c}{2\dot{\varepsilon}_{||}}, \tag{5.7}$$

$$\eta^c_{eff} = \left(\frac{1}{\eta^c_{disl}} + \frac{1}{\eta^c_{pl}} \right)^{-1}. \tag{5.8}$$

Table 5.1
Model parameters

symbol	Meaning	Value	Units
Upper mantle rheology			
A_{diff}	Pre-exponential parameter of diffusion creep[a]	1×10^{-9}	$Pa^{-1}\ s^{-1}$
A_{disl}	Pre-exponential parameter of dislocation creep[a]	31.5×10^{-18}	$Pa^{-n}\ s^{-1}$
E_{diff}	Activation energy of diffusion creep[a]	3.35×10^5	$J\ mol^{-1}$
E_{disl}	Activation energy of dislocation creep[a]	4.8×10^5	$J\ mol^{-1}$
V_{diff}	Activation volume of diffusion creep[a]	4.0×10^{-6}	$m^3\ mol^{-1}$
V_{disl}	Activation volume of dislocation creep[a]	11×10^{-6}	$m^3\ mol^{-1}$
η_{diff}	Viscosity of diffusion creep	–	$Pa\ s$
η_{disl}	Viscosity of dislocation creep	–	$Pa\ s$
η_y	Power-law stress limitor viscosity	–	$Pa\ s$
n	dislocation creep exponent	3.5	–
$\dot{\epsilon}_y$	Reference strain rate	1×10^{-15}	s^{-1}
σ_y	Stress limit	$2 - 5 \times 10^8$	Pa
p	Hydrostatic pressure	–	Pa
n_y	Stress limit exponent	10	–
R	Gas constant	8.314	$J\ K^{-1}\ mol^{-1}$
T	Temperature	–	K
$\dot{\epsilon}_{\|}$	Second invariant of strainrate	–	s^{-1}
Lower mantle rheology			
A_{diff}	Pre-exponential parameter of diffusion creep	1.3×10^{-16}	$Pa^{-1}\ s^{-1}$
E_{diff}	Activation energy of diffusion creep[b]	2×10^5	$J\ mol^{-1}$
V_{diff}	Activation volume of diffusion creep[b]	1.1×10^{-6}	$m^3\ mol^{-1}$
Other model parameters			
η_c	Range of constant viscosity crust values	$5 \times 10^{19} - 5 \times 10^{20}$	$Pa\ s$
κ	Thermal diffusivity	10^{-6}	$m^2\ s^{-1}$
g	Gravitational acceleration	9.8	$m^2\ s^{-2}$
ρ_0	Reference density	3416	$kg\ m^{-3}$
c_p	Specific heat	1250	$J\ kg^{-1}\ K^{-1}$
α_0	Surface thermal expansivity	3×10^{-5}	K^{-1}
γ_{410}	Clapeyron slope of 410 km phase transition[c]	3×10^6	$Pa\ K^{-1}$
γ_{660}	Clapeyron slope of 660 km phase transition[c]	-1.5×10^6	$Pa\ K^{-1}$
$\delta_{\rho 410}$	Density contrast of 410 km phase transition[d]	273	$kg\ m^{-3}$
$\delta_{\rho 660}$	Density contrast of 660 km phase transition[d]	341	$kg\ m^{-3}$
Nonlinear crustal rheology			
A_c	Pre-exponential parameter of dislocation creep	2.5×10^{-17}	$Pa^{-1}\ s^{-1}$
E_c	Activation energy of dislocation creep	1.54×10^5	$J\ mol^{-1}$
V_c	Activation volume of dislocation creep	0	$m^3\ mol^{-1}$
n_c	dislocation creep exponent	2.3	–
τ_c	Cohesion	$0.25 - 1 \times 10^7$	Pa
μ_c	Friction coefficient	$0.025 - 0.1$	–
σ^c_y	Stress limit in the crust	–	Pa

(a) Parameters of wet olivine based on Hirth and Kohstedt (2003).
(b) Čížková et al. (2012).
(c) Bina and Helffrich (1994).
(d) Steinbach and Yuen (1995).

5.3 Results

We conducted experiments in a 2D numerical model of subduction (see hods 5.2). The rheology of the upper and lower mantle [Čížková et al., 2012, Čížková and Bina, 2013, 2019] was chosen to accommodate typical subduction velocities [Zahirovic et al., 2015] that in the upper mantle exceed the inferred lower mantle slab sinking rates. The average slab sinking rates of 10-15 mm/a [van der Meer et al., 2018] are consistent with approximately one order of magnitude viscosity contrast between the lower and upper mantle [Čížková et al., 2012]. This mantle rheology leads to slab shortening and buckling in the upper-to-lower mantle transition zone (MTZ). We experimented with varying lithospheric ages to assess the effect of varying oceanic lithosphere thickness, and with varying crustal viscosities to assess the effect of average plate motion on the amplitude and period of the plate motion. Our slabs have a stress limit of 0.2 GPa and for all the models presented here we use Clapeyron slopes $\gamma_{410} = 3$ MPa/K and $\gamma_{660} = -1.5$ MPa/K. We conducted one group of experiments, with a free overriding plate which leads to slab rollback and results in low angle buckling with multiple buckles [Christensen, 1996] (partly) present above the 660 km discontinuity, and lower mantle slab sinking rates (Figure 5.3 a-g). Another group of experiments implements a fixed overriding plate that suppresses the development of rollback, such that subduction occurs at a mantle-stationary trench (Figure 5.3 h-n). This generates buckling into a near-vertical slab-pile [Běhounková and Čížková, 2008] that slowly sinks into the lower mantle leaving at any time only one buckle present above the 660 km discontinuity.

Slab shortening occurs through the combined resistance of the more viscous lower mantle and the endothermic phase change at the 660 km boundary, while the shallower part of the slab is continuously pulled by the exothermic phase change at 410 km (see methods 5.2). Buckling of the shortening slab is then controlled by the non-linear power-law stress limiting mechanism (see methods 5.2) [Pokorný et al., 2021]. We assess the horizontal velocity of the subducting plate V_{SP} and upper plate V_{UP} as an effect of lithospheric thickness (corresponding to the age of lithosphere at the trench) or through weakening subduction interfaces (crustal viscosity) to evaluate causal relationships between subduction dynamics and oscillating plate motions.

5.3.1 Slab buckling in the reference models

Figure 5.3 shows two reference experiments for the model setups with and without roll-back. These have a crustal viscosity of 10^{20} Pa s and overriding and subducting plate ages at the trench of 100 Ma. In the model with a mobile overriding plate (Fig. 5.3 a-g), the slab undergoes a rapid, vertical descent through the upper mantle and the tip reaches the 660 km discontinuity after approximately 5 Ma model time. The slab in the transition zone experiences down-dip compression which leads to (nonlinear) rheological weakening, causing the slab to buckle forwards (Fig. 5.4 a) (i.e., towards the overriding plate) over the trapped tip that started to penetrate the 660 km discontinuity. Next, the slab buckles backward (i.e. towards the downgoing plate).

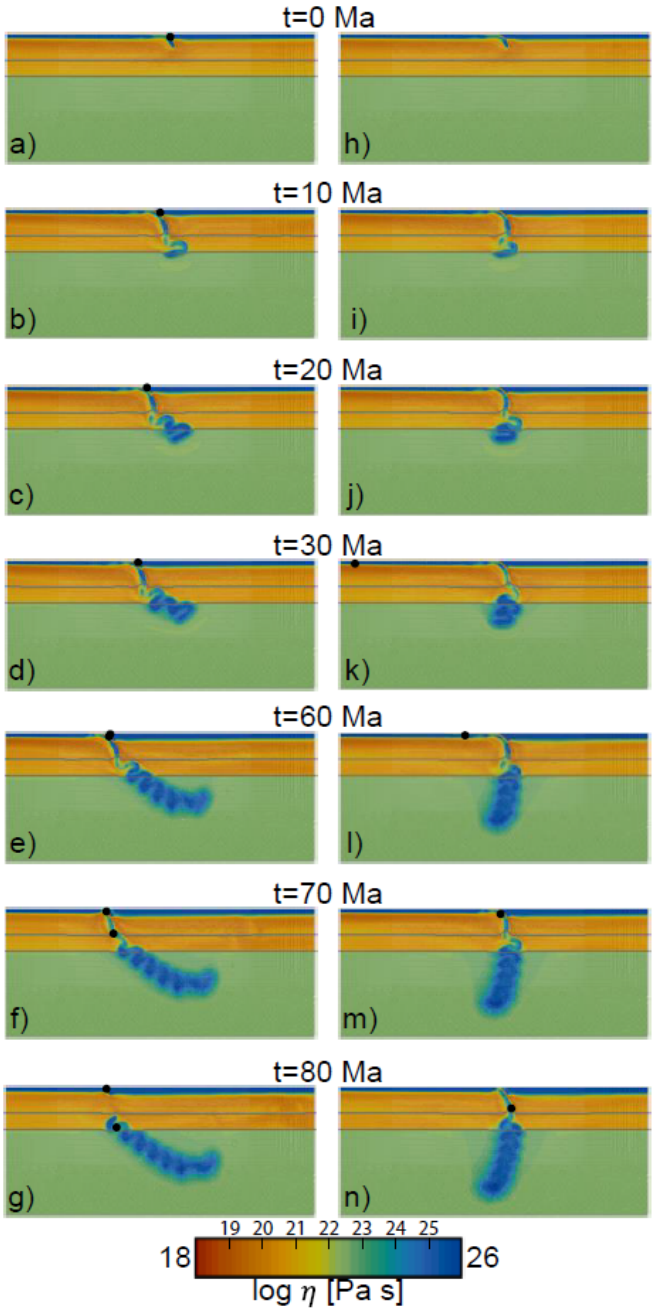

Figure 5.3: Zoomed-in viscosity snapshots (4800x2000 km) of the model for 80 Ma of model time. Grey lines indicate position of the major phase transition at 410 and 660 km depth with the values of Clapeyron slopes of 3 and -1.5 MPa/K, respectively. Black dots are reference points used to calculate plate velocities. a-g) Reference model with free moving overriding plate resulting in trench retreat and an inclined slab in the lower mantle. h-n) Reference model with a stationary trench creating a vertical lower mantle slab.

This leads to an episode of roll-back and short-lived V_{SP} increase until the slab is almost vertically oriented at t = 11 Ma (Fig. 5.4 b). This is followed by the initiation of a second forward buckle, folding the slab over its deeper part in the MTZ, between t = 11 Ma and 18 Ma, associated with rollback and a decrease of V_{SP} and increase of V_{UP} (Fig. 5.4 b & 5.5 a). This forward buckle starts

tightening at t= 18 Ma, inducing the next backward buckle which is followed by a rapid increase of V_{SP} up to 12 cm/a, accompanied by a decrease of V_{UP} to almost 0 cm/a (Fig. 5.5 a). At t=20 Ma the next forward buckle initiated (Fig. 5.3 c), resulting again in an episode of rollback with decreasing V_{SP} and increasing V_{UP} (Fig. 5.4 a & 5.5 a).

From here on, this process repeats itself quasi-periodically with new buckles forming approximately every 10 Ma (Fig. 5.3 c-f). This continuous subduction and rollback creates a buckled and thickened slab which slowly enters the lower mantle at an overall low-angle orientation (Fig. 5.3 d-g). After 70 Ma and 5000 km of subduction, the weak crust that facilitates the modelled subduction (see methods 5.2) is entirely consumed, the subducting plate is locked to the overriding plate and subduction stops. The modelled slab detaches and sinks into the lower mantle at a rate of $\sim$ 1 cm/a, on par with inferred and modelled lower mantle slab sinking rates [Čížková et al., 2012, van der Meer et al., 2018]. Throughout the experiment, and after 70 Ma of modelled convergence, the overriding plate and trench moved $\sim$ 1000 km in absolute motion, i.e., relative to the mantle, towards the subducting plate.

The model with a fixed overriding plate, which suppresses rollback (Fig. 5.3 h-n), shows similar characteristics. The slab is compressed down-dip and rheologically weakened in the transition zone, also resulting in the formation of a second buckle at around t=10 Ma (Figure 5.3 i). The tightening of the buckle at the base of the upper mantle coincides with an increase in plate velocity around t=15Ma (Fig. 5.5 b). Due to the absence of rollback, the buckled slab is oriented vertically, like previously conceptualised 'slab walls' [Sigloch and Mihalynuk, 2013]. The oscillations in V_{SP} are of lower amplitude, on the order of 2 cm/a, recurring in a $\sim$ 12 Ma period (Fig. 5.5 b). Absolute motion rates and oscillations therein of the subducting plate are similar to the scenario with roll-back but because the upper plate is fixed and roll-back does not add to the net convergence rate, subduction continued for $\sim$90 Ma in model time, after which, the modelled slab detached and descended through the lower mantle with similar rate as in the reference model with rollback.

5.3.2 Plate motion variations caused by buckling

The quasiperiodic buckling of the subducting plate in the MTZ causes oscillations in the subduction velocity for both types of models (5.5) and in the motion of the overriding plate in the models that allow for roll-back (5.5 a). Intervals of fast V_{SP} coincide with tightening of a buckle and steepening of the slab and are followed by a minimum in the V_{UP} (Fig. 5.5). We represent the periodicity of these plate motions with an amplitude and period, which we calculate in a 40 Ma time-interval of steady-state oscillations after subduction initiation and initial descend of the slab to the mantle transition zone, and before the end of the experiment (Fig. 5.5). In this 40 Ma time interval we calculate an average subduction velocity $V_{SP,ave}$ as well as an amplitude and period of oscillations. The amplitude is calculated as the average difference between the maxima and minima of V_{SP}, the period reflects the time for a full buckle to form. In the ref-

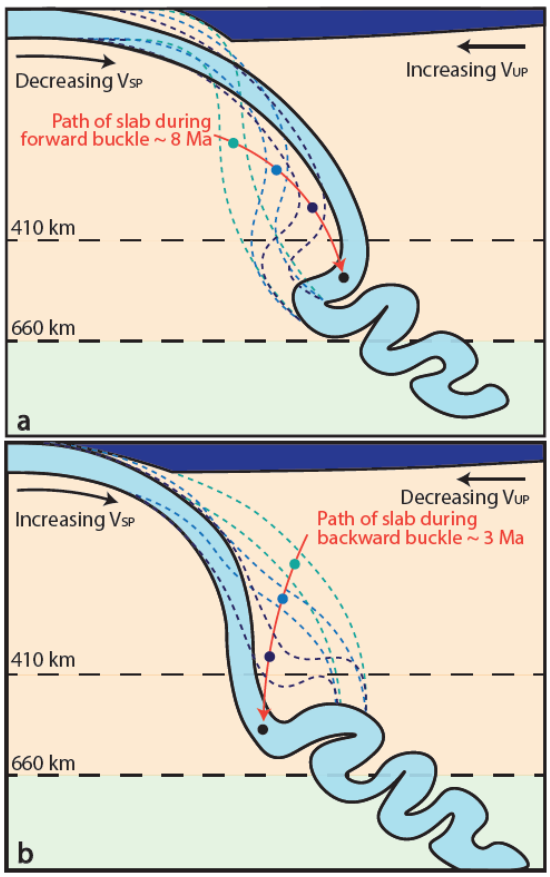

Figure 5.4: A cartoon illustrating forward (a) and backward (b) slab buckling as result of the interplay of the slab with the phase transitions and the lower mantle. During forward buckling the slab in the MTZ advances while the trench retreats, accompanied by a decreasing V_{SP} and increasing V_{UP}. The backward buckle allows the slab to sink fast in the MTZ with a rapid increase of V_{SP}, while the trench stays mantle stationary. The backward buckles form faster than forward buckles, in about 3 versus 8 Ma for our reference model.

erence model with rollback, the subducting plate moved between 20 and 60 Ma with an average $V_{SP,ave}$ of 5.1 cm/a while oscillating between $\sim$ 2 and 10 cm/a (Fig. 5.5 a). The average amplitude and period of the V_{SP} oscillations are 6.8 cm/a and 9.8 Ma (Fig. 5.5 a). Motion of the rigid, undeformable overriding plate, follows the oscillatory motion of the retreating trench. In the 20-60 Ma interval the overriding plate has an average V_{UP} of 1.8 cm/a towards the subducting plate, with oscillations between $\sim$ 0 and 3 cm/a (Fig. 5.5a). Maxima in trench motion and V_{UP} coincide with minima in V_{SP}, both occurring during formation of a new forward buckle and the associated shallowing of slab dip. During tightening of the buckle, the slab rolls back from inclined to vertical, associated with a sharp rise in V_{SP}, this change in angle is associated with a temporally near-stationary trench, and a resulting decrease in V_{UP} towards 0. The total convergence rate (V_C) then also oscillates (Fig. 5.6 a), with an amplitude of 6 cm/a, about 1 cm/a smaller than the amplitude of V_{SP}. The motion of the subducting plate accounts for 50-100 % of the total convergence, while the overriding plate is only responsible for 50-0 % (Fig. 5.6 b). The highest contribution of trench motion to the

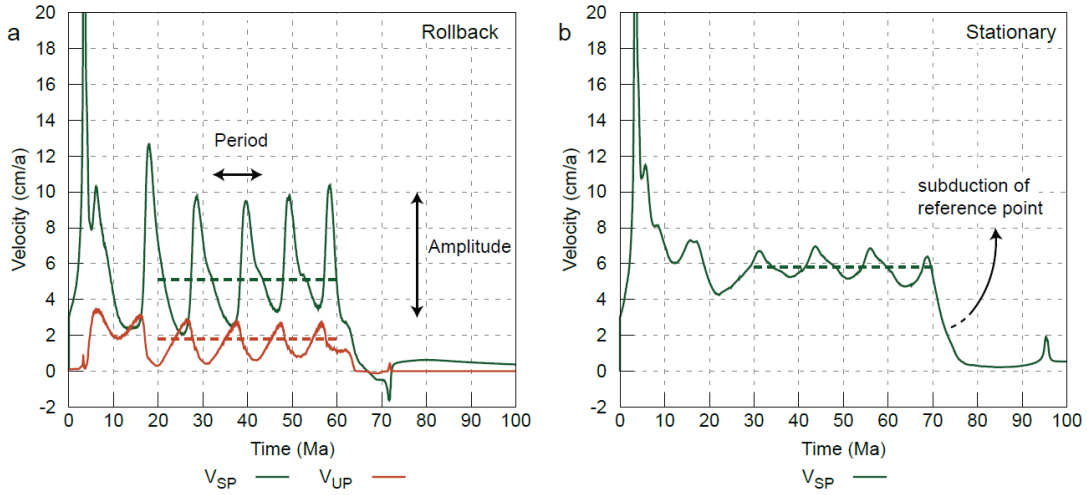

Figure 5.5: Temporal evolution of the plate motions in both reference models. a) Subduction velocity and overriding plate motion of the reference model with rollback, V_{SP} oscillates between 2 and 10 cm/a and V_{UP} between 0 and 3 cm/a. The reference point subducts at t = 60 Ma and slab detachment occurs around t = 70 Ma. b) Similar as in a but for the reference model with a stationary trench, subduction of the reference point occurs at t = 70 Ma and slab detachment at t = 90 Ma. The dashed lines indicate the average velocity, which is calculated over the shown 40 Ma time-interval.

convergence occurs during periods of minimal V_{SP}.

The reference model with a fixed overriding plate (Fig. 5.3 h-n), for which the trench is stationary with respect to the mantle, also shows oscillations in V_{SP} (Fig. 5.5 b) caused by the buckling of the overall vertical slab in the MTZ. In the 40 Ma long time-interval (here, between 30-70 Ma) quasiperiodic buckling occurs with an average V_{SP} of 5.7 cm/a (Fig. 5.5 b), faster than the model with rollback. The oscillations in V_{SP} occur with a period of 12.7 Ma and an amplitude of 1.6 cm/a. This amplitude is more than 4 times lower than the amplitude of oscillations in the model with rollback. The freedom to roll back allows for much larger variation in slab dips, and results in higher amplitudes of plate motion oscillations, as well as a higher net convergence rate.

5.3.3 How subduction velocity controls plate motion oscillations

When lithosphere subducts at a rate of $V_{SP,ave}$ 5-6 cm/a as in our reference models, it can reach the 660-discontinuity 13-11 Ma after passing the trench. Higher subduction rates decrease that time interval and increase the amount of subducted slab in the MTZ, creating an accommodation space problem. We performed numerical experiments to evaluate the effect of subduction speed on the formation of buckles and on oscillations in V_{SP}. We modified the subduction rate in our experiments in two ways. On the one hand, we performed experiments with constant crustal viscosity while varying the age of the overriding and subducting plates. Overriding plate age determines the length of the subduction interface,

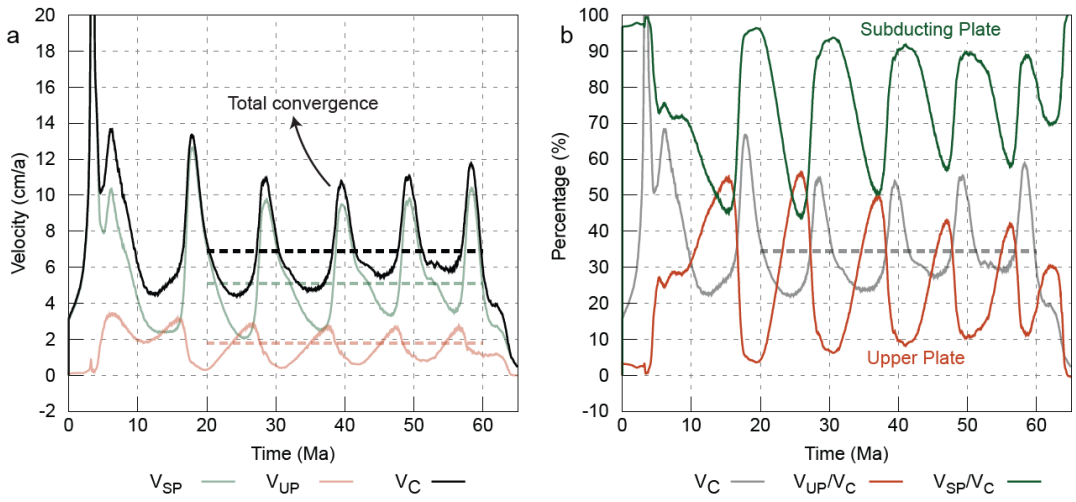

Figure 5.6: a) Total convergence rate ($V_C = V_{SP} + V_{UP}$) of the reference model with rollback showing smaller amplitudes in the oscillations, red and green lines are the same as in Figure 5.5 a. b) Relative percentages of the total convergence rate for both the subducting plate (green; 100-50%) and overriding plate (orange; 50-0%). Grey line is the same as in a, and uses the y-axis of a.

with larger interfaces giving more resistance against subduction, decreasing subduction velocity. Subducting plate age determines the negative buoyancy, with higher subduction velocities for older plates [Capitanio et al., 2011]. On the other hand, we performed experiments with constant lithosphere ages (100 Ma) while adopting a constant or a power-law crustal viscosity, with lower viscosity yielding higher V_{SP} [e.g Behr et al., 2022].

In our numerical experiments with varying plate age, the amplitude and period of the oscillations in plate velocity depend on the average subduction velocity (Fig. 5.7 & Fig. 5.8 a-f). Models with a younger overriding plate and therefore a shorter subduction interface, have higher average subduction velocities within the 40 Ma long time-interval with steady-state, quasi-periodic buckling (Fig. 5.8 a,b). These velocities correlate directly to larger amplitudes (2-9 cm/a) in oscillations in the cases with rollback (Fig. 5.8 e). The cases with a stationary trench show that the amplitude of V_{SP} oscillations is predominantly determined by subducting plate age while the effect of the overriding plate age is limited. V_{SP} amplitudes vary between 1-3 cm/a (Fig. 5.8 f). Hence, faster-subducting plates have higher velocity amplitudes and shorter periods of oscillation, and analogous to our reference models, this trend is most profound in models that allow rollback, in which the amplitudes are 2-3 times larger than in models with a mantle-stationary trench (5.7).

The models with a varying constant crustal viscosity show the same trend: higher average V_{SP}'s leads to larger velocity oscillation amplitudes (Fig. 5.8 c,d) and shorter periods (Fig. 5.8 g,h). Models with a power law crustal viscosity have smaller variations in average V_{SP} between them than those with a constant viscosity and consequently also smaller variations in oscillation amplitudes, albeit with higher absolute amplitudes (Fig. 5.8 c,d). This is the result of feedback

mechanisms between the subducting plate velocity and the strain-rate dependent crustal power law viscosity [Pokorný et al., 2021]. Crustal viscosity dynamically responds to changes in slab velocity, where the viscosity decreases as plate velocity (and thus strain-rate) increase. This aids in keeping the period of V_{SP} oscillations constant (Fig. 5.8 g,h).

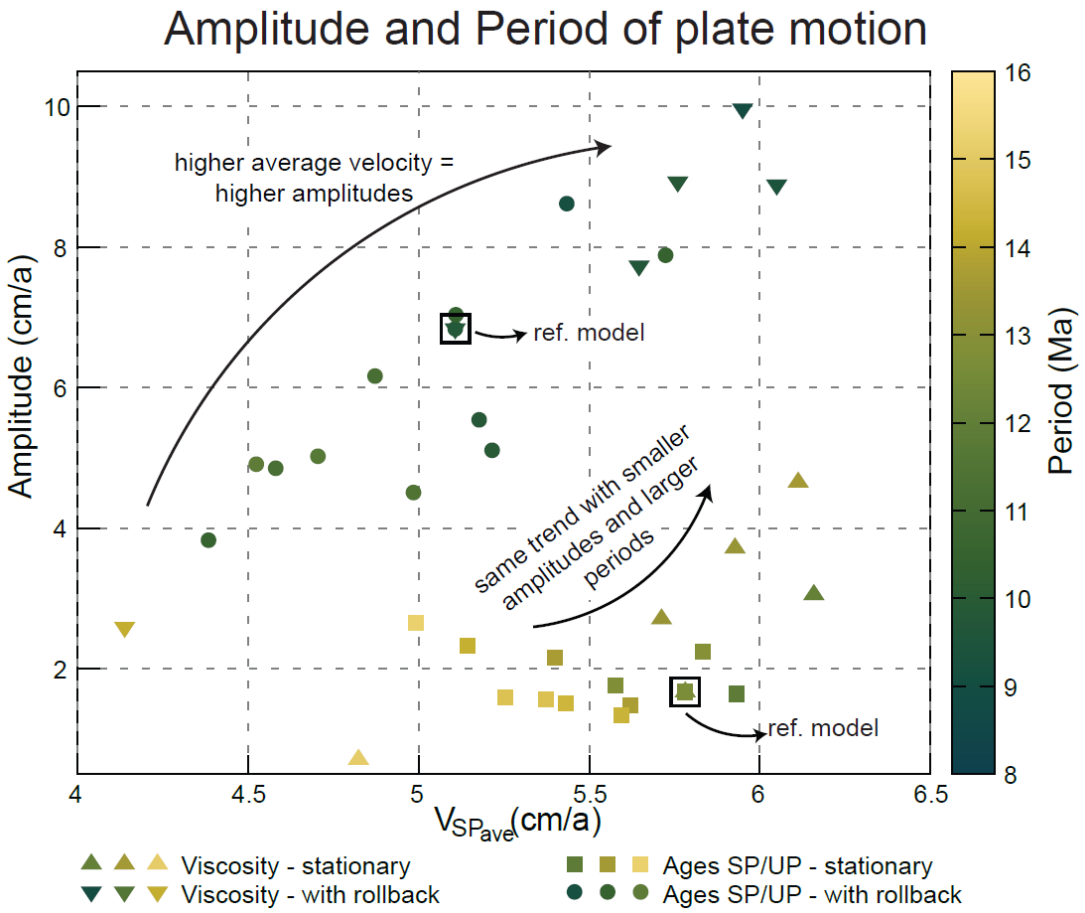

Figure 5.7: Overview of all models showing the relation the amplitude and period (colour) of V_{SP} oscillations have with the average V_{SP}. The four types of models shown are with a varying crustal viscosity and rollback (triangles) or a stationary trench (upside-down triangles), and models with changing SP and UP ages with rollback (circles) or a stationary trench (squares). For values of the crustal viscosity and ages of plates, see figure 5.8.

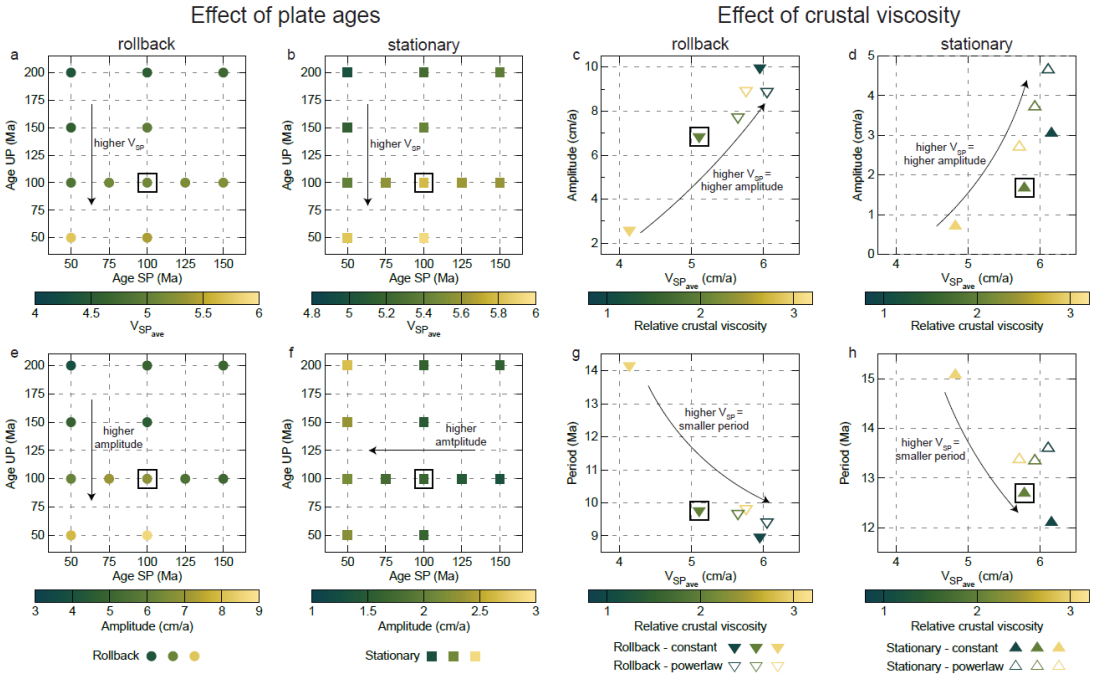

Figure 5.8: V_{SP} as function of SP and OP ages for models with a moving trench (a) and a stationary trench (b). Amplitude of the oscillating V_{SP} as function of the average V_{SP} for crustal viscosities: 5×10^{19}, 1×10^{20}, 5×10^{20} (closed triangles) and three power law crustal viscosities (open triangles) in models with a moving trench (c) and a stationary trench (d). Amplitude of the oscillating V_{SP} as function of SP and OP plate ages for models with a moving trench (e) and a stationary trench (f). Period of the oscillating V_{SP} as function of the average V_{SP} for a varying crustal viscosity in models with a moving trench (g) and a stationary trench (h).

5.3.4 Discussion

Slabs that subduct with plate motions exceeding the average lower mantle sinking rate of 1-1.5 cm/a [van der Meer et al., 2018] inevitably require that slabs shorten and thicken. Interpretations of geophysical observations and subduction models (cited above), including our own, show that this occurs through buckling of the slab in the MTZ (Fig. 5.3). During slab buckling, the slab dip in the top ∼300 km alternates between steep (vertical or overturned) and inclined, and our results illustrate that this induces alternating phases of slab rollback and stagnation (or advance), as well as motion of the trench and upper plate (Fig. 5.5 a). Our results reveal that these alternating phases of forward and backward buckling induce variations in subduction rate and subducting plate motion.

High subduction rates occur in our experiments when the slab buckles backward, towards the downgoing plate and adjacent to a previous slab fold. For backward buckling, the accommodation space in the MTZ in which the buckling slab can sink is available as opposed to forward buckling, in which case the lower part of the MTZ is still occupied by previously buckled slab (Fig. 5.4 a). As the 410 km phase transition enhances the negative buoyancy of slabs and thus enhances slab pull [Čížková and Bina, 2013] the accommodation in the MTZ for backward

buckling allows the slab to force a short (in our reference model < 3 Ma) pulse of high V_{SP}, and roll-back. During roll-back, the slab steepens to a vertical orientation accompanied by limited motion of the trench (Fig. 5.4 b), or even trench advance if the upper plate rheology would allow it. Once the slab overturns the next forward buckle initiates, during which time MTZ accommodation space decreases. A forward buckle is associated with trench retreat and slab advance in the MTZ, seemingly rotating over a pivot point in the upper mantle (Fig. 5.4a). As a result, V_{SP} decreases during a forward buckling slab while V_{UP} increases. As the slab flattens during this forward buckle it creates accommodation space for the next backward buckle and associated acceleration (Fig. 5.4 b). Furthermore, such slab-folding in the MTZ generates variations in strain-rate in the slab itself which correlate to the occurrence of deep-seismicity in natural subduction zones [Billen, 2020]. The slab-morphologies at varying stages of buckling in our models (Figure 5.4) may explain the natural slab-dip variations of present-day subduction zones.

V_{SP} variations in models with a forced stationary trench are smaller because the slab has less variation in the amount of accommodation space in the MTZ. Trench-stationary subduction causes the slab buckling in a vertical column (Fig. 5.3 i-n). Basically, the rate and amplitude of plate motion oscillation primarily depends on the average V_{SP}: the higher, the bigger the space accommodation problem for slab folds in the MTZ. Our experiments with a moving trench and an average V_{SP} of 6 cm/a, i.e., the global average plate velocity [Meer et al., 2014], reveal rapid oscillations (< 10 Ma periods) with large V_{SP} fluctuations (3-13 cm/a) (Fig. 5.6). Our slab buckling models have shorter periods and larger amplitudes than obtained in previous studies with variations in subduction velocity as a result from slab buckling and eventual slab transfer into the lower mantle [Schellart et al., 2007, Gibert et al., 2012, Čížková and Bina, 2013, Billen and Arredondo, 2018, Briaud et al., 2020, Cerpa et al., 2022]. Those previous investigations showed velocity variations of a subducting plate with periods between 15 and 30 Ma owing to smaller subduction plate velocities compared to our models, emphasising the V_{SP} dependency of the oscillations. The trench motion in our models is controlled by the shape of the slab and therefore the interaction between the slab and the MTZ. Imposing a weak asthenospheric layer (WAL) increases subduction rate and decreases trench motion, allowing for a similar lower mantle slab-structure as in our models, especially for young oceanic lithosphere [Cerpa et al., 2022]. Therefore, adding a weak asthenospheric layer may increase the subduction rates in our models and even further shorten the period of oscillations while increasing the amplitudes.

The rapid subducting plate motion oscillations that we find in our experiments have similar periods to those recently observed in the high-resolution (0.5-1 Ma) reconstruction of marine magnetic anomalies of the Indian Ocean [DeMets and Merkouriev, 2021]. Previous plate reconstructions using stage rotations based on larger stage intervals of 5-10 Ma (Fig. 5.1) [van Hinsbergen et al., 2011, Müller et al., 2019] smoothed out such rapid plate motion changes [White and Lister, 2012, Espinoza and Iaffaldano, 2023]. We illustrate this by sampling V_{SP} in our reference experiment with a mobile upper plate: when we sample on a 1-2 Ma

resolution, similar to DeMets and Merkouriev [2021] we resolve rapid (< 5 Ma) peaks in plate motion caused by slab buckling (Fig. 5.9 a). However, sampling our V_{SP} curves at larger, typically used intervals of 5 or 10 Ma generates the smooth plate motion history that is widely inferred from plate reconstructions (Fig. 5.9 b,c).

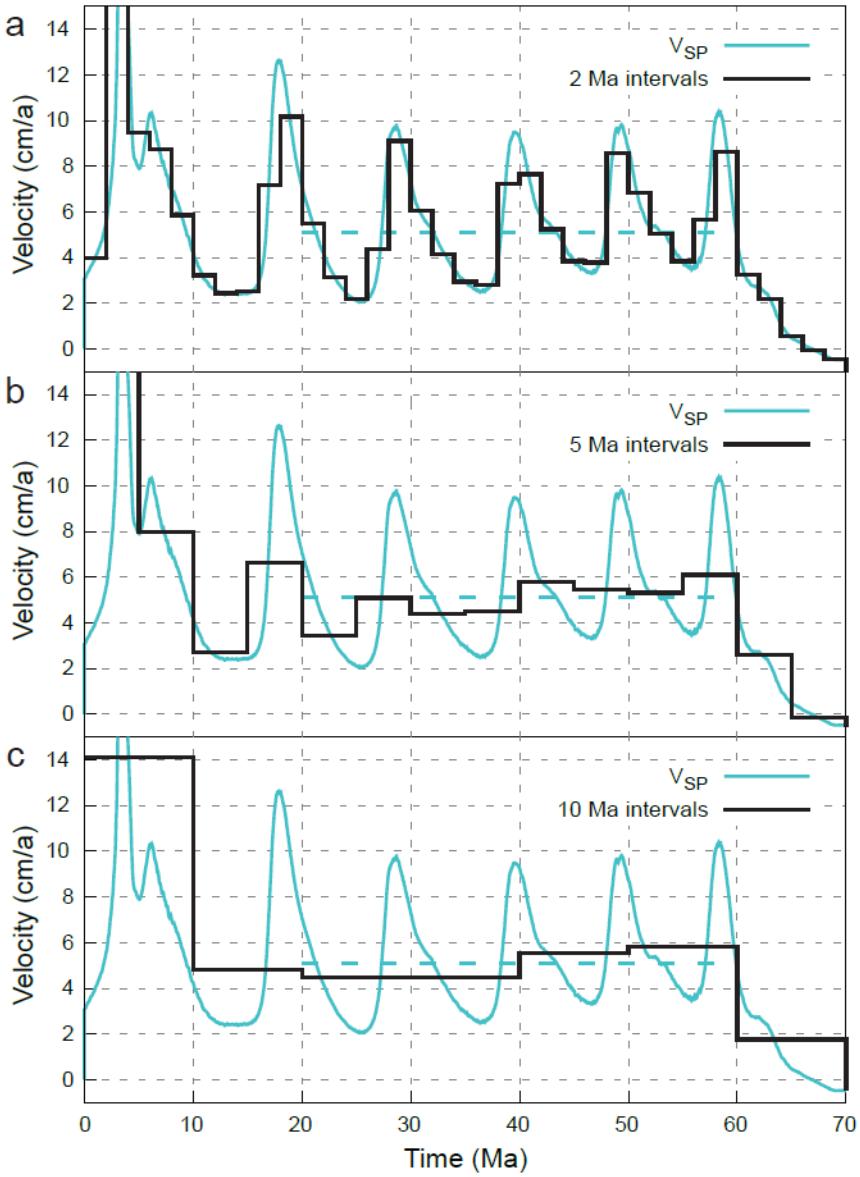

Figure 5.9: Horizontal subducting plate motion for the reference model with roll-back and stage velocities if sampled at 2, 5 or 10 Ma intervals.

The average V_{SP} as well as the amplitudes of the plate motion oscillations for the case of India are higher than in our experiments. However, a further increase in V_{SP} in our models would probably result in shorter periods and larger amplitudes of oscillation (Figure 5.7). The differences between the Indian Plate velocities and our models may be explained by the necessary simplified nature of our models: the absolute plate motion rate of India may have been much higher than we obtained in our experiments because the Indian plate may have been lubricated at the base by a mantle plume [Kumar et al., 2007, van Hinsbergen

et al., 2011], or the subduction interface may have been lubricated by sediments [Behr and Becker, 2018]. The two dimensionality of our models is also unable to characterise the lateral variations in subduction rate of the Indian Plate [van Hinsbergen et al., 2011] which may affect the buckling behaviour. Furthermore, the lithosphere in the MTZ during the 55-50 Ma ago interval during which the oscillations were reconstructed may at least partly have been of continental origin [van Hinsbergen et al., 2019]. This could have influenced the slab pull, the rate of slab transfer into the lower mantle, and the amount of accommodation space in the MTZ, which would all influence the oscillation V_{SP} amplitude and period in our experiments.

An additional difference with our simplified experiments is that subduction of the Indian plate occurred at a trench that was not retreating, as in our experiments, but instead slowly moving northwards, i.e. advancing [van Hinsbergen et al., 2019]. In our experiments, subduction at a mantle-stationary trench occurs with lower amplitude oscillations than those reconstructed by DeMets and Merkouriev [2021]. However, the Indian slab may have advanced below the upper plate creating a flat lying slab [van Hinsbergen et al., 2019] in which case buckles may form at varying locations below the upper plate which may hamper the effect buckling has on trench motion. Slab buckling combined with trench advance could create an opposite regime as in our experiments, with acceleration during forward buckles and vice versa, as in this case the mantle below the upper plate would have more accommodation space than below the subducting plate. Imposing a thicker or stiffer overriding plate may make a trench more susceptible to advance [Sharples et al., 2014] while slab buckling may then cause the trench to alternate between retreat and advance [Stegman et al., 2010]. We foresee that buckling may produce variations in slab morphology and large variations in subduction rate also when the trench is nearly stationary [Cerpa et al., 2022]. With higher subduction rates for India than we reproduced in our experiments, slab buckling must intensify allowing a trench to also advance (besides retreating) which may explain the $\sim$ 1000 km wide north to south tomographic anomaly widely interpreted as the Indian slab [Qayyum et al., 2022] of which we consider its large buckling the plausible and viable candidate to explain the reconstructed Indian Plate velocity oscillations.

In our slab-pull-driven subduction models with a freely moving upper plate we also observe oscillating motion of the trench and upper plate [Royden and Husson, 2006]. In our simple experiments, the rigid upper plate is not able to deform, and it thus moves along with the trench where naturally this would lead to changes in stress state, reflected by episodic back-arc spreading [Clark et al., 2008, Ishii and Wallis, 2022], extensional or contractional upper plate deformation [Capitanio et al., 2010, Lee and King, 2011, Billen and Arredondo, 2018, Cerpa et al., 2018, Boutoux et al., 2021, Dasgupta et al., 2021, van Hinsbergen et al., 2021, Pons et al., 2022] and even changes in topography [Briaud et al., 2020]. Such variations may be of interest to the understanding of fluid and magmatic processes affecting the upper plate. For instance, episodic magmatic ponding alternating with migration and flare ups [Chapman et al., 2021], and episodic mineralization [Chelle-Michou et al., 2015] and associated pulses in the formation of ore deposits

[Wilson et al., 2020] may be the result of such stress state oscillations. Therefore, for subduction zones where slab buckling leads to oscillating trench motion and upper plate deformation, enhanced resolution in marine magnetic anomalies and accompanying reconstructions could lead to a better predictive power in the timing of these magmatic and ore-genesis related upper plate processes. In the Andes, alternations on a timescale of ∼10 Ma between shortening and trench retreat were recently postulated to result from slab buckling [Pons et al., 2022]. For Tibet, the only high-resolution deformation records in the relevant time interval of 60-50 Ma ago are from the Qiangtang terrane of northern Tibet, far from the trench [Li et al., 2020a,b], which on a first order appear to record shortening pulses that coincide with the oscillations [DeMets and Merkouriev, 2021]. More high-resolution work, for instance in the Xigaze forearc basin, could reveal whether the upper plate may also have recorded short intervals of extension.

Would all subducting plates then show these oscillating plate motions? Higher-resolution tectonic reconstructions could provide the answer, but we see several reasons why not all ridges that border subducting plates may record such oscillations similarly. The process of buckling at long subduction zones might not occur synchronously along the entire trench. Such a process may explain the oscillating azimuth of India-Asia convergence during the documented oscillations [DeMets and Merkouriev, 2021]. In addition, subduction rate may vary gradually along-strike of a trench (e.g., the west Pacific subduction zones from New Zealand to Kamchatka), and rapidly across triple junctions [e.g. van de Lagemaat et al., 2018, Vaes et al., 2019]. Plates like the modern Pacific plate would be less susceptible to the effect of slab buckling in the MTZ, even if the oscillations in a 2D system likely occur. We foresee that oscillations in plate motion are best visible for plates where subduction zones are oriented sub-parallel to spreading ridges and sub-perpendicular to the plate motion direction. Possible candidates for the Cenozoic besides the Indian plate are the Nazca plate [Pons et al., 2022], the Juan de Fuca plate, the Cocos plate, or the Aluk plate [van de Lagemaat et al., 2023] and for earlier times perhaps the Farallon or Kula plates. We consider these targets for high-resolution magnetic anomaly reconstruction to further test the possibilities of slab buckling and the opportunities it may apply to understand mantle and lithosphere dynamics and magmatic and economic geology.

Finally, our models show that the rapid oscillations shown by DeMets and Merkouriev [2021] may well be explained by buckling of the subducting slab that results from the accommodation space problem caused by the much lower sinking rates of slabs in the lower mantle. This implies that plate motions that exceed lower mantle slab sinking rates, so larger than 1-1.5 cm/a [van der Meer et al., 2010, Butterworth et al., 2014, van der Meer et al., 2018], are resisted from the transition zone downwards. In other words, typical plate motions must be primarily driven in the top few hundred kilometers of the mantle. The 410 km phase transition still enhances slab pull, but at the 660 discontinuity the slab encounters resistance and thickens. In addition, the top 100 km of the Earth also resists plate motion due to friction on the subduction interface or drag resistance from the underlying mantle, therefore plate tectonics must primarily be driven between depths of ∼100 and 500 km, or only 6-7% of the Earth's radius. This

is a remarkably small niche that on Earth apparently has the right conditions for plate tectonics. We foresee that understanding the dynamics of this narrow zone throughout Earth's history holds the key to understand the uniqueness of our planet to start and sustain plate tectonics.

6. The influence of water on crustal rheology: implications for subduction dynamics

6.1 Introduction

In numerical models of subduction, slab deformation critically depends on the characteristics of decoupling of the subducting and overriding plates. In chapter 3 we discussed the effects of the parametrization of a weak decoupling crust and concluded that it has primary effects on slab behavior. Here we will complement these results by discussing further the nature of this weakening, namely the effect of bound water on the crustal viscosity. Water bound in minerals reduces the density and viscosity of the crust and mantle and thus has a considerable impact on the subduction dynamics [e.g. Arcay et al., 2005, Nakao et al., 2016, 2018]. In nature, crustal material deforms non-linearly, which results in a positive feedback between subduction velocity and crustal viscosity, as discussed in chapter 3. However, since the detailed description of the complex crustal rheological structure in subduction models on a larger scale is demanding, a decoupling crust of constant viscosity is often used. [e.g. Běhounková and Čížková, 2008, Chertova et al., 2012, Androvičová et al., 2013, Goes et al., 2017, Pokorný et al., 2021].

The low viscosity of this decoupling layer is associated with the presence of water, therefore, the magnitude of viscosity and depth extent of this weak layer are affected by material (de)hydration. In this chapter we focus on models where uniform crustal viscosity is moderated by the presence of water. The amount of bound water present in the crustal material changes according to the saturation diagram (see Fig. 2.2). The bound water content reduces the viscosity of the crustal material as

$$\eta_{crust} = \eta_{const} * f_w(w_b). \tag{6.1}$$

Here η_{const} is the crustal background viscosity and $f_w(w_b)$ is the bound water prefactor function defining the viscosity contrast of dry and wet material (see eq. 2.20). In some of the models, water also influences the diffusion and dislocation creep viscosity of mantle material; the viscosity of these mechanisms follows eq. (2.17) and (2.18). We also present here three models where water influences density, in addition to rheology, following eq. (2.24).

6.2 Description of the model

The model setup is based on dry models presented in chapter 3 (Fig. 6.1). The 2D Cartesian model domain is 10 000 km wide and 2000 km deep. The age of the subducting and overriding plates is 100 Ma at the trench. We include the main mantle phase transitions at 410 km and 660 km with Clapeyron slopes of 2 MPa/K and -2.5 MPa/K, respectively. The crustal decoupling layer is 10 km thick. For numerical convenience at 10 GPa ($\sim$ 300 km), where crustal material

is already dry and the decoupling effect of the crust is no longer necessary, the rheology of the crust is replaced by the mantle rheology. Thermal expansivity is depth dependent with $3 \times 10^{-5} K^{-1}$ at the surface and reaching $1.2 \times 10^{-5} K^{-1}$ at a depth of 2000 km [Hansen et al., 1993, Katsura et al., 2009]. Thermal diffusivity is constant at $10^{-6} m^2 s^{-1}$. An impermeable free slip is prescribed on all boundaries.

Initially, only the crustal material is saturated with 6 wt% of water typical for basalt [Schmidt and Poli, 1998, Iwamori, 2004, 2007] (Fig. 6.1 b). Crustal material viscosity follows eq. (6.1). Background viscosity of dry crust η_{crust} is 10^{21}Pa s and crustal viscosity contrast parameter f_{m_c}, as applied in eq. (2.20), varies among different models within the range of $0.1 - 0.5$. In the mantle material, we employ effective viscosity (eq. 2.12) [van den Berg et al., 1993] that combines diffusion creep, dislocation creep, and a power-law stress limiter. In models where water also reduces the viscosity of the mantle material, the viscosity of diffusion and dislocation creep follow eq. (2.17) and (2.18) and viscosity contrast parameter f_{m_m} is also in range of $0.1 - 0.5$. In the lower mantle, we use only dry diffusion creep [Čížková et al., 2012]. Individual parameters are specified in Table 6.1. Maximum bound water content follows phase saturation diagrams for the crust (Fig. 2.2) and mantle (Fig. 2.3) as presented in section 2.5.

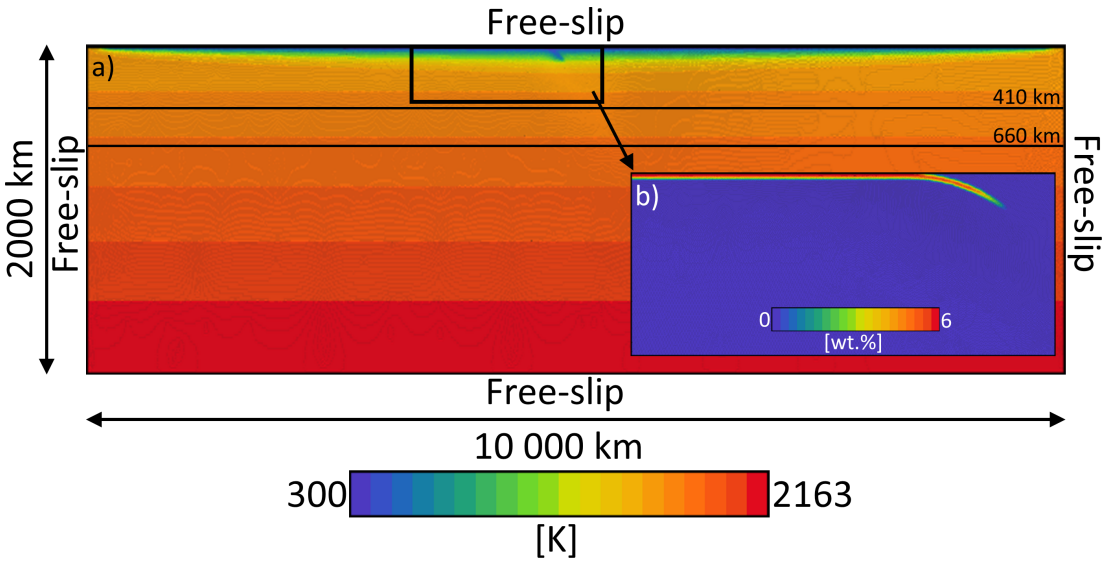

Figure 6.1: Model setup. Initial temperature (a), and initial bound water distribution (b). The model domain is 2000 km deep and 10 000 km wide. At all boundaries, an impermeable free slip is prescribed. Initially, only crustal material is saturated with 6 wt% of H_2O.

Table 6.1
Model parameters

symbol	Meaning	Value	Units
Water parameters			
$w_{b_{ref}}$	reference water content[a]	6.2×10^{-4}	–
f_{m_c}	viscosity contrast between wet and dry crust [a]	$0.1 - 0.5$	–
f_{m_m}	viscosity contrast between wet and dry mantle [a]	$0.3 - 0.5$	–
β	water density coefficient [b]	1	–
u_{f_w}	free water migration velocity	1000	cm/a
Upper mantle rheology			
A_{diff}	Pre-exponential parameter of diffusion creep[c]	1×10^{-9}	$Pa^{-1}\ s^{-1}$
A_{disl}	Pre-exponential parameter of dislocation creep[c]	31.5×10^{-18}	$Pa^{-n}\ s^{-1}$
E_{diff}	Activation energy of diffusion creep[c]	3.35×10^{5}	$J\ mol^{-1}$
E_{disl}	Activation energy of dislocation creep[c]	4.8×10^{5}	$J\ mol^{-1}$
V_{diff}	Activation volume of diffusion creep[c]	4.0×10^{-6}	$m^3\ mol^{-1}$
V_{disl}	Activation volume of dislocation creep[c]	11×10^{-6}	$m^3\ mol^{-1}$
n	dislocation creep exponent	3.5	–
$\dot{\epsilon}_y$	Reference strain rate	1×10^{-15}	s^{-1}
σ_y	Stress limit	2×10^{8}	Pa
n_y	Stress limit exponent	10	–
Lower mantle rheology			
A_{diff}	Pre-exponential parameter of diffusion creep	1.3×10^{-16}	$Pa^{-1}\ s^{-1}$
E_{diff}	Activation energy of diffusion creep[d]	2×10^{5}	$J\ mol^{-1}$
V_{diff}	Activation volume of diffusion creep[d]	1.1×10^{-6}	$m^3\ mol^{-1}$
Other model parameters			
R	Gas constant	8.314	$J\ K^{-1}\ mol^{-1}$
κ	Thermal diffusivity	10^{-6}	$m^2\ s^{-1}$
g	Gravitational acceleration	9.8	$m^2\ s^{-2}$
ρ_0	Reference density	3416	$kg\ m^{-3}$
c_p	Specific heat	1250	$J\ kg^{-1}\ K^{-1}$
α_0	Surface thermal expansivity	3×10^{-5}	K^{-1}
γ_{410}	Clapeyron slope of 410 km phase transition[e]	2×10^{6}	$Pa\ K^{-1}$
γ_{660}	Clapeyron slope of 660 km phase transition[e]	-2.5×10^{6}	$Pa\ K^{-1}$
$\delta_{\rho 410}$	Density contrast of 410 km phase transition[f]	273	$kg\ m^{-3}$
$\delta_{\rho 660}$	Density contrast of 660 km phase transition[f]	341	$kg\ m^{-3}$

[a] Arcay et al. [2005]
[a] Nakao et al. [2016]
[c] Parameters of wet olivine based on Hirth and Kohlstedt [2003b]
[d] Čížková et al. [2012].
[e] Bina and Helffrich [1994].
[f] Steinbach and Yuen [1995].

6.3 Results

6.3.1 Evolution of the reference model

Let us first describe the model where only crustal viscosity is influenced by water (Fig. 6.2). The viscosity contrast between wet and dry material of the crust is $f_{m_c} = 0.3$. Density does not depend on water content. We consider this model a reference for the other models discussed in this chapter. At $\sim$ 10 Ma (Fig 6.2 a) the tip of the slab reaches a depth of $\sim$ 150 km. Until $\sim$ 15 Ma storage capacity of crust is high enough and no dehydration occurs. At $\sim$ 15 Ma PT conditions in the slab tip result in bound water exceeding the water saturation capacity and water from crust hydrates thin overlying layer. Water released

from the downgoing crust is propagating upwards and hydrating the overlying mantle wedge and the overriding plate (Fig. 6.2). The water transport is further illustrated in Figure 6.3, where integrated water content is shown as a function of time. Red, green and blue curves represent the amount of bound water, free water and water outflux from the model domain, respectively. Until $t \sim 20$ Ma the curves remain constant because the water that dehydrated from the crust, hydrated the mantle wedge or the overriding plate within the same time step. After 20 Ma, water that was saturating the overriding plate, reaches the top boundary and starts to outflux from the model (see white arrow in Fig. 6.2 m) as can be observed in Fig. 6.3, where blue (out flux) and red (bound water) curves have opposing slopes. At 30 Ma, the slab tip lies horizontally at the boundary between the transition zone and the lower mantle at 660 km depth, and the first buckle starts to form (see Fig. 6.2 d). At 50 Ma, the slab is horizontally buckling at the base of the transition zone at 660 km depth (see Fig. 6.2 e). Note that the thin hydrated layer of mantle material overlying the subducting crust is dragged by the slab to the transition zone (Fig. 6.2 n,o). The fact that we can drag water to such depths, may have important implications for the nucleation of deep earthquakes as well as for the possible water reservoirs in the upper mantle and the transition zone [e.g. Hirschmann, 2006, Faccenda, 2014].

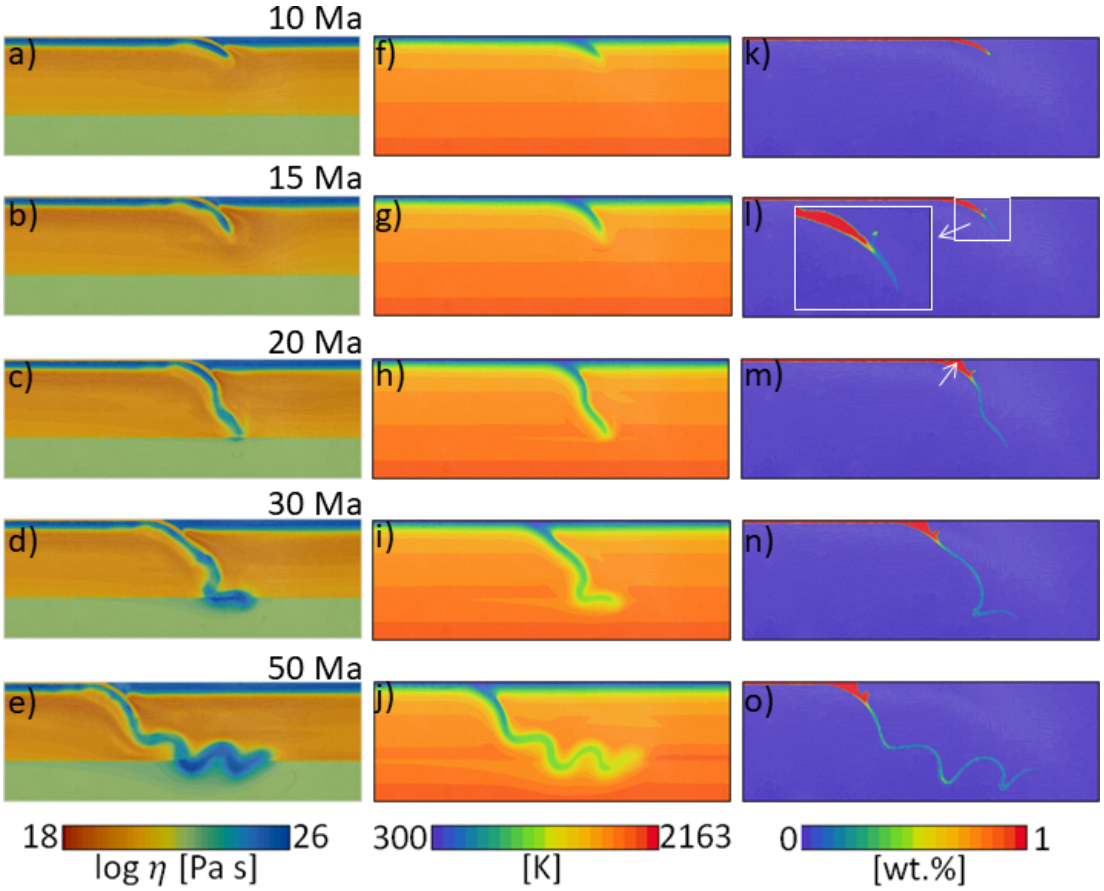

Figure 6.2: Zoomed-in snapshots of viscosity (3000x1000 km) (a-e), temperature (3000x1000 km) (f-j) and weight fraction of bound water (2400x800 km) (k-o) of the model in which water influences the rheology of the crustal material with $f_{m_c} = 0.3$.

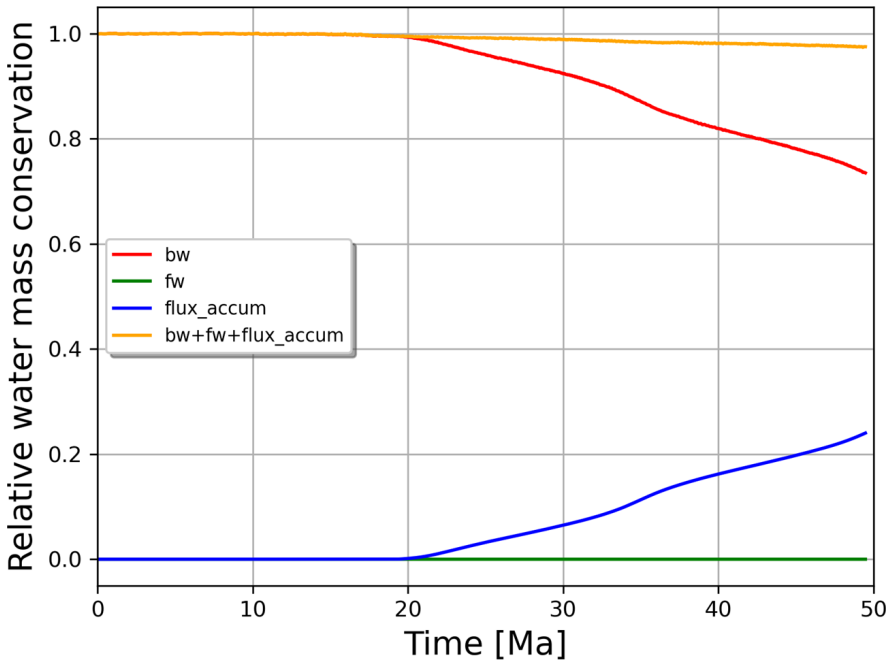

Figure 6.3: Time evolution of the integrated water content in the reference model (water mass at the time t divided by water mass at the beginning of the simulation). The red curve is for bound water, the green curve is for free water, the blue curve is for accumulated flux through the top boundary, and the yellow curve is a sum of bound water, free water, and accumulated flux through the top boundary.

6.3.2 Comparison of the dry and wet models

To illustrate the implications of the dry and wet rheology, we executed 9 models with varying parameters that control water dependent viscosity of crust and mantle. In Fig. 6.4 we ilustrate each of these models by one snapshot taken at 40 Ma. Three of them are dry, employing constant viscosity of the crust (Fig. 6.4 g-i). The rest of the models (Fig. 6.4 a-f) have water dependent viscosity. In models WC0.1 - WC0.5 (6.4 a-c), water only influences crustal rheology, models WC0.3_M0.1 - WC0.3_M0.5 (6.4 d-f) have in addition mantle material weakened by water.

The dry models differ only in the value of constant viscosity of the crust of 10^{20}, 2.5×10^{20} and 5×10^{20} Pa s (Fig. 6.4 g-i). Their behavior is similar to models described in detail in section 3.4.1. At t=40 Ma, model Dry10^{20} with a weak crust is horizontally buckling at the base of the transition zone, while the trench is rolling back. On the other hand, the slab in the model Dry5×10^{20} with a strong crust is much slower (cf. plate velocities in Fig. 6.5). The trench rollback is limited in this case.

Now, we will consider models where only the crust is initially saturated with water. Water in these models affects only the viscosity of the crust. In models WC0.1 - WC0.5 (6.4 a-c) the background viscosity of the dry crust of 10^{21} Pa s is reduced by water, with the viscosity contrasts between wet and dry material of $f_{m_c} = 0.1$, $f_{m_c} = 0.3$ and $f_{m_c} = 0.5$, respectively. Model WC0.1 (6.4 a) with the viscosity reduction factor $f_{m_c} = 0.1$ has effective crustal viscosity of approx-

imately 10^{20} Pa s for the fully saturated crust and thus its decoupling efficiency is essentially the same as in the dry model Fig. 6.4 g. Similarly, behaviour of models WC0.3 and WC0.5, is close to the behavior of models Dry2.5×10^{20} and Dry5×10^{20}. Following the saturation diagram (Fig. 2.2) crust in models WC0.1 and WC0.5 dehydrates at $\sim$ 230 km. At that depth crustal viscosity reaches 10^{21} Pa s (dry crust viscosity). Yet somewhat deeper, at 300 km, the crustal material is repleaced by mantle material for numerical convenience. As we can see from the comparison of the models with dry and wet crust, this process of dehydration of the crustal material and associated stiffening of the crust play a minor role in the subduction dynamics. In general, wet models correspond to dry models in cases where chosen f_{m_c} results in comparable crustal viscosities.

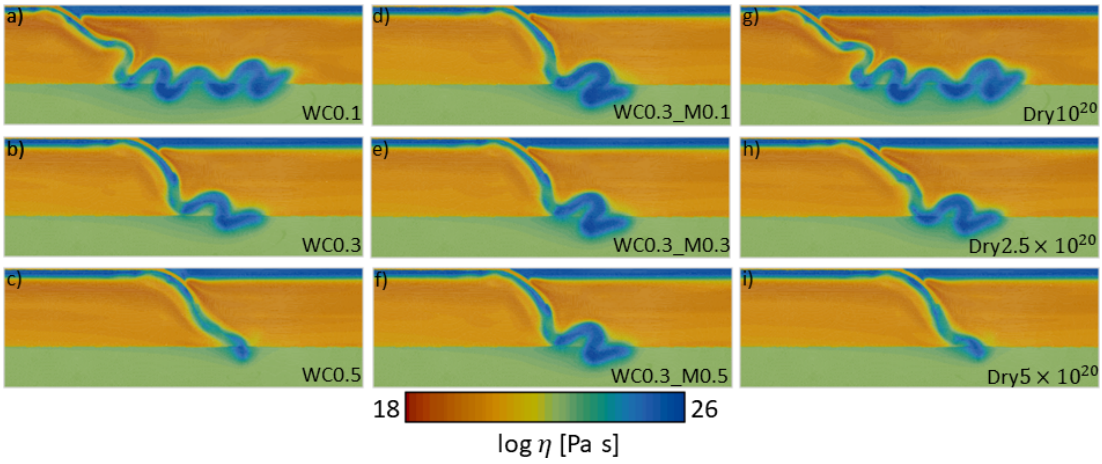

Figure 6.4: Zoomed-in (3000x1000 km) snapshots of viscosity taken at t=40 Ma. Models a-f have background constant crustal viscosity of 10^{21} *Pa s and initially prescribed water in the crustal material. In models a-c water only influences the rheology of the crustal material with* $f_{m_c} = 0.1, 0.3$ *and* 0.5*, respectively. In models d-f water influences the rheology of the crustal material with* $f_{m_c} = 0.3$ *and mantle material with* $f_{m_m} = 0.1, 0.3$ *and* 0.5*, respectively. Finally, models g-i are dry with constant crustal viscosity of* 10^{20} *Pa s,* 2.5×10^{20} *Pa s and* 5×10^{20} *Pa s, respectively*

In the next step, we assume that water reduces viscosity of both crustal and mantle material. Thus water released from the crust hydrates the mantle wedge and lowers the viscosity of the contact between the subducting slab and the mantle material above the slab. Models WC0.3_M0.1, WC0.3_M0.3 and WC0.3_M0.5 (Fig. 6.4 d-f) have the viscosity contrast between wet and dry crustal material fixed with value of $f_{m_c} = 0.3$. The diffusion and dislocation creep of the mantle material influenced by water follows eq. (2.17) and (2.18) and the viscosity contrast of the wet mantle material f_{m_m} is $0.1, 0.3$ and 0.5, respectively.

In model WC0.3_M0.1 where mantle wedge viscosity is reduced by a factor of $\sim$1.8 for fully saturated material (Fig. 6.4 d) at t=40 Ma slab is buckling at the base of the transition zone. The decreased viscous coupling between the slab and the wet mantle wedge accelerates the slab and thus the buckles are tight and the slab is slowly penetrating into the lower mantle. Model WC0.3_M0.5, with lower

viscosity reduction of the mantle material in comparison to model WC0.3_M0.1 (factor ∼1.2), shows very similar behavior. But because the mantle material just above the slab is not as weakened as in the case of the model WC0.3_M0.1, the average subduction velocity is lower (see Fig. 6.5), rollback is stronger and thus the buckles are not as tight as in case of the model WC0.3_M0.1. In general, water reducing viscosity of the mantle wedge affects the behavior of subduction. It increases plate velocity and results in more tight buckles. However, in the tested range of parameters, the differences in slab deformation are not large.

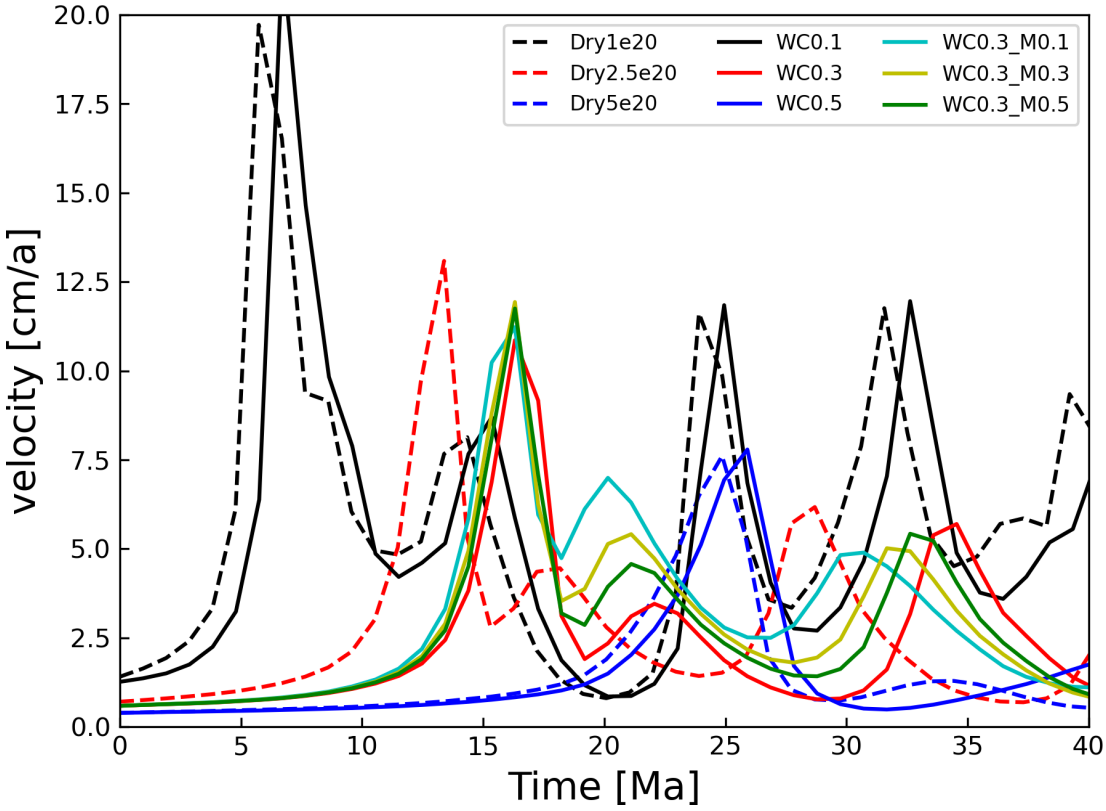

Figure 6.5: Time evolution of the subducting plate velocity of the models shown in Fig. 6.4. Dashed lines show dry models, solid lines are for models with water dependent rheology.

Figure 6.6 shows PT - paths of the tip of the model slabs WC0.1 and WC0.5 overplotted on saturation diagrams for crustal (a) and mantle (b) material. Dots on the PT - paths represent output time steps (plotted each ∼ 1 Ma). We can observe that, despite the differences in subduction velocity (black and blue lines in Fig. 6.5), deformation in the transition zone, and the overall subduction dynamics that the slabs are experiencing, the models do not differ much. We can however note that they follow different dehydration reactions in depth range of ∼ 150 - 200 km, where faster slab of model WC0.1 goes through the stability field of phase A, serpentine, garnet and clinopyroxyne, while slower slab of model WC0.5 goes through the stability field of olivine, orthopyroxene, Mg-sursassite and clinopyroxene.

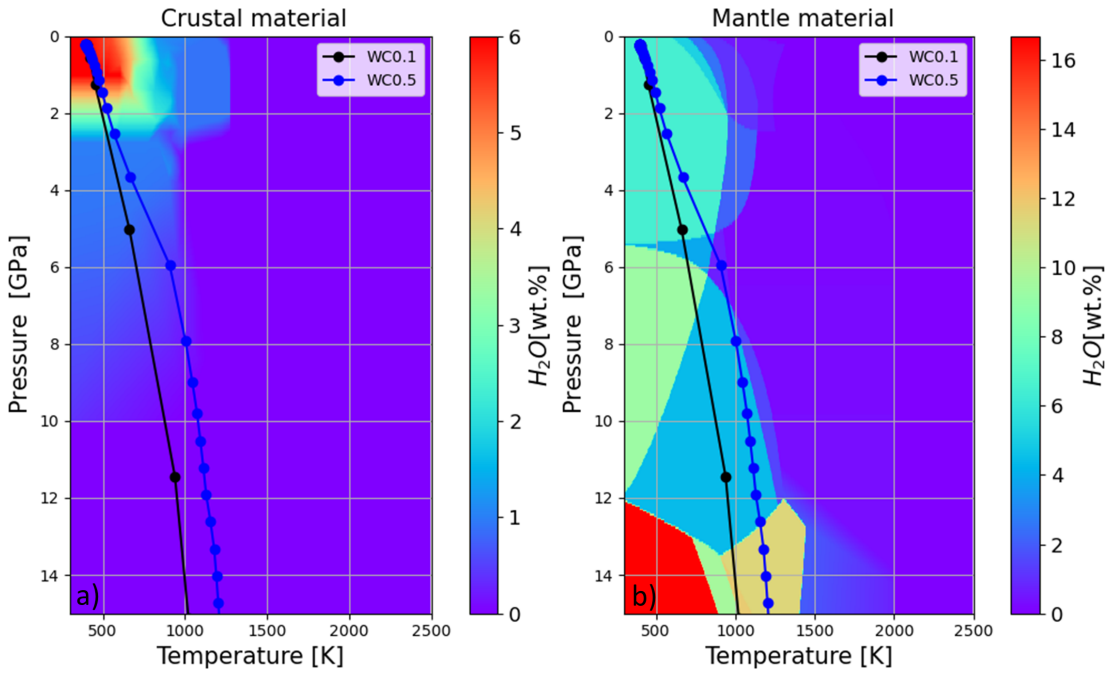

Figure 6.6: PT - paths of tracers close to the slab tip overplotted with saturation H_2O diagram for crustal (a) and mantle (b) material [Iwamori, 2004, 2007]. Black line is for model WC0.1 and black line for model WC0.5

6.3.3 Models with water density reduction

Finally, let us assume that water not only influences the rheology of the crustal and mantle material, but also reduces its density. The density reduction follows eq. (2.24). In Fig. 6.7 a-c we show three models with $f_{m_c} = f_{m_m} = 0.3$ (this corresponds to model WC0.3_M0.3 in Fig. 6.4 e) and with the water density coefficients β of 0.5, 1.0 and 1.5, respectively. Slab morphology in model WC0.3_M0.3_EOS0.5 with a mild density reduction in the water saturated material shown in Fig. 6.7 a is not strikingly different from model WC0.3_0.3 (Fig. 6.4 e), yet the second buckle is apparently less tight thanks to lower plate velocity caused by more buoyant crust (Fig. 6.7 d). With increasing β, meaning higher density reduction and thus increased buoyancy of the slab (Fig. 6.7 b-c), plate velocity further decreases (see Fig. 6.7 d). Thus, density reduction by water has opposite effect on the slab velocity than rheological weakening.

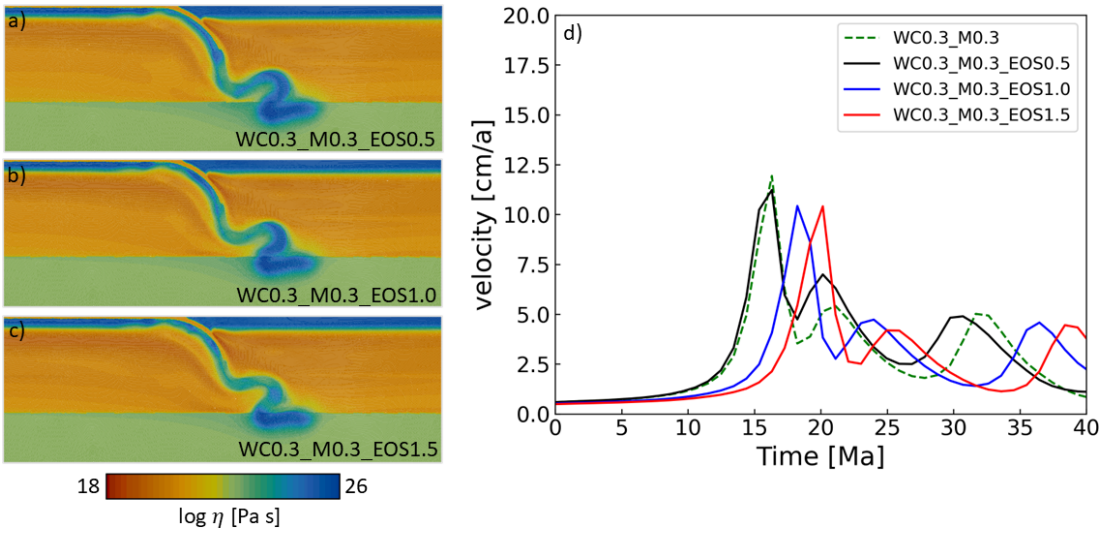

Figure 6.7: a-c) Zoomed-in (3000x1000 km) snapshots of viscosity taken at t=40 Ma. All models have background constant crustal viscosity of 10^{21} *Pa s and reduction by factor* $f_{mc} = f_{mm} = 0.3$ *for both crust and mantle. Models differ in the water density coefficient* β*. a)* $\beta = 0.5$*, b)* $\beta = 1.0$*, c)* $\beta = 1.5$*. d) Time evolution of the subducting plate velocity of the models in panels a-c. The Green dashed line represents model WC0.3_M0.3 and serves as a reference.*

6.4 Conclusion

We have shown that variations of material properties due to water in crust and mantle wedge affect the subduction dynamics and that only a small change in the viscosity contrast between wet and dry crustal material considerably changes the plate velocity. The comparison of wet (Fig. 6.4 a-c) and dry (Fig. 6.4 g-i) models suggests that the effect of water on crustal material may be mimicked by lowering the constant crustal viscosity in dry models at depths above $\sim$ 150 km and assuming viscosity increase at about the depth where crustal material dehydrates by eclogitization. Such dry models could however not account for water induced weakening of mantle wedge. The models that consistently include water transport are therefore necessary to investigate, e.g. the water budget in the transition zone [e.g. Nakagawa and Iwamori, 2019] or the role played by water in the nucleation of the deep earthquakes [e.g. Zhan, 2020].

A. Lid-driven convection models with water transport

This appendix illustrates the mechanism of water transport in simple kinematic models. These models do not include heat transport. The flow is the models is driven by specified horizontal velocity at the top boundary (therefore, models are referred to as "lid-driven").

A.1 Description of the model

The lid-driven convection model is 2D square box 1000 km wide and 1000 km deep. Model domain is discretized using 100×100 quadratic triangular elements. The background grid resolution is 100×100 equidistant grid cells. On all boundaries we prescribe an impermeable free-slip except for the top boundary, where a constant horizontal velocity is prescribed. Initially, 100 tracers are randomly distributed within each grid cell. Here we solve only equations (2.1) and (2.3) for the viscous flow, assuming constant viscosity. We test three values of surface velocity, 3, 5 and 7 cm/a. We also tested three values of free water migration velocity of 50, 100 and 200 cm/a. Model contains top 100 km thick layer of initially wet material with 2 wt% of water (material 1) and a background material (material 2) that is initially dry (see red and blue area in Fig. A.1 b). These two materials share the same 2-layered (pressure dependent) saturation diagram. In the upper 500 km both materials are able to carry 2 wt% of bound water. In the lower half of the model domain, the allowed water saturation is set to 0 wt%, meaning that when the wet material crosses the middle of the model domain, all bound water must be released and transported upwards.

A.2 Results

Let us now first describe the behaviour of the reference model (Fig. A.1) with lid velocity of 5 cm/a and the free water migration velocity of 100 cm/a. Prescribed velocity on the top boundary induces clockwise single cell motion within model domain. This flow field carries hydrated material 1 (red stripe in Fig. A.1 b). Material that crosses the dehydration front at a mid-depth of the model domain has to release all bound water, i.e. no bound water can be present in the lower half of the model (Fig. A.1 c). Released water then follows the free water migration scheme (section 2.4). Free water is allowed to ascend only the distance given by the integration time step multiplied by free water migration velocity (100 cm/a in this reference model). In case the tracers in the respective background cell are fully saturated (i.e. there is no available capacity for bounding more water) this water appears as a free water (see Fig. A.1 d at t=31.70 Ma). The free water appears in discrete stripes. The distance of individual stripes is given by the integration time step and the value of the prescribed free water migration velocity. When the initially wet material 1 sinks below the dehydration front and the unsaturated material 2 is in path of the percolating free water, this water

then saturates the dry material. This can be observed in figure A.1 b and c at t=63.400 Ma when all initially wet material 1 has already passed the mid-depth of the model domain, but bound water is present only above the dehydration front.

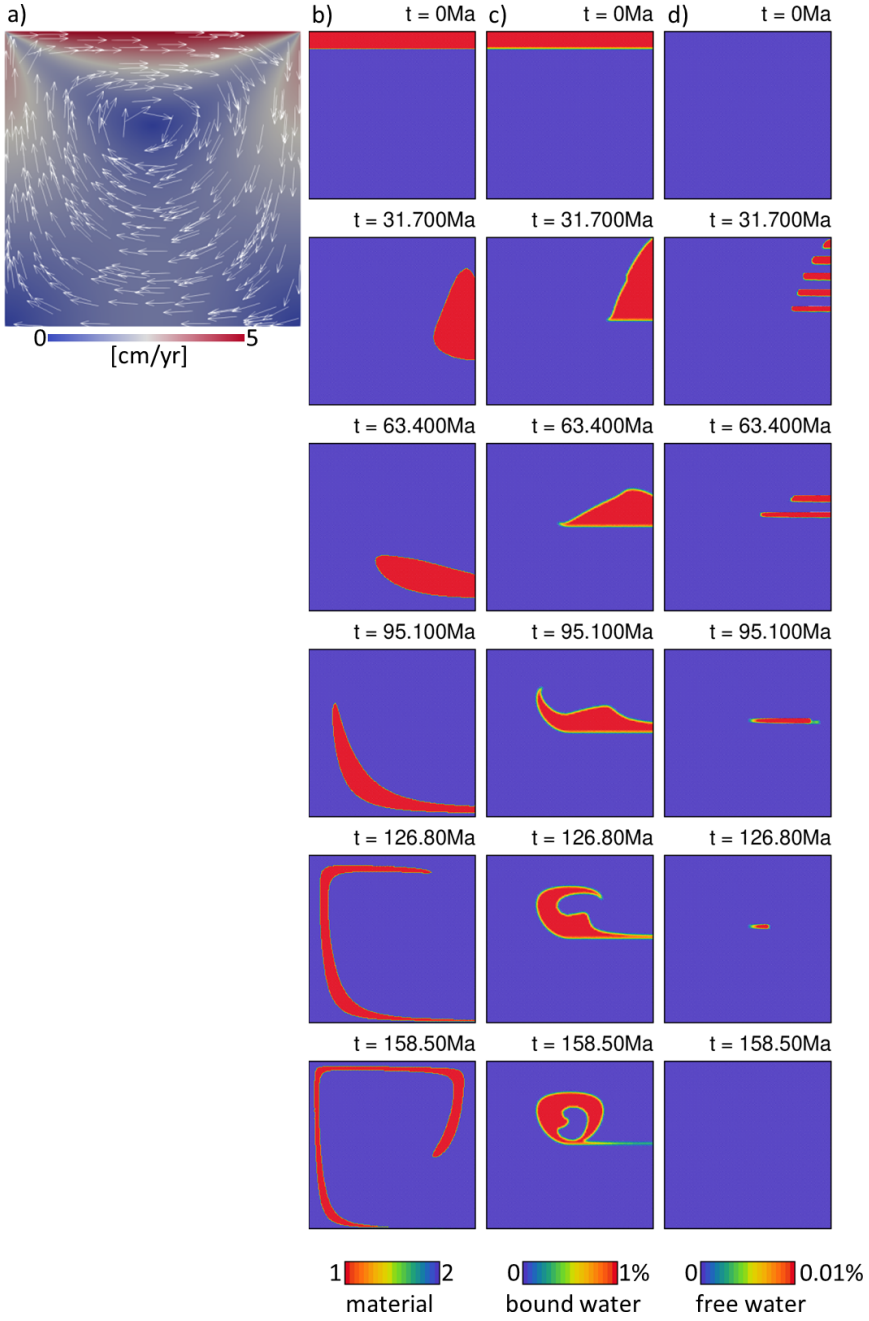

Figure A.1: The time evolution of the model with lid velocity 5 cm/a and free water migration velocity 100cm/a. a) Magnitude of velocity overplotted with velocity vectors, b) Snapshots of material distribution in time, c) Snapshots of bound water distribution in time and d) Snapshots of free water distribution in time.

At $\sim$ 158 Ma model reaches quasi-steady state and no free water is observed in the model, i.e. no saturated material is crossing the dehydration front and no free water is generated.

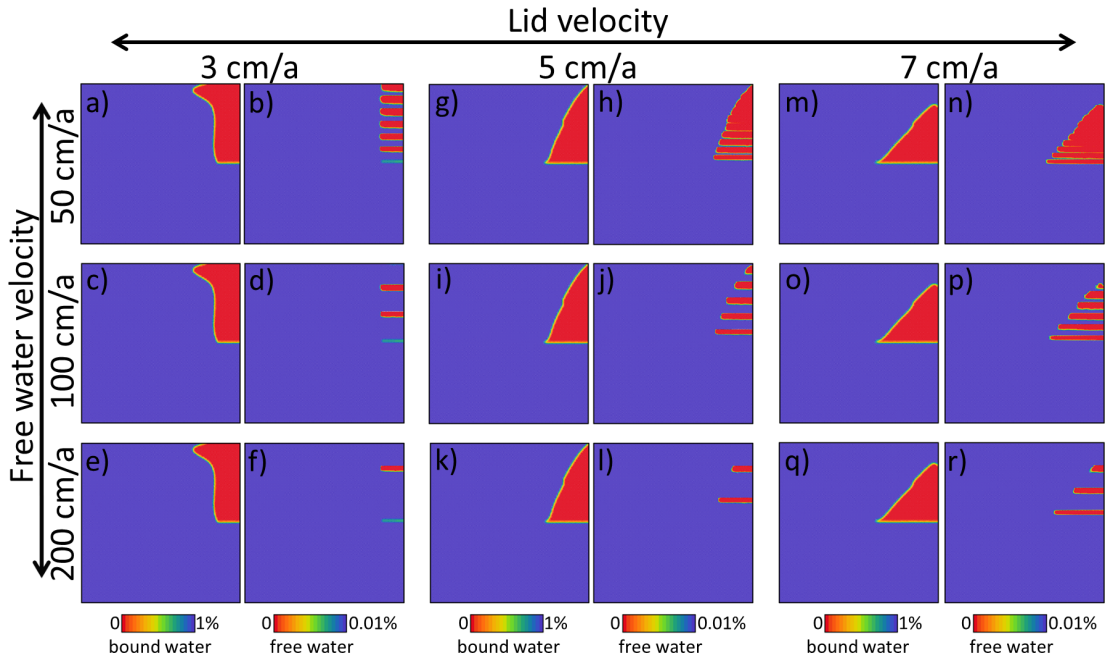

Figure A.2: Snapshots of bound and free water taken at approx. 32 Ma for models differing in lid velocity and free water migration velocity. a) - f) lid velocity of 3 cm/a, g) - l) lid velocity of 5 cm/a and m) - r) lid velocity of 7 cm/a. Free water migration velocity of 50 cm/a is valid for models in panels a), b), g), h), m) and n), of 100 cm/a in panels c), d), i), j), o) and p) and 200 cm/a in panels e), f), k), l), q) and r).

To further illustrate the effects of parameters controlling dehydration of the system, namely the lid velocity and free water migration velocity, we show 9 models differing in lid velocity in the range from 3 to 7 cm/a and in free water migration velocity varying from 50 to 200 cm/a. Figure A.2 shows one snapshot for each of these models. Snapshots are displayed at t=32 Ma. We can notice that bound water in models with higher lid velocity (see e.g. Fig. A.2 m) reaches a lower depth compared to the ones with lower lid velocity (see e.g. Fig. A.2 a). These models with higher lid velocity also show closer distribution of the discrete stripes of free water (compare e.g. Fig. A.2 b, n). This is caused by the fact that within one integration time step, more of wet material crosses the dehydration front, following that more background grid cells are covered with the material that must be dehydrated. Because the migration of free water is treated on a background grid cell level, the more cells are dehydrated in one integration time step, the more cells (stripes that are closer to each other) need to be occupied by the free water. Consequently, more background grid cells are covered with material requiring dehydration. As more cells are dehydrated there is a need for a higher number of closely situated cells to be filled with free water in the top

half of the model domain. With increasing the free water migration velocity, the evolution of the bound water is not affected (compare e.g. Fig. A.2 a, e). On the other hand, free water distribution is affected considerably - the distance of the discrete free water stripes is growing with increasing migration velocity. This is because the released water travels a greater distance within one integration time step.

Conclusions

This thesis tried to deepen our knowledge of factors that control slab deformation in numerical models. We contributed to a detailed understanding of how crustal and mantle rheologies, potentially impacted by the presence of water, influence deep slab deformation and how is this deformation connected to deep earthquakes and oscillations in the lithospheric plate motions.

Our models show how an entrained weak layer between the subducting and overriding plates impacts the decoupling of these plates and affects the overall subduction dynamics. We point out that both the thickness and viscosity of this crust are crucial; thicker or less viscous crustal layer promotes slab decoupling, facilitating faster rollback and potential stagnation in the transition zone, while stronger or thinner crust leads to reduced rollback and easier penetration into the lower mantle. Further, models with nonlinear crustal rheology show a strong feedback between slab velocity and crustal viscosity. Crustal viscosity is anti-correlated with subducting plate velocity - it decreases as the strain-rate increases during slab acceleration, while it increases as the slab slows down and strain-rate is reduced. Slab rollback is closely linked to the slab dip angle - the shallower the angle, the more it promotes rollback (potentially alongside subhorizontal buckling) and may lead to slab stagnation. Conversely, slabs with a steep dip angle tend to exhibit vertical buckling and limited rollback, and are more likely to penetrate into the lower mantle.

An application of our numerical models in natural subduction zone is further used to shed more light on deep seismicity in the Tonga subduction region. The motivation for this research was to explain the unusual stress regime of deep earthquakes focal mechanism at the boundary between the transition zone and lower mantle. We demonstrated that the observed stress rotation from vertical to subhorizontal compression at the boundary between the upper and lower mantle is primarily caused by the bending forces of the slab, that overprint the effect of petrological buoyancy associated with the phase transitions.

Further, our models were used to connect the surface plate motions with deep slab deformation. Recent plate kinematic reconstructions revealed that the convergence rate between India and Africa contains rapid oscillations with an amplitude of 10 cm/a at a period of 6-8 Ma. We show that these oscillations are caused by the quasiperiodic buckling of the slab in the transition zone. Alternating episodes of forward and backward buckling are inducing variations in subduction velocity and hence in lithospheric plate motions. We conclude that the amplitude and period of the oscillations in plate velocity depend on the average subduction velocity. Faster subducting plates have higher velocity amplitudes and lower periods of oscillation. The rapid oscillations in plate motion that we observed in our numerical models, occur over similar periods to those detected in the detailed (0.5-1 Ma) analysis of marine magnetic anomalies in the Indian Ocean, in contrast with earlier plate reconstructions on broader stage intervals of 3-10 Ma. These rapid oscillations may be relevant to fluid and magmatic processes in the subducution

zones. Thus, we conclude that higher-resolution plate reconstructions, in sense of finer sampling, could lead to a better understanding of these processes and are therefore important. Our models indicate that rapid oscillations may result from the subducting slab buckling due to space constraints and lower sinking rates in the lower mantle. This implies that typical plate motions are mainly driven in the top few hundred kilometers of the Earth. Additionally, because the top 100 km of the Earth resists plate motion due to friction and drag, plate tectonics is primarily driven between depths of approximately 100 and 500 km (6-7% of the Earth's radius).

Finally, we explored the influence of water that is initially bound in the crustal material, on subduction dynamics. We demonstrated that variations in the viscosity contrast between wet and dry crustal material can alter the velocity of subducting slabs, ultimately deciding whether subduction is penetrative or stagnant. Our models comparing wet and dry crust show that the effect of water can be approximated in dry models by simply lowering the uniform crustal viscosity. We also show that water that is removed from the crust with increasing pressure and temperature influences the mantle wedge rheology, accelerates slab movement, and slightly alters subduction dynamics. In the studied range of parameters is its role however relatively small. Additionally, we show that water-dependent density changes within subduction models cause further deceleration of the downgoing slab.

Future applications of these models in natural subduction zones will allow a broader range of research questions to be addressed, including the presence of water in the deep transition zone or dehydration-related seismicity.

Bibliography

R. Agrusta, J. Van Hunen, and S. Goes. The effect of metastable pyroxene on the slab dynamics. *Geophysical Research Letters*, 41(24):8800–8808, 2014. ISSN 19448007. doi: 10.1002/2014GL062159.

R. Agrusta, S. Goes, and J. van Hunen. Subducting-slab transition-zone interaction: Stagnation, penetration and mode switches. *Earth and Planetary Science Letters*, 464:10–23, 2017. ISSN 0012821X. doi: 10.1016/j.epsl.2017.02.005.

J. C. Alt, J. Honnorez, C. Laverne, and R. Emmermann. Hydrothermal alteration of a 1 km section through the upper oceanic crust, deep sea drilling project hole 504b: Mineralogy, chemistry and evolution of seawater-basalt interactions. *Journal of Geophysical Research: Solid Earth*, 91(B10):10309–10335, 1986.

C. Amante and B. W. Eakins. ETOPO1 1 arc-minute global relief model: procedures, data sources and analysis. NOAA technical memorandum NESDIS NGDC-24, 19. 2009.

M. L. Amaru. *Global travel time tomography with 3-D reference models*. PhD thesis, Utrecht University, 2007.

A. Androvičová, H. Čížková, and A. van den Berg. The effects of rheological decoupling on slab deformation in the Earth's upper mantle. *Studia Geophysica et Geodaetica*, 2013. ISSN 00393169. doi: 10.1007/s11200-012-0259-7.

D. Arcay, E. Tric, and M. P. Doin. Numerical simulations of subduction zones. Effect of slab deghydration on the mantle wedge dynamics. *Physics of the Earth and Planetary Interiors*, 149(1-2 SPEC. ISS.):133–153, 2005. ISSN 00319201. doi: 10.1016/j.pepi.2004.08.020.

K. Arredondo and M. Billen. Coupled effects of phase transitions and rheology in 2D dynamical models of subduction. *J. Geophys. Res. Solid Earth*, 122: 5813–5830, 2017. doi: 10.1002/2017JB014374.

K. M. Arredondo and M. I. Billen. The effects of phase transitions and compositional layering in two-dimensional kinematic models of subduction. *Journal of Geodynamics*, 100:159–174, oct 2016. ISSN 0264-3707. doi: 10.1016/J.JOG.2016.05.009.

E. Barbier. Geothermal energy technology and current status: an overview. *Renewable and Sustainable Energy Reviews*, 6(1):3–65, 2002. ISSN 1364-0321. doi: https://doi.org/10.1016/S1364-0321(02)00002-3.

M. Běhounková and H. Čížková. Long-wavelength character of subducted slabs in the lower mantle. *Earth and Planetary Science Letters*, 275(1-2):43–53, 2008. ISSN 0012821X. doi: 10.1016/j.epsl.2008.07.059.

W. M. Behr and T. W. Becker. Sediment control on subduction plate speeds. *Earth and Planetary Science Letters*, 502:166–173, 2018.

W. M. Behr, A. F. Holt, T. W. Becker, and C. Faccenna. The effects of plate interface rheology on subduction kinematics and dynamics. *Geophysical Journal International*, 230(2):796–812, 2022. doi: 10.1093/gji/ggac075.

D. Bercovici and S.-i. Karato. Whole-mantle convection and the transition-zone water filter. *Nature*, 425(6953):39–44, 2003.

D. Bercovici, G. Schubert, and Y. Ricard. Abrupt tectonics and rapid slab detachment with grain damage. *Proceedings of the National Academy of Sciences*, 112(5):1287–1291, 2015. doi: 10.1073/pnas.1415473112.

H. Bijwaard, W. Spakman, and E. R. Engdahl. Closing the gap between regional and global travel time tomography. *Journal of Geophysical Research: Solid Earth*, 103(B12):30055–30078, 1998. ISSN 01480227. doi: 10.1029/98JB02467.

S. L. Bilek, C. P. Conrad, and C. Lithgow-Bertelloni. Slab pull, slab weakening, and their relation to deep intra-slab seismicity. *Geophysical research letters*, 32 (14), 2005. doi: doi.org/10.1029/2005GL022922.

M. I. Billen. Slab dynamics in the transition zone. *Physics of the Earth and Planetary Interiors*, 183(1):296 – 308, 2010. ISSN 0031-9201. doi: https://doi.org/10.1016/j.pepi.2010.05.005. Special Issue on Deep Slab and Mantle Dynamics.

M. I. Billen. Deep slab seismicity limited by rate of deformation in the transition zone. *Science Advances*, 6(22):7692, 2020. doi: 10.1126/sciadv.aaz7692.

M. I. Billen and K. M. Arredondo. Decoupling of plate-asthenosphere motion caused by non-linear viscosity during slab folding in the transition zone. *Physics of the Earth and Planetary Interiors*, 281:17–30, 2018. ISSN 0031-9201. doi: https://doi.org/10.1016/j.pepi.2018.04.011.

M. I. Billen and G. Hirth. Rheologic controls on slab dynamics. *Geochemistry, Geophysics, Geosystems*, 8(8), 2007. ISSN 15252027. doi: 10.1029/2007GC001597.

C. R. Bina and G. Helffrich. Phase transition clapeyron slopes and transition zone seismic discontinuity topography. *Journal of Geophysical Research: Solid Earth*, 99(B8):15853–15860, 1994. doi: 10.1029/94JB00462.

C. R. Bina and H. Kawakatsu. Buoyancy, bending, and seismic visibility in deep slab stagnation. *Physics of the Earth and Planetary Interiors*, 183(1-2): 330–340, 2010. doi: doi.org/10.1016/j.pepi.2010.04.010.

C. R. Bina, S. Stein, F. C. Marton, and E. M. V. Ark. Implications of slab mineralogy for subduction dynamics. *Physics of the Earth and Planetary Interiors*, 127(1):51 – 66, 2001. ISSN 0031-9201. doi: https://doi.org/10.1016/S0031-9201(01)00221-7.

A. Bögli. *Karst hydrology and physical speleology*. Springer Science & Business Media, 2012.

N. Bolfan-Casanova, H. Keppler, and D. C. Rubie. Water partitioning at 660 km depth and evidence for very low water solubility in magnesium silicate perovskite. *Geophysical Research Letters*, 30(17), 2003.

R. Bousquet, B. Goffé, P. Henry, X. Le Pichon, and C. Chopin. Kinematic, thermal and petrological model of the Central Alps: Lepontine metamorphism in the upper crust and eclogitisation of the lower crust. *Tectonophysics*, 273 (1-2):105–127, 1997.

A. Boutoux, A. Briaud, C. Faccenna, P. Ballato, F. Rossetti, and E. Blanc. Slab Folding and Surface Deformation of the Iran Mobile Belt. *Tectonics*, 40(6): e2020TC006300, 2021. doi: https://doi.org/10.1029/2020TC006300.

A. Briaud, R. Agrusta, C. Faccenna, F. Funiciello, and J. van Hunen. Topographic fingerprint of deep mantle subduction. *Journal of Geophysical Research: Solid Earth*, 125(1):e2019JB017962, 2020. doi: https://doi.org/10.1029/2019JB017962.

P. C. Burnley, H. W. Green, and D. J. Prior. Faulting associated with the olivine to spinel transformation in Mg_2GeO_4 and its implications for deep-focus earthquakes. *Journal of Geophysical Research: Solid Earth*, 96(B1):425–443, 1991. doi: doi.org/10.1029/90JB01937.

E. Burov and G. Schubert. Plate rheology and mechanics. *Treatise on Geophysics Vol 6-Crust and Lithosphere Dynamics*, pages 99–151, 2007.

N. Butterworth, A. Talsma, R. Müller, M. Seton, H.-P. Bunge, B. Schuberth, G. Shephard, and C. Heine. Geological, tomographic, kinematic and geodynamic constraints on the dynamics of sinking slabs. *Journal of Geodynamics*, 73:1–13, 2014. ISSN 0264-3707. doi: https://doi.org/10.1016/j.jog.2013.10.006.

J. Byerlee. Friction of rocks. pages 615–626, 1978.

C. Cai and D. A. Wiens. Dynamic triggering of deep earthquakes within a fossil slab. *Geophysical Research Letters*, 43(18):9492–9499, 2016. doi: doi.org/10.1002/2016GL070347.

F. Capitanio, D. Stegman, L. Moresi, and W. Sharples. Upper plate controls on deep subduction, trench migrations and deformations at convergent margins. *Tectonophysics*, 483(1):80–92, 2010. ISSN 0040-1951. doi: https://doi.org/10.1016/j.tecto.2009.08.020.

F. Capitanio, C. Faccenna, S. Zlotnik, and D. Stegman. Subduction dynamics and the origin of Andean orogeny and the Bolivian orocline. *Nature*, 480(7375): 83–86, 2011.

S. Carbotte and D. Scheirer. Variability of ocean crustal structure created along the global midocean ridge. In *Hydrogeology of the Oceanic Lithosphere*, pages 59–107. 2004.

R. Carlson and D. Jay Miller. Influence of pressure and mineralogy on seismic velocities in oceanic gabbros: Implications for the composition and state of the

lower oceanic crust. *Journal of Geophysical Research: Solid Earth*, 109(B9), 2004.

N. Cerpa, R. Hassani, M. Gerbault, and J.-H. Prevost. A fictious domain method for lithosphere-astenosphere interaction: Application to periodic slab folding in the upper mantle. *Geochemistry, Geophysics, Geosystems*, 15:1852–1877, 2014. doi: 10.1002/2014GC005241.

N. G. Cerpa, B. Guillaume, and J. Martinod. The interplay between overriding plate kinematics, slab dip and tectonics. *Geophysical Journal International*, 215(3):1789–1802, 09 2018. ISSN 0956-540X. doi: 10.1093/gji/ggy365.

N. G. Cerpa, K. Sigloch, F. Garel, A. Heuret, D. R. Davies, and M. G. Mihalynuk. The effect of a weak asthenospheric layer on surface kinematics, subduction dynamics and slab morphology in the lower mantle. *Journal of Geophysical Research: Solid Earth*, 127(8):e2022JB024494, 2022. doi: doi.org/10.1029/2022JB024494.

B. Cesare, G. Cruciani, and U. Russo. Hydrogen deficiency in Ti-rich biotite from anatectic metapelites (El Joyazo, SE Spain): Crystal-chemical aspects and implications for high-temperature petrogenesis. *American Mineralogist*, 88 (4):583–595, 2003. doi: doi:10.2138/am-2003-0412.

J. B. Chapman, J. E. Shields, M. N. Ducea, S. R. Paterson, S. Attia, and K. E. Ardill. The causes of continental arc flare ups and drivers of episodic magmatic activity in Cordilleran orogenic systems. *Lithos*, 398-399:106307, 2021. ISSN 0024-4937. doi: https://doi.org/10.1016/j.lithos.2021.106307.

C. Chelle-Michou, M. Chiaradia, D. Selby, M. Ovtcharova, and R. A. Spikings. High-resolution geochronology of the Coroccohuayco porphyry-skarn deposit, Peru: A rapid product of the Incaic orogeny. *Economic Geology*, 110(2):423–443, 03 2015. ISSN 0361-0128. doi: 10.2113/econgeo.110.2.423.

Z. Chemia, D. Dolejš, and G. Steinle-Neumann. Thermal effects of variable material properties and metamorphic reactions in a three-component subducting slab. *Journal of Geophysical Research: Solid Earth*, 120(10):6823–6845, 2015.

Y.-W. Chen, J. Wu, and J. Suppe. Southward propagation of nazca subduction along the andes. *Nature*, 565(7740):441–447, 2019.

M. V. Chertova, T. Geenen, A. Van Den Berg, and W. Spakman. Using open sidewalls for modelling self-consistent lithosphere subduction dynamics. *Solid Earth*, 3(2):313–326, 2012. ISSN 18699510. doi: 10.5194/se-3-313-2012.

U. R. Christensen. The influence of trench migration on slab penetration into the lower mantle. *Earth and Planetary Science Letters*, 140(1-4):27–39, 1996. ISSN 0012821X. doi: 10.1016/0012-821X(96)00023-4.

U. R. Christensen and D. A. Yuen. Layered convection induced by phase transitions. *Journal of Geophysical Research: Solid Earth*, 90(B12):10291–10300, 1985.

H. Čížková and C. R. Bina. Effects of mantle and subduction-interface rheologies on slab stagnation and trench rollback. *Earth and Planetary Science Letters*, 379:95–103, 2013. ISSN 0012821X. doi: 10.1016/j.epsl.2013.08.011.

H. Čížková and C. R. Bina. Linked influences on slab stagnation: Interplay between lower mantle viscosity structure, phase transitions, and plate coupling. *Earth and Planetary Science Letters*, 509:88–99, 2019. ISSN 0012821X. doi: 10.1016/j.epsl.2018.12.027.

H. Čížková, J. Van Hunen, A. P. Van den Berg, and N. J. Vlaar. The influence of rheological weakening and yield stress on the interaction of slabs with the 670 km discontinuity. 199(3-4):447–457, 2002. ISSN 0012821X. doi: 10.1016/S0012-821X(02)00586-1.

H. Čížková, J. van Hunen, and A. van den Berg. Stress distribution within subducting slabs and their deformation in the transition zone. *Physics of the Earth and Planetary Interiors*, 161(3-4):202–214, 2007. ISSN 00319201. doi: 10.1016/j.pepi.2007.02.002.

H. Čížková, A. P. van den Berg, W. Spakman, and C. Matyska. The viscosity of Earth's lower mantle inferred from sinking speed of subducted lithosphere. *Physics of the Earth and Planetary Interiors*, 200-201:56–62, 2012. ISSN 00319201. doi: 10.1016/j.pepi.2012.02.010.

S. R. Clark, D. Stegman, and R. D. Müller. Episodicity in back-arc tectonic regimes. *Physics of the Earth and Planetary Interiors*, 171(1):265–279, 2008. ISSN 0031-9201. doi: https://doi.org/10.1016/j.pepi.2008.04.012. Recent Advances in Computational Geodynamics: Theory, Numerics and Applications.

N. Coltice, L. Husson, C. Faccenna, and M. Arnould. What drives tectonic plates? *Science Advances*, 5(10):eaax4295, 2019. doi: 10.1126/sciadv.aax4295.

J. Connolly and D. Kerrick. An algorithm and computer program for calculating composition phase diagrams. *Calphad*, 11(1):1–55, 1987. ISSN 0364-5916. doi: https://doi.org/10.1016/0364-5916(87)90018-6.

J. A. Connolly. Computation of phase equilibria by linear programming: A tool for geodynamic modeling and its application to subduction zone decarbonation. *Earth and Planetary Science Letters*, 236(1-2):524–541, 2005. ISSN 0012821X. doi: 10.1016/j.epsl.2005.04.033.

F. Crameri and P. J. Tackley. Spontaneous development of arcuate single-sided subduction in global 3-D mantle convection models with a free surface. *Journal of Geophysical Research: Solid Earth*, 119, 07 2014. doi: 10.1002/2014JB010939.

C. Cuvelier, A. Segal, and A. van Steenhoven. *Finite Element Methods and Navier–Stokes Equations*. D. Reidel Publishing Company, 1986. ISBN 9027721483. doi: 10.1007/978-94-010-9333-0.

R. Dasgupta, N. Mandal, and C. Lee. Controls of subducting slab dip and age on the extensional versus compressional deformation in the overriding plate. *Tectonophysics*, 801:228716, 2021. ISSN 0040-1951. doi: https://doi.org/10.1016/j.tecto.2020.228716.

C. DeMets and S. Merkouriev. Detailed reconstructions of India–Somalia Plate motion, 60 Ma to present: implications for Somalia Plate absolute motion and India–Eurasia Plate motion. *Geophysical Journal International*, 227(3):1730–1767, 07 2021. ISSN 0956-540X. doi: 10.1093/gji/ggab295.

P. V. Doubrovine, B. Steinberger, and T. H. Torsvik. Absolute plate motions in a reference frame defined by moving hot spots in the Pacific, Atlantic, and Indian oceans. *Journal of Geophysical Research: Solid Earth*, 117(B9), 2012. doi: https://doi.org/10.1029/2011JB009072.

J. I. Drever. *Surface and Ground Water, Weathering, and Soils: Treatise on Geochemistry, Volume 5*, volume 5. Elsevier, 2005.

J. C. Duarte, W. P. Schellart, and A. R. Cruden. How weak is the subduction zone interface? *Geophysical Research Letters*, 42(8):2664–2673, 2015. ISSN 19448007. doi: 10.1002/2014GL062876.

M. A. Eberle, O. Grasset, and C. Sotin. A numerical study of the interaction between the mantle wedge, subducting slab, and overriding plate. *Physics of the Earth and Planetary Interiors*, 134(3-4):191–202, 2002.

V. Espinoza and G. Iaffaldano. Rapid absolute plate motion changes inferred from high-resolution relative spreading reconstructions: A case study focusing on the South America plate and its Atlantic/Pacific neighbors. *Earth and Planetary Science Letters*, 604:118009, 2023. ISSN 0012-821X. doi: https://doi.org/10.1016/j.epsl.2023.118009.

N. Eyles. The role of meltwater in glacial processes. *Sedimentary Geology*, 190(1):257–268, 2006. ISSN 0037-0738. doi: https://doi.org/10.1016/j.sedgeo.2006.05.018. Sedimentology and Sequence Stratigraphy of Fluvial Deposits.

M. Faccenda. Water in the slab: A trilogy. *Tectonophysics*, 614:1–30, 2014. ISSN 0040-1951. doi: https://doi.org/10.1016/j.tecto.2013.12.020.

M. Faccenda and L. D. Zilio. The role of solid–solid phase transitions in mantle convection. *Lithos*, 268-271:198 – 224, 2017. ISSN 0024-4937. doi: https://doi.org/10.1016/j.lithos.2016.11.007.

Y. Fei, J. Van Orman, J. Li, W. van Westrenen, C. Sanloup, W. Minarik, K. Hirose, T. Komabayashi, M. Walter, and K. Funakoshi. Experimentally determined postspinel transformation boundary in Mg_2SiO_4 using MgO as an internal pressure standard and its geophysical implications. *Journal of Geophysical Research: Solid Earth*, 109(B2), 2004. doi: https://doi.org/10.1029/2003JB002562.

T. Fockenberg. An experimental study of the pressure-temperature stability of MgMgAl-pumpellyite in the system $MgO - Al_2O_3 - SiO_2 - H_2O$. *American Mineralogist*, 83(3-4):220–227, 1998. doi: doi:10.2138/am-1998-3-404.

D. Forsyth and S. Uyeda. On the Relative Importance of the Driving Forces of Plate Motion. *Geophysical Journal of the Royal Astronomical Society*, 43: 163–200, 1975. doi: 10.1111/j.1365-246X.1975.tb00631.x.

Y. Fukao and M. Obayashi. Subducted slabs stagnant above, penetrating through, and trapped below the 660 km discontinuity. *Journal of Geophysical Research: Solid Earth*, 118(11):5920–5938, 2013. doi: doi.org/10.1002/2013JB010466.

Y. Fukao, M. Obayashi, and J. Yoshimitsu. Mechanisms of ultra-deep earthquakes (h>680km) in a slab penetrating the 660-km discontinuity. *JpGU Meeting Abstracts*, pages SIT03–12, 2014.

F. Garel, S. Goes, D. R. Davies, J. H. Davies, S. C. Kramer, and C. R. Wilson. Interaction of subducted slabs with the mantle transition-zone: A regime diagram from 2-D thermo-mechanical models with a mobile trench and an overriding plate. *Geochemistry, Geophysics, Geosystems*, 15(5):1739–1765, 2014. ISSN 15252027. doi: 10.1002/2014GC005257.

H. Genda. Origin of earth's oceans: An assessment of the total amount, history and supply of water. *Geochemical Journal*, 50(1):27–42, 2016. doi: 10.2343/geochemj.2.0398.

T. Gerya and F. Meilick. Geodynamic regimes of subduction under an active margin: effects of rheological weakening by fluids and melts. *Journal of Metamorphic Geology*, 29:7–31, 2010. doi: 10.1111/j.1525-1314.2010.00904.x.

T. V. Gerya, D. Bercovici, and T. W. Becker. Dynamic slab segmentation due to brittle–ductile damage in the outer rise. *Nature*, 599(7884):245–250, 2021. doi: doi.org/10.1038/s41586-021-03937-x.

G. Gibert, M. Gerbault, R. Hassani, and E. Tric. Dependency of slab geometry on absolute velocities and conditions for cyclicity: insights from numerical modelling. *Geophysical Journal International*, 189(2):747–760, 05 2012.

S. Goes, F. Capitanio, G. Morra, M. Seton, and D. Giardini. Signatures of downgoing plate-buoyancy driven subduction in Cenozoic plate motions. *Physics of the Earth and Planetary Interiors*, 184(1):1–13, 2011. ISSN 0031-9201. doi: https://doi.org/10.1016/j.pepi.2010.10.007.

S. Goes, R. Agrusta, J. van Hunen, and F. Garel. Subduction-transition zone interaction: A review. *Geosphere*, 13(3):644–664, jun 2017.

R. G. Gordon, A. Cox, and S. O'Hare. Paleomagnetic Euler poles and the apparent polar wander and absolute motion of North America since the Carboniferous. *Tectonics*, 3(5):499–537, 1984. doi: https://doi.org/10.1029/TC003i005p00499.

H. W. Green. Phase-transformation-induced lubrication of earthquake sliding. *Philosophical Transactions of the Royal Society A: Mathematical, Physical and Engineering Sciences*, 375(2103):20160008, 2017. doi: doi.org/10.1098/rsta.2016.0008.

D. Gürer, R. Granot, and D. J. van Hinsbergen. Plate tectonic chain reaction revealed by noise in the cretaceous quiet zone. *Nature Geoscience*, 15(3):233–239, 2022.

M. Gurnis and B. H. Hager. Controls of the structure of subducted slabs. *Nature*, 335(6188):317–321, 1988. doi: doi.org/10.1038/335317a0.

R. Hall. Cenozoic geological and plate tectonic evolution of SE Asia and the SW Pacific: computer-based reconstructions, model and animations. *Journal of Asian Earth Sciences*, 20(4):353–431, 2002. doi: doi.org/10.1016/S1367-9120(01)00069-4.

U. Hansen, D. A. Yuen, S. Kroening, and L. T. B. Dynamical consequences of depth-dependent thermal expansivity and viscosity on mantle circulations and thermal structure. *Physics of the Earth and Planetary Interiors*, 77:205–223, 1993.

C. Hensen, K. Wallmann, M. Schmidt, C. R. Ranero, and E. Suess. Fluid expulsion related to mud extrusion off Costa Rica - A window to the subducting slab. *Geology*, 32(3):201–204, 2004. ISSN 00917613. doi: 10.1130/G20119.1.

D. Hernández-Uribe, R. M. Palin, K. A. Cone, and W. Cao. Petrological Implications of Seafloor Hydrothermal Alteration of Subducted Mid-Ocean Ridge Basalt. *Journal of Petrology*, 61(9):egaa086, 08 2020. ISSN 0022-3530. doi: 10.1093/petrology/egaa086.

K. Hirose. Phase transitions in pyrolitic mantle around 670-km depth: Implications for upwelling of plumes from the lower mantle. *Journal of Geophysical Research: Solid Earth*, 107(B4):ECV 3–1–ECV 3–13, 2002. doi: https://doi.org/10.1029/2001JB000597.

M. M. Hirschmann. Water, Melting, and the Deep Earth H_2O Cycle . *Annual Review of Earth and Planetary Sciences*, 34(1):629–653, 2006. doi: 10.1146/annurev.earth.34.031405.125211.

G. Hirth and D. Kohlstedt. In: Rheology of the upper mantle and the mantle wedge: A view from the experimentalists. *Washington DC American Geophysical Union Geophysical Monograph Series*, 138:83–105, 2003a. doi: 10.1029/138GM06.

G. Hirth and D. L. Kohlstedt. Rheology of the Upper Mantle and the Mantle Wedge : A View from the Experimentalists upper mantle . We first analyze experimental data to provide a critical review of flow. *Geophysical Monograph Series*, 138:83–105, 2003b. doi: 10.1029/138GM06.

R. W. Hockney and J. W. Eastwood. *Computer simulation using particles*. Institute of Physics Publising Ltd, Bristol, 1988.

T. J. B. Holland and R. Powell. An internally consistent thermodynamic data set for phases of petrological interest. *Journal of Metamorphic Geology*, 16(3):309–343, 1998. doi: https://doi.org/10.1111/j.1525-1314.1998.00140.x.

A. F. Holt, T. W. Becker, and B. A. Buffett. Trench migration and overriding plate stress in dynamic subduction models. *Geophysical Journal International*, 201(1):172–192, 2015. ISSN 1365246X. doi: 10.1093/gji/ggv011.

K. Hosseini, K. J. Matthews, K. Sigloch, G. E. Shephard, M. Domeier, and M. Tsekhmistrenko. Submachine: Web-based tools for exploring seismic tomography and other models of Earth's deep interior. *Geochemistry, Geophysics, Geosystems*, 19(5):1464–1483, 2018. doi: doi.org/10.1029/2018GC007431.

J. Hu, M. Gurnis, J. Rudi, G. Stadler, and R. D. Müller. Dynamics of the abrupt change in pacific plate motion around 50 million years ago. *Nature Geoscience*, 15(1):74–78, 2022.

T. Inoue, H. Yurimoto, and Y. Kudoh. Hydrous modified spinel, $Mg_{1.75}SiH_{0.5}O_4$: a new water reservoir in the mantle transition region. *Geophysical Research Letters*, 22(2):117–120, 1995.

T. Inoue, D. J. Weidner, P. A. Northrup, and J. B. Parise. Elastic properties of hydrous ringwoodite (γ-phase) in Mg_2Sio_4. *Earth and Planetary Science Letters*, 160(1-2):107–113, 1998.

K. Ishii and S. R. Wallis. A possible mechanism for spontaneous cyclic back-arc spreading. *Progress in Earth and Planetary Science*, 9(1):27, 2022.

T. Ishii and E. Ohtani. Dry metastable olivine and slab deformation in a wet subducting slab. *Nature Geoscience*, 14(7):526–530, 2021. doi: doi.org/10.1038/s41561-021-00756-7.

T. Ishii, H. Kojitani, and M. Akaogi. Post-spinel transitions in pyrolite and Mg_2SiO_4 and akimotoite–perovskite transition in $MgSiO_3$: Precise comparison by high-pressure high-temperature experiments with multi-sample cell technique. *Earth and Planetary Science Letters*, 309(3):185–197, 2011. ISSN 0012-821X. doi: https://doi.org/10.1016/j.epsl.2011.06.023.

J. Ita and S. D. King. Sensitivity of convection with an endothermic phase change to the form of governing equations, initial conditions, boundary conditions, and equation of state. *Journal of Geophysical Research*, 99(B8):15919, aug 1994. ISSN 0148-0227. doi: 10.1029/94JB00852.

H. Iwamori. Transportation of H_2O and melting in subduction zones. *Earth and Planetary Science Letters*, 160(1):65–80, 1998. ISSN 0012-821X. doi: https://doi.org/10.1016/S0012-821X(98)00080-6.

H. Iwamori. Phase relations of peridotites under H_2O-saturated conditions and ability of subducting plates for transportation of H_2O. *Earth and Planetary Science Letters*, 227(1-2):57–71, 2004. ISSN 0012821X. doi: 10.1016/j.epsl.2004.08.013.

H. Iwamori. Transportation of H_2O beneath the Japan arcs and its implications for global water circulation. *Chemical Geology*, 239(3-4):182–198, 2007. ISSN 00092541. doi: 10.1016/j.chemgeo.2006.08.011.

M. H. Jacobs and A. P. van den Berg. Complex phase distribution and seismic velocity structure of the transition zone: Convection model predictions for a magnesium-endmember olivine–pyroxene mantle. *Physics of the Earth and Planetary Interiors*, 186(1):36–48, 2011. ISSN 0031-9201. doi: https://doi.org/10.1016/j.pepi.2011.02.008.

M. H. Jacobs, R. Schmid-Fetzer, and A. P. van den Berg. An alternative use of kieffer's lattice dynamics model using vibrational density of states for constructing thermodynamic databases. *Physics and Chemistry of Minerals*, 40: 207–227, 2013.

R. D. Jarrard. Subduction fluxes of water, carbon dioxide, chlorine, and potassium. *Geochemistry, Geophysics, Geosystems*, 4(5), 2003.

M. Kameyama, D. A. Yuen, and S.-I. Karato. Thermal-mechanical effects of low-temperature plasticity (the Peierls mechanism) on the deformation of a viscoelastic shear zone. *Earth and Planetary Science Letters*, 168(1-2):159–172, apr 1999. ISSN 0012-821X. doi: 10.1016/S0012-821X(99)00040-0.

M. Kanzaki. Stability of hydrous magnesium silicates in the mantle transition zone. *Physics of the Earth and Planetary Interiors*, 66(3):307–312, 1991. ISSN 0031-9201. doi: https://doi.org/10.1016/0031-9201(91)90085-V.

S.-i. Karato. Deformation of earth materials. *An Introduction to the Rheology of Solid Earth*, 463, 2008.

S.-i. Karato and H. Jung. Water, partial melting and the origin of the seismic low velocity and high attenuation zone in the upper mantle. *Earth and Planetary Science Letters*, 157(3):193 – 207, 1998. ISSN 0012-821X. doi: https://doi.org/10.1016/S0012-821X(98)00034-X.

S.-i. Karato and P. Wu. Rheology of the Upper Mantle: A Synthesis. *Science*, 260(5109):771–778, 1993. ISSN 0036-8075. doi: 10.1126/science.260.5109.771.

S.-i. Karato, S. Zhang, and H.-R. Wenk. Superplasticity in Earth's Lower Mantle: Evidence from Seismic Anisotropy and Rock Physics. *Science*, 270(5235):458 LP – 461, oct 1995.

S. I. Karato, M. Riedel, and Y. DA. Rheological structure and deformation of subducted slabs in the mantle transition zone: implications for mantle circulation and deep earthquakes. *Physics Earth and Planetary Interiors*, 3994:1–26, 2001. doi: doi.org/10.1016/S0031-9201(01)00223-0.

J. A. Karson. Geologic Structure of the Uppermost Oceanic Crust Created at Fast- to Intermediate-Rate Spreading Centers. *Annual Review of Earth and Planetary Sciences*, 30(1):347–384, 2002. ISSN 0084-6597. doi: 10.1146/annurev.earth.30.091201.141132.

T. Katsura, H. Yamada, T. Shinmei, A. Kubo, S. Ono, M. Kanzaki, A. Yoneda, M. J. Walter, E. Ito, S. Urakawa, K. Funakoshi, and W. Utsumi. Post-spinel transition in Mg_2SiO_4 determined by high P–T in situ X-ray diffractometry. *Physics of the Earth and Planetary Interiors*, 136(1):11–24, 2003. ISSN 0031-9201. doi: https://doi.org/10.1016/S0031-9201(03)00019-0.

T. Katsura, H. Yamada, O. Nishikawa, M. Song, A. Kubo, T. Shinmei, S. Yokoshi, Y. Aizawa, T. Yoshino, M. J. Walter, E. Ito, and K.-i. Funakoshi. Olivine-wadsleyite transition in the system $(Mg, Fe)_2SiO_4$. *Journal of Geophysical Research: Solid Earth*, 109(B2), 2004. doi: https://doi.org/10.1029/2003JB002438.

T. Katsura, S. Yokoshi, K. Kawabe, A. Shatskiy, M. Manthilake, S. Zhai, H. Fukui, H. Hegoda, T. Yoshino, D. Yamazaki, T. Matsuzaki, A. Yoneda, E. Ito, M. Sugita, N. Tomioka, K. Hagiya, A. Nozawa, and K.-i. Funakoshi. P-V-T relations of $MgSiO_3$ perovskite determined by in situ X-ray diffraction using a large-volume high-pressure apparatus. *Geophysical Research Letters*, 36, 01 2009. doi: 10.1029/2009GL039318.

T. Kawamoto. Hydrous phase stability and partial melt chemistry in H_2O-saturated KLB-1 peridotite up to the uppermost lower mantle conditions. *Physics of the Earth and Planetary Interiors*, 143-144:387–395, 2004. ISSN 0031-9201. doi: https://doi.org/10.1016/j.pepi.2003.06.003.

T. Kawamoto, K. Leinenweber, R. L. Hervig, and J. R. Holloway. Stability of hydrous minerals in H_2O-saturated KLB-1 peridotite up to 15 GPA. *AIP Conference Proceedings*, 341(1):229–239, 07 1995. ISSN 0094-243X. doi: 10.1063/1.48731.

H. Keppler and N. Bolfan-Casanova. Thermodynamics of Water Solubility and Partitioning. *Reviews in Mineralogy and Geochemistry*, 62(1):193–230, 01 2006. ISSN 1529-6466. doi: 10.2138/rmg.2006.62.9.

S. H. Kirby, W. B. Durham, and L. A. Stern. Mantle phase changes and deep-earthquake faulting in subducting lithosphere. *Science*, 252(5003):216–225, 1991. doi: 10.1126/science.252.5003.216.

K. M. Knesel, B. E. Cohen, P. M. Vasconcelos, and D. S. Thiede. Rapid change in drift of the Australian plate records collision with Ontong Java plateau. *Nature*, 454(7205):754–757, 2008.

D. L. Kohlstedt, H. Keppler, and D. C. Rubie. Solubility of water in the α, β and γ phases of $(Mg, Fe)_2SiO_4$, 1996.

T. Komabayashi, S. Omori, and S. Maruyama. Petrogenetic grid in the system $MgO - SiO_2 - H_2O$ up to 30 GPa, 1600°C: Applications to hydrous peridotite subducting into the Earth's deep interior. *Journal of Geophysical Research: Solid Earth*, 109(B3), 2004. doi: https://doi.org/10.1029/2003JB002651.

P. Kumar, X. Yuan, M. R. Kumar, R. Kind, X. Li, and R. Chadha. The rapid drift of the Indian tectonic plate. *Nature*, 449(7164):894–897, 2007.

C. Lee and S. D. King. Dynamic buckling of subducting slabs reconciles geological and geophysical observations. *Earth and Planetary Science Letters*, 312(3):360–370, 2011. ISSN 0012-821X. doi: https://doi.org/10.1016/j.epsl.2011.10.033.

S. Li, D. J. van Hinsbergen, Y. Najman, J. Liu-Zeng, C. Deng, and R. Zhu. Does pulsed tibetan deformation correlate with indian plate motion changes? *Earth and Planetary Science Letters*, 536:116144, 2020a. ISSN 0012-821X. doi: https://doi.org/10.1016/j.epsl.2020.116144.

S. Li, D. J. J. van Hinsbergen, Z. Shen, Y. Najman, C. Deng, and R. Zhu. Anisotropy of Magnetic Susceptibility (AMS) Analysis of the Gonjo Basin as an Independent Constraint to Date Tibetan Shortening Pulses. *Geophysical Research Letters*, 47(8):e2020GL087531, 2020b. doi: https://doi.org/10.1029/2020GL087531.

Y. Li, L. Vočadlo, T. Sun, and J. P. Brodholt. The Earth's core as a reservoir of water. *Nature Geoscience*, 13(6):453–458, 2020c.

Z.-H. Li, T. Gerya, and J. A. Connolly. Variability of subducting slab morphologies in the mantle transition zone: Insight from petrological-thermomechanical modeling. *Earth-Science Reviews*, 196:102874, 2019. ISSN 0012-8252. doi: https://doi.org/10.1016/j.earscirev.2019.05.018.

J. Liao, T. Gerya, M. Thielmann, A. A. G. Webb, S. K. Kufner, and A. Yin. 3D geodynamic models for the development of opposing continental subduction zones: The Hindu Kush–Pamir example. *Earth and Planetary Science Letters*, 480:133–146, 2017. ISSN 0012821X. doi: 10.1016/j.epsl.2017.10.005.

K. Litasov, E. Ohtani, F. Langenhorst, H. Yurimoto, T. Kubo, and T. Kondo. Water solubility in mg-perovskites and water storage capacity in the lower mantle. *Earth and Planetary Science Letters*, 211(1-2):189–203, 2003.

K. Litasov, E. Ohtani, A. Sano, A. Suzuki, and K. Funakoshi. In situ x-ray diffraction study of post-spinel transformation in a peridotite mantle: Implication for the 660-km discontinuity. *Earth and Planetary Science Letters*, 238(3):311–328, 2005. ISSN 0012-821X. doi: https://doi.org/10.1016/j.epsl.2005.08.001.

K. D. Litasov and E. Ohtani. Effect of water on the phase relations in Earth's mantle and deep water cycle. In *Advances in High-Pressure Mineralogy*. Geological Society of America, 01 2007. ISBN 9780813724218. doi: 10.1130/2007.2421(08).

K. D. Litasov, E. Ohtani, A. Sano, A. Suzuki, and K. Funakoshi. Wet subduction versus cold subduction. *Geophysical Research Letters*, 32(13). doi: https://doi.org/10.1029/2005GL022921.

C. Lithgow-Bertelloni and M. A. Richards. The dynamics of cenozoic and mesozoic plate motions. *Reviews of Geophysics*, 36(1):27–78, 1998. doi: https://doi.org/10.1029/97RG02282.

H. Liu, M. Gurnis, W. Leng, Z. Jia, and Z. Zhan. Tonga slab morphology and stress variations controlled by a relic slab: Implications for deep earthquakes in the Tonga-Fiji region. *Geophysical Research Letters*, 48(7):e2020GL091331, 2021. doi: doi.org/10.1029/2020GL091331.

F. T. Mackenzie. *Sediments, Diagenesis, and Sedimentary Rocks: Treatise on Geochemistry, Volume 7*, volume 7. Elsevier, 2005.

S. Maruyama and T. Komiya. The Oldest Pillow Lavas, 3.8-3.7 Ga from the Isua Supracrustal Belt, SW Greenland. *Journal of Geography (Chigaku Zasshi)*, 120 (5):869–876, 2011. doi: 10.5026/jgeography.120.869.

D. G. V. D. Meer, R. E. Zeebe, D. J. J. van Hinsbergen, A. Sluijs, W. Spakman, and T. H. Torsvik. Plate tectonic controls on atmospheric CO_2 levels since the Triassic. *Proceedings of the National Academy of Sciences*, 111(12):4380–4385, 2014. doi: 10.1073/pnas.1315657111.

H. Morishima, T. Kato, M. Suto, E. Ohtani, S. Urakawa, W. Utsumi, O. Shimomura, and T. Kikegawa. The Phase Boundary Between α- and β-$Mg2_SiO_4$ Determined by in Situ X-ray Observation. *Science*, 265(5176):1202–1203, 1994. doi: 10.1126/science.265.5176.1202.

M. J. Mottl, B. T. Glazer, R. I. Kaiser, and K. J. Meech. Water and astrobiology. *Geochemistry*, 67(4):253–282, 2007. ISSN 0009-2819. doi: https://doi.org/10.1016/j.chemer.2007.09.002.

R. D. Müller, M. Seton, S. Zahirovic, S. E. Williams, K. J. Matthews, N. M. Wright, G. E. Shephard, K. T. Maloney, N. Barnett-Moore, M. Hosseinpour, et al. Ocean basin evolution and global-scale plate reorganization events since Pangea breakup. *Annual Review of Earth and Planetary Sciences*, 44:107–138, 2016. doi: 10.1146/annurev-earth-060115-012211.

R. D. Müller, N. Flament, J. Cannon, M. G. Tetley, S. E. Williams, X. Cao, O. F. Bodur, S. Zahirovic, and A. Merdith. A tectonic-rules-based mantle reference frame since 1 billion years ago – implications for supercontinent cycles and plate–mantle system evolution. *Solid Earth*, 13(7):1127–1159, 2022. doi: 10.5194/se-13-1127-2022.

M. Murakami, K. Hirose, H. Yurimoto, S. Nakashima, and N. Takafuji. Water in earth's lower mantle. *Science*, 295(5561):1885–1887, 2002. ISSN 0036-8075. doi: 10.1126/science.1065998.

R. D. Müller, S. Zahirovic, S. E. Williams, J. Cannon, M. Seton, D. J. Bower, M. G. Tetley, C. Heine, E. Le Breton, S. Liu, S. H. J. Russell, T. Yang, J. Leonard, and M. Gurnis. A global plate model including lithospheric deformation along major rifts and orogens since the triassic. *Tectonics*, 38(6): 1884–1907, 2019. doi: https://doi.org/10.1029/2018TC005462.

T. Nakagawa. Numerical modeling on global-scale mantle water cycle and its impact on the sea-level change. *Earth and Planetary Science Letters*, 619:118312, 2023. ISSN 0012-821X. doi: https://doi.org/10.1016/j.epsl.2023.118312.

T. Nakagawa and H. Iwamori. On the implications of the coupled evolution of the deep planetary interior and the presence of surface ocean water in hydrous mantle convection. *Comptes Rendus Geoscience*, 351(2):197–208, 2019. ISSN 1631-0713. doi: https://doi.org/10.1016/j.crte.2019.02.001.

A. Nakao, H. Iwamori, and T. Nakakuki. Effects of water transportation on subduction dynamics: Roles of viscosity and density reduction. *Earth and Planetary Science Letters*, 454:178–191, 2016. ISSN 0012821X. doi: 10.1016/j.epsl.2016.08.016.

A. Nakao, H. Iwamori, T. Nakakuki, Y. J. Suzuki, and H. Nakamura. Roles of Hydrous Lithospheric Mantle in Deep Water Transportation and Subduction Dynamics. *Geophysical Research Letters*, 45(11):5336–5343, 2018. ISSN 19448007. doi: 10.1029/2017GL076953.

M. Obayashi, J. Yoshimitsu, G. Nolet, Y. Fukao, H. Shiobara, H. Sugioka, H. Miyamachi, and Y. Gao. Finite frequency whole mantle P wave tomography: Improvement of subducted slab images. *Geophysical Research Letters*, 40(21):5652–5657, 2013. doi: doi.org/10.1002/2013GL057401.

E. Ohtani, M. Toma, K. Litasov, T. Kubo, and A. Suzuki. Stability of dense hydrous magnesium silicate phases and water storage capacity in the transition zone and lower mantle. *Physics of the Earth and Planetary Interiors*, 124(1):105–117, 2001. ISSN 0031-9201. doi: https://doi.org/10.1016/S0031-9201(01)00192-3.

E. Ohtani, K. Litasov, T. Hosoya, T. Kubo, and T. Kondo. Water transport into the deep mantle and formation of a hydrous transition zone. *Physics of the Earth and Planetary Interiors*, 143(1-2):255–269, 2004. ISSN 00319201. doi: 10.1016/j.pepi.2003.09.015.

T. Ohuchi, X. Lei, H. Ohfuji, Y. Higo, Y. Tange, T. Sakai, K. Fujino, and T. Irifune. Intermediate-depth earthquakes linked to localized heating in dunite and harzburgite. *Nature Geoscience*, 10(10):771–776, 2017. doi: doi.org/10.1038/ngeo3011.

E. A. Okal and S. H. Kirby. Deep earthquakes beneath the Fiji basin, SW Pacific: Earth's most intense deep seismicity in stagnant slabs. *Physics of the Earth and Planetary Interiors*, 109(1):25–63, 1998. doi: doi.org/10.1016/S0031-9201(98)00116-2.

S. Ono. Stability limits of hydrous minerals in sediment and mid-ocean ridge basalt compositions: Implications for water transport in subduction zones, 1998. ISSN 0148-0227.

L. Page and K. Hattori. Abyssal Serpentinites: Transporting Halogens from Earth's Surface to the Deep Mantle. *Minerals*, 9:61, 01 2019. doi: 10.3390/min9010061.

A. J. Parsons, K. Sigloch, and K. Hosseini. Australian Plate Subduction is Responsible for Northward Motion of the India-Asia Collision Zone and $\sim 1,000$ km Lateral Migration of the Indian Slab. *Geophysical Research Letters*, 48(18):e2021GL094904, 2021. doi: https://doi.org/10.1029/2021GL094904.

V. Patočka, H. Čížková, and J. Pokorný. Dynamic component of the asthenosphere: Lateral viscosity variations due to dislocation creep at the base of oceanic plates. *Geophysical Research Letters*, 51(13):e2024GL109116, 2024.

P. Patriat and J. Achache. India - Eurasia collision chronology has implications for crustal shortening and driving mechanism of plates. *Nature*, 311(5987): 615–621, 1984.

A. Pawley. Chlorite stability in mantle peridotite: the reaction clinochlore+ enstatite= forsterite+ pyrope+ H_2O. *Contributions to Mineralogy and Petrology*, 144(4):449–456, 2003.

A. R. Pawley and J. R. Holloway. Water sources for subduction zone volcanism: New experimental constraints. *Science*, 260(5108):664–667, 1993. doi: 10.1126/science.260.5108.664.

S. A. Peacock. Fluid processes in subduction zones. *Science*, 248(4953):329–337, 1990.

S. M. Peacock and K. Wang. Seismic consequences of warm versus cool subduction metamorphism: Examples from southwest and northeast japan. *Science*, 286 (5441):937–939, 1999. ISSN 0036-8075. doi: 10.1126/science.286.5441.937.

D. Pearson, F. Brenker, F. Nestola, J. McNeill, L. Nasdala, M. Hutchison, S. Matveev, K. Mather, G. Silversmit, S. Schmitz, et al. Hydrous mantle transition zone indicated by ringwoodite included within diamond. *Nature*, 507(7491):221–224, 2014.

A. H. Peslier, M. Schönbächler, H. Busemann, and S.-I. Karato. Water in the Earth's interior: distribution and origin. *Space Science Reviews*, 212:743–810, 2017.

T. Plank and C. H. Langmuir. The chemical composition of subducting sediment and its consequences for the crust and mantle. *Chemical Geology*, 145(3):325 – 394, 1998. ISSN 0009-2541. doi: https://doi.org/10.1016/S0009-2541(97)00150-2.

J. Pokorný, H. Čížková, and A. van den Berg. Feedbacks between subduction dynamics and slab deformation: Combined effects of nonlinear rheology of a weak decoupling layer and phase transitions. *Physics of the Earth and Planetary Interiors*, 313:106679, 2021.

J. Pokorný, H. Čížková, C. R. Bina, and A. van den Berg. 2D stress rotation in the Tonga subduction region. *Earth and Planetary Science Letters*, 621:118379, 2023. ISSN 0012-821X. doi: https://doi.org/10.1016/j.epsl.2023.118379.

M. Pons, S. V. Sobolev, S. Liu, and D. Neuharth. Hindered Trench Migration Due To Slab Steepening Controls the Formation of the Central Andes. *Journal of Geophysical Research: Solid Earth*, 127(12):e2022JB025229, 2022. doi: https://doi.org/10.1029/2022JB025229.

A. E. Pusok and D. R. Stegman. The convergence history of India-Eurasia records multiple subduction dynamics processes. *Science Advances*, 6(19):eaaz8681, 2020. doi: 10.1126/sciadv.aaz8681.

A. Qayyum, N. Lom, E. L. Advokaat, W. Spakman, D. G. van der Meer, and D. J. J. van Hinsbergen. Subduction and Slab Detachment Under Moving Trenches During Ongoing India-Asia Convergence. *Geochemistry, Geophysics, Geosystems*, 23(11):e2022GC010336, 2022. doi: https://doi.org/10.1029/2022GC010336.

G. Ranalli. *Rheology of the earth*. Springer Science & Business Media, 1995. ISBN 0412546701.

C. R. Ranero, J. Phipps Morgan, K. McIntosh, and C. Reichert. Bending-related faulting and mantle serpentinization at the middle america trench. *Nature*, 425 (6956):367–373, 2003.

A. Replumaz, H. Karason, R. D. van der Hilst, J. Besse, and P. Tapponnier. 4-D evolution of SE Asia's mantle from geological reconstructions and seismic tomography. *Earth and Planetary Science Letters*, 221(1):103–115, 2004. ISSN 0012-821X. doi: https://doi.org/10.1016/S0012-821X(04)00070-6.

N. Ribe, E. Stutzmann, Y. Ren, and R. van der Hilst. Buckling instabilities of subducted lithosphere beneath the transition zone. *Earth and Planetary Science Letters*, 254(1):173–179, 2007. ISSN 0012-821X. doi: https://doi.org/10.1016/j.epsl.2006.11.028.

N. M. Ribe. Bending mechanics and mode selection in free subduction: a thin-sheet analysis. *Geophysical Journal International*, 180(2):559–576, 2010. ISSN 0956-540X. doi: 10.1111/j.1365-246X.2009.04460.x.

G. C. Richard and H. Iwamori. Stagnant slab, wet plumes and cenozoic volcanism in east asia. *Physics of the Earth and Planetary Interiors*, 183(1):280–287, 2010. ISSN 0031-9201. doi: https://doi.org/10.1016/j.pepi.2010.02.009. Special Issue on Deep Slab and Mantle Dynamics.

S. Richards, R. Holm, and G. Barber. When slabs collide: A tectonic assessment of deep earthquakes in the Tonga-Vanuatu region. *Geology*, 39(8):787–790, 2011. doi: doi.org/10.1130/G31937.1.

L. H. Royden and L. Husson. Trench motion, slab geometry and viscous stresses in subduction systems. *Geophysical Journal International*, 167(2):881–905, 2006. doi: doi.org/10.1111/j.1365-246X.2006.03079.x.

M. L. Rudolph, V. Lekić, and C. Lithgow-Bertelloni. Viscosity jump in Earth's mid-mantle. *Science*, 350(6266):1349–1352, 2015. doi: doi:10.1126/science.aad1929.

L. H. Rüpke, J. P. Morgan, M. Hort, and J. A. Connolly. Serpentine and the subduction zone water cycle. *Earth and Planetary Science Letters*, 223(1-2): 17–34, 2004. ISSN 0012821X. doi: 10.1016/j.epsl.2004.04.018.

D. M. Saffer and H. J. Tobin. Hydrogeology and mechanics of subduction zone forearcs: Fluid flow and pore pressure. *Annual Review of Earth and Planetary Sciences*, 39:157–186, 2011.

D. Sandiford and L. Moresi. Improving subduction interface implementation in dynamic numerical models. *Solid Earth*, 10(3):969–985, 2019. doi: 10.5194/se-10-969-2019.

D. Sandiford, L. Moresi, M. Sandiford, R. Farrington, and T. Yang. The fingerprints of flexure in slab seismicity. *Tectonics*, 39(8), 2020. doi: doi.org/10.1029/2019TC005894.

W. Schellart. Influence of the subducting plate velocity on the geometry of the slab and migration of the subduction hinge. *Earth and Planetary Science Letters*, 231(3):197–219, 2005. ISSN 0012-821X. doi: https://doi.org/10.1016/j.epsl.2004.12.019.

W. Schellart, G. Lister, and V. Toy. A late Cretaceous and Cenozoic reconstruction of the southwest Pacific region: Tectonics controlled by subduction and slab rollback processes. *Earth-Science Reviews*, 76(3-4):191–233, 2006. doi: doi.org/10.1016/j.earscirev.2006.01.002.

W. Schellart, D. Stegman, and J. Freeman. Global trench migration velocities and slab migration induced upper mantle volume fluxes: Constraints to find an Earth reference frame based on minimizing viscous dissipation. *Earth-Science Reviews*, 88(1):118–144, 2008. doi: doi.org/10.1016/j.earscirev.2008.01.005.

W. P. Schellart and W. Spakman. Mantle constraints on the plate tectonic evolution of the Tonga–Kermadec–Hikurangi subduction zone and the south Fiji basin region. *Australian Journal of Earth Sciences*, 59(6):933–952, 2012. doi: doi.org/10.1080/08120099.2012.679692.

W. P. Schellart, J. Freeman, D. R. Stegman, L. Moresi, and D. May. Evolution and diversity of subduction zones controlled by slab width. *Nature*, 446(7133):308–311, 2007.

H. Schmeling, R. Monz, and D. C. Rubie. The influence of olivine metastability on the dynamics of subduction. *Earth and Planetary Science Letters*, 165(1):55 – 66, 1999. ISSN 0012-821X. doi: https://doi.org/10.1016/S0012-821X(98)00249-0.

M. W. Schmidt and S. Poli. Experimentally based water budgets for dehydrating slabs and consequences for arc magma generation. *Earth and Planetary Science Letters*, 163(1-4):361–379, 1998. ISSN 0012821X. doi: 10.1016/S0012-821X(98)00142-3.

G. Schubert, D. Turcotte, and P. Olson. Mantle convection in the earth and planets,(2001). *Cambridge Univ. press, Cambridge*, 2001.

M. Sdrolias and R. D. Müller. Controls on back-arc basin formation. *Geochemistry, Geophysics, Geosystems*, 7(4), 2006. doi: https://doi.org/10.1029/2005GC001090.

A. Segal and N. Praagman. The Sepran Fem Package, Technical Report, Ingenieursbureau Sepra, 2005.

E. Seibold and W. Berger. *The Sea Floor. An Introduction to Marine Geology.* Springer Verlag, N.Y, 1984. doi: 10.1111/j.1439-0485.1984.tb00309.x.

W. Sharples, M. A. Jadamec, L. N. Moresi, and F. A. Capitanio. Overriding plate controls on subduction evolution. *Journal of Geophysical Research: Solid Earth*, 119(8):6684–6704, 2014. doi: https://doi.org/10.1002/2014JB011163.

G. Shelton and J. Tullis. Experimental flow laws for crustal rocks. *EOS, Trans. Am. Geophysical union*, 62, 1981.

S. R. Shieh, H.-k. Mao, R. J. Hemley, and L. C. Ming. Decomposition of phase d in the lower mantle and the fate of dense hydrous silicates in subducting slabs. *Earth and Planetary Science Letters*, 159(1-2):13–23, 1998.

R. H. Sibson. Fault rocks and fault mechanisms. *Journal of the Geological Society*, 133(3):191–213, 1977. doi: 10.1144/gsjgs.133.3.0191.

K. Sigloch and M. G. Mihalynuk. Intra-oceanic subduction shaped the assembly of cordilleran north america. *Nature*, 496(7443):50–56, 2013.

C. Sippl, A. Dielforder, T. John, and S. M. Schmalholz. Global constraints on intermediate-depth intraslab stresses from slab geometries and mechanisms of double seismic zone earthquakes. *Geochemistry, Geophysics, Geosystems*, 23 (9), 2022. doi: doi.org/10.1029/2022GC010498.

W. Spakman, M. V. Chertova, A. van den Berg, and D. J. van Hinsbergen. Puzzling features of western Mediterranean tectonics explained by slab dragging. *Nature Geoscience*, 11(3):211–216, 2018.

C. Spandler and C. Pirard. Element recycling from subducting slabs to arc crust: A review. *Lithos*, 170:208–223, 2013.

H. Staudigel, S. R. Hart, H.-U. Schmincke, and B. M. Smith. Cretaceous ocean crust at DSDP Sites 417 and 418: Carbon uptake from weathering versus loss by magmatic outgassing. *Geochimica et Cosmochimica Acta*, 53(11):3091–3094, 1989.

D. Stegman, R. Farrington, F. Capitanio, and W. Schellart. A regime diagram for subduction styles from 3-d numerical models of free subduction. *Tectonophysics*, 483(1):29 – 45, 2010. ISSN 0040-1951. doi: https://doi.org/10.1016/j.tecto.2009.08.041.

V. Steinbach and D. A. Yuen. The effects of temperature-dependent viscosity on mantle convection with the two major phase transitions. *Physics of the Earth and Planetary Interiors*, 90(1):13 – 36, 1995. ISSN 0031-9201. doi: https://doi.org/10.1016/0031-9201(95)03018-R.

C. Su, Y. Liu, D. Fan, W. Song, J. Jiang, Z. Sun, and G. Yang. Thermodynamic Properties of Fe-Bearing Wadsleyite and Determination of the Olivine-Wadsleyite Phase Transition Boundary in $(Mg, Fe)_2SiO_4$ System. *Frontiers in Earth Science*, 10:879678, 2022.

R. Sutherland, G. R. Dickens, P. Blum, C. Agnini, L. Alegret, G. Asatryan, J. Bhattacharya, A. Bordenave, L. Chang, J. Collot, et al. Continental-scale geographic change across Zealandia during Paleogene subduction initiation. *Geology*, 48(5):419–424, 2020. doi: doi.org/10.1130/G47008.1.

M. Thielmann. Grain size assisted thermal runaway as a nucleation mechanism for continental mantle earthquakes: Impact of complex rheologies. *Tectonophysics*, 746:611–623, 2018. doi: doi.org/10.1016/j.tecto.2017.08.038.

Y. Torii and S. Yoshioka. Physical conditions producing slab stagnation: Constraints of the Clapeyron slope, mantle viscosity, trench retreat, and dip angles. *Tectonophysics*, 445(3-4):200–209, 2007. ISSN 00401951. doi: 10.1016/j.tecto.2007.08.003.

T. H. Torsvik, R. D. Müller, R. Van der Voo, B. Steinberger, and C. Gaina. Global plate motion frames: Toward a unified model. *Reviews of Geophysics*, 46(3), 2008. doi: https://doi.org/10.1029/2007RG000227.

B. Vaes, D. J. J. van Hinsbergen, and L. M. Boschman. Reconstruction of subduction and back-arc spreading in the NW Pacific and Aleutian basin: Clues to causes of Cretaceous and Eocene plate reorganizations. *Tectonics*, 38(4): 1367–1413, 2019. doi: https://doi.org/10.1029/2018TC005164.

S. H. van de Lagemaat, D. J. Van Hinsbergen, L. M. Boschman, P. J. Kamp, and W. Spakman. Southwest Pacific absolute plate kinematic reconstruction reveals major cenozoic Tonga-Kermadec slab dragging. *Tectonics*, 37(8):2647–2674, 2018. doi: doi.org/10.1029/2017TC004901.

S. H. van de Lagemaat, P. J. Kamp, L. M. Boschman, and D. J. van Hinsbergen. Reconciling the Cretaceous breakup and demise of the Phoenix Plate with East Gondwana orogenesis in New Zealand. *Earth-Science Reviews*, 236:104276, 2023. ISSN 0012-8252. doi: https://doi.org/10.1016/j.earscirev.2022.104276.

A. van den Berg, G. Segal, and D. Yuen. Sepran: A versatile finite-element package for a wide variety of problems in geosciences. *Journal of Earth Science*, 26(1):89–95, 1 2015. ISSN 1674-487X. doi: 10.1007/s12583-015-0508-0.

A. van den Berg, D. Yuen, K. Umemoto, M. Jacobs, and R. Wentzcovitch. Mass-dependent dynamics of terrestrial exoplanets using ab initio mineral properties. *Icarus*, 317:412–426, 2019. ISSN 0019-1035. doi: https://doi.org/10.1016/j.icarus.2018.08.016.

A. P. van den Berg, P. E. van Keken, and D. A. Yuen. The effects of a composite non-newtonian and newtonian rheology on mantle convection. *Geophysical Journal International*, 115(1):62–78, 1993.

S. van der Lee, K. Regenauer-Lieb, and D. A. Yuen. The role of water in connecting past and future episodes of subduction. *Earth and Planetary Science Letters*, 273(1):15–27, 2008. ISSN 0012-821X. doi: https://doi.org/10.1016/j.epsl.2008.04.041.

D. van der Meer, W. Spakman, D. van Hinsbergen, M. Amaru, and T. Torsvik. Towards absolute plate motions constrained by lower-mantle slab remnants. *Nature Geoscience*, 3:36–40, 2010. doi: 10.1038/NGEO708.

D. G. van der Meer, D. J. van Hinsbergen, and W. Spakman. Atlas of the underworld: Slab remnants in the mantle, their sinking history, and a new outlook on lower mantle viscosity. *Tectonophysics*, 723:309 – 448, 2018. ISSN 0040-1951. doi: https://doi.org/10.1016/j.tecto.2017.10.004.

R. Van der Voo, W. Spakman, and H. Bijwaard. Tethyan subducted slabs under India. *Earth and Planetary Science Letters*, 171(1):7–20, 1999. ISSN 0012-821X. doi: https://doi.org/10.1016/S0012-821X(99)00131-4.

E. van der Wiel, J. Pokorný, H. Čížková, W. Spakman, A. P. van den Berg, and D. J. van Hinsbergen. Slab buckling as a driver for rapid oscillations in Indian plate motion and subduction rate. *Communications Earth & Environment*, 5 (1):316, 2024.

D. J. van Hinsbergen, P. C. Lippert, S. Li, W. Huang, E. L. Advokaat, and W. Spakman. Reconstructing greater india: Paleogeographic, kinematic, and geodynamic perspectives. *Tectonophysics*, 760:69–94, 2019. ISSN 0040-1951. doi: https://doi.org/10.1016/j.tecto.2018.04.006.

D. J. van Hinsbergen, B. Steinberger, C. Guilmette, M. Maffione, D. Gürer, K. Peters, A. Plunder, P. J. McPhee, C. Gaina, E. L. Advokaat, et al. A record of plume-induced plate rotation triggering subduction initiation. *Nature Geoscience*, 14(8):626–630, 2021.

D. J. J. van Hinsbergen, B. Steinberger, P. V. Doubrovine, and R. Gassmöller. Acceleration and deceleration of india-asia convergence since the cretaceous: Roles of mantle plumes and continental collision. *Journal of Geophysical Research: Solid Earth*, 116(B6), 2011. doi: https://doi.org/10.1029/2010JB008051.

J. van Hunen. *Shallow and buoyant lithospheric subduction: causes and implications from thermo-chemical numerical modeling.* dissertation thesis, Utrecht University, 2001.

J. van Hunen, A. P. van den Berg, and N. J. Vlaar. A thermo-mechanical model of horizontal subduction below an overriding plate. *Earth and Planetary Science Letters*, 182(2):157–169, 2000. doi: doi.org/10.1016/S0012-821X(00)00240-5.

J. van Hunen, A. P. van den Berg, and N. J. Vlaar. Latent heat effects of the major mantle phase transitions on low-angle subduction. *Earth and Planetary Science Letters*, 190(3):125 – 135, 2001. ISSN 0012-821X. doi: https://doi.org/10.1016/S0012-821X(01)00383-1.

P. E. Van Keken, B. Kiefer, and S. M. Peacock. High-resolution models of subduction zones: Implications for mineral dehydration reactions and the transport of water into the deep mantle. *Geochemistry, Geophysics, Geosystems*, 3(10): 1–of, 2002.

P. E. van Keken, B. R. Hacker, E. M. Syracuse, and G. A. Abers. Subduction factory: 4. Depth-dependent flux of H_2O from subducting slabs worldwide. *Journal of Geophysical Research: Solid Earth*, 116(B1), 2011. doi: https://doi.org/10.1029/2010JB007922.

M. Vassiliou, B. Hager, and A. Raefsky. The distribution of earthquakes with depth and stress in subducting slabs. *Journal of geodynamics*, 1(1):11–28, 1984. doi: doi.org/10.1016/0264-3707(84)90004-8.

L. White and G. Lister. The collision of India with Asia. *Journal of Geodynamics*, 56-57:7–17, 2012. ISSN 0264-3707. doi: https://doi.org/10.1016/j.jog.2011.06.006.

W. White and E. Klein. 4.13 - composition of the oceanic crust. In H. D. Holland and K. K. Turekian, editors, *Treatise on Geochemistry (Second Edition)*, pages 457 – 496. Elsevier, Oxford, second edition edition, 2014. ISBN 978-0-08-098300-4. doi: https://doi.org/10.1016/B978-0-08-095975-7.00315-6.

C. J. Wilson, D. H. Moore, S. A. Vollgger, and H. E. Madeley. Structural evolution of the orogenic gold deposits in central Victoria, Australia: The role of regional stress change and the tectonic regime. *Ore Geology Reviews*, 120:103390, 2020. ISSN 0169-1368. doi: https://doi.org/10.1016/j.oregeorev.2020.103390.

R. Wortel and S. Cloetingh. On the origin of the Cocos-Nazca spreading center. *Geology*, 9(9):425–430, 09 1981. ISSN 0091-7613. doi: 10.1130/0091-7613(1981)9<425:OTOOTC>2.0.CO;2.

J. Wu, J. Suppe, R. Lu, and R. Kanda. Philippine sea and east asian plate tectonics since 52 Ma constrained by new subducted slab reconstruction methods. *Journal of Geophysical Research: Solid Earth*, 121(6):4670–4741, 2016. doi: https://doi.org/10.1002/2016JB012923.

J. Wu, S. J. Desch, L. Schaefer, L. T. Elkins-Tanton, K. Pahlevan, and P. R. Buseck. Origin of earth's water: Chondritic inheritance plus nebular ingassing and storage of hydrogen in the core. *Journal of Geophysical Research: Planets*, 123(10):2691–2712, 2018. doi: https://doi.org/10.1029/2018JE005698.

K. Xue, W. P. Schellart, and V. Strak. Overriding plate deformation and topography during slab rollback and slab rollover: Insights from subduction experiments. *Tectonics*, 41(2):e2021TC007089, 2022. doi: https://doi.org/10.1029/2021TC007089.

T. Yang, M. Gurnis, and S. Zahirovic. Slab avalanche-induced tectonics in self-consistent dynamic models. *Tectonophysics*, 746:251–265, 2018. doi: 10.1016/j.tecto.2016.12.007.

S. Zahirovic, R. D. Müller, M. Seton, and N. Flament. Tectonic speed limits from plate kinematic reconstructions. *Earth and Planetary Science Letters*, 418:40–52, 2015. ISSN 0012-821X. doi: https://doi.org/10.1016/j.epsl.2015.02.037.

J. Zahradník, H. Čížková, C. R. Bina, E. Sokos, J. Jánský, H. Tavera, and J. Carvalho. A recent deep earthquake doublet in light of long-term evolution of Nazca subduction. *Scientific Reports*, 7(1):45153, 2017. doi: doi.org/10.1038/srep45153.

Z. Zhan. Mechanisms and implications of deep earthquakes. *Annual Review of Earth and Planetary Sciences*, 48:147–174, 2020. doi: 10.1146/annurev-earth-053018-060314.

H. Zhang, H. Che, J. Xia, Q. Cheng, D. Qi, J. Cao, and Y. Luo. Sedimentary $CaCO_3$ accumulation in the deep west Pacific Ocean. *Frontiers in Earth Science*, 10:857260, 2022.

D. Zhao, M. Fujisawa, and G. Toyokuni. Tomography of the subducting Pacific slab and the 2015 Bonin deepest earthquake (Mw 7.9). *Scientific Reports*, 7 (February):1–8, 2017. ISSN 20452322. doi: 10.1038/srep44487.

List of publications

1. [Pokorný et al., 2021]: J.Pokorný, H. Čížková, and A. van den Berg. Feedbacks between subduction dynamics and slab deformation: Combined effects of nonlinear rheology of a weak decoupling layer and phase transitions. Physics of the Earth and Planetary Interiors, doi.org/10.1016/j.pepi.2021.106679, 2021

2. [Pokorný et al., 2023]: J.Pokorný, H. Čížková, C. R. Bina and A. van den Berg. 2D stress rotation in the Tonga subduction region. Earth and Planetary Science Letters, 5doi.org/10.1016/j.epsl.2023.118379, 2023

3. [van der Wiel et al., 2024]: E. van der Wiel, J. Pokorný, H. Čížková, W. Spakman, A. P. van den Berg, and D. J. van Hinsbergen. Slab buckling as a driver for rapid oscillations in Indian plate motion and subduction rate. Communications Earth & Environment, 5(1):316, 2024.

4. [Patočka et al., 2024]: V. Patočka, H. Čížková, and J. Pokorný. Dynamic component of the asthenosphere: Lateral viscosity variations due to dislocation creep at the base of oceanic plates. Geophysical Research Letters, 51(13):e2024GL109116, 2024.